

Proton imaging of high-energy-density laboratory plasmas

Derek B. Schaeffer 

*Department of Physics and Astronomy, University of California—Los Angeles,
Los Angeles, California 90095, USA*

Archie F. A. Bott 

*Department of Physics, University of Oxford,
Parks Road, Oxford OX1 3PU, United Kingdom*

Marco Borghesi

*School of Mathematics and Physics, The Queen's University Belfast,
Belfast BT7 1NN, United Kingdom*

Kirk A. Flippo 

*Applied and Fundamental Physics (P-2), Los Alamos National Laboratory,
Los Alamos, New Mexico 87544, USA*

William Fox 

*Princeton Plasma Physics Laboratory, Princeton, New Jersey 08543, USA
and Department of Astrophysical Sciences, Princeton University,
Princeton, New Jersey 08540, USA*

Julien Fuchs 

*LULI-CNRS, CEA, UPMC Université Paris 06, Sorbonne Université,
École Polytechnique, Institut Polytechnique de Paris,
Palaiseau, France*

Chikang Li  and Fredrick H. Séguin

*Plasma Science and Fusion Center, Massachusetts Institute of Technology,
Cambridge, Massachusetts 02139, USA*

Hye-Sook Park 

Lawrence Livermore National Laboratory, Livermore, California 94550, USA

Petros Tzeferacos

*Department of Physics and Astronomy, University of Rochester,
Rochester, New York 14627, USA*

Louise Willingale 

*Gérard Mourou Center for Ultrafast Optical Science,
Department of Electrical Engineering and Computer Science, University of Michigan,
Ann Arbor, Michigan 48109, USA*

 (published 28 December 2023)

Proton imaging has become a key diagnostic for measuring electromagnetic fields in high-energy-density (HED) laboratory plasmas. Compared to other techniques for diagnosing fields, proton imaging is a measurement that can simultaneously offer high spatial and temporal resolution and the ability to distinguish between electric and magnetic fields without the protons perturbing the plasma of interest. Consequently, proton imaging has been used in a wide range of HED experiments, from

*derek.schaeffer@ucla.edu

inertial-confinement fusion to laboratory astrophysics. An overview is provided on the state of the art of proton imaging, including a discussion of experimental considerations like proton sources and detectors, the theory of proton-imaging analysis, and a survey of experimental results demonstrating the breadth of applications. Topics at the frontiers of proton-imaging development are also described, along with an outlook on the future of the field.

DOI: [10.1103/RevModPhys.95.045007](https://doi.org/10.1103/RevModPhys.95.045007)

CONTENTS

| | |
|---|----|
| I. Introduction | 2 |
| A. Context and principles | 2 |
| B. Historical development | 4 |
| II. Experimental Techniques | 5 |
| A. Proton sources | 5 |
| 1. Target normal sheath acceleration | 5 |
| 2. D ³ He | 7 |
| B. Detectors | 8 |
| 1. Film | 8 |
| 2. CR-39 | 9 |
| 3. Other detectors | 10 |
| C. Diagnostic geometry and other considerations | 10 |
| 1. Magnification | 11 |
| 2. Meshes and grids | 11 |
| 3. Spatial resolution | 12 |
| 4. Temporal resolution and multiframe capability | 12 |
| III. Theory of Proton-Imaging Analysis | 15 |
| A. Basics | 15 |
| B. Particle-tracing simulations | 16 |
| 1. Overview | 16 |
| 2. Particle-tracing algorithms | 16 |
| 3. Combined modeling with HEDP codes | 17 |
| 4. Parametrized field models | 17 |
| C. Analytical modeling | 17 |
| 1. Overview | 17 |
| 2. Analytical theory of proton imaging | 18 |
| 3. Analytical interpretations of proton-fluence inhomogeneities | 19 |
| 4. Inverse analysis using electromagnetic-field-reconstruction algorithms | 20 |
| D. Comparing particle-tracing and analytical modeling techniques | 22 |
| IV. Proton-Imaging Experiments | 22 |
| A. Magnetic-Field Generation | 22 |
| B. Magnetic reconnection | 24 |
| C. Weibel instabilities | 25 |
| D. Shocks | 26 |
| E. Jets | 27 |
| F. Turbulence and dynamos | 29 |
| G. Ultrafast dynamics | 30 |
| H. HED hydrodynamic instabilities | 31 |
| I. Inertial-Confinement Fusion | 31 |
| V. Frontiers | 34 |
| A. Advanced sources | 34 |
| B. Advanced detectors | 35 |
| C. Advanced algorithms and analysis | 37 |
| D. Advanced schemes | 38 |
| VI. Summary and Outlook | 38 |
| Acknowledgments | 39 |
| References | 39 |

I. INTRODUCTION

A. Context and principles

Plasmas with energy densities exceeding 10^{11} J m^{-3} (or, equivalently, pressures above 1 Mbar) are found in a wide range of contemporary laboratory experiments (Colvin and Larson, 2014). These “high-energy-density” (HED) plasmas are often created using high-powered laser beams or energetic pulsed power devices. Given the high pressures involved, the conditions typically exist over relatively short timescales ($\lesssim 100 \text{ ns}$) and small volumes ($\lesssim 1 \text{ cm}^3$) (Drake, 2018). Historically, HED plasmas have been studied primarily in the pursuit of inertial-confinement fusion (ICF), in which lasers are used to compress a small pellet of fusion material to extreme pressures, with the goal of initiating a self-sustaining burning plasma to harness as an energy source (Lindl, 1995; Craxton *et al.*, 2015). More generally there have been a large number of experiments studying HED plasmas generated by the interaction of lasers with solid or gaseous targets, with applications to hydrodynamic instabilities, particle acceleration, and ultrafast field and particle dynamics. Because plasmas are also a key component of many astrophysical systems, more recently the field of laboratory astrophysics has utilized HED plasmas in scaled experiments to study a variety of astrophysical phenomena (Gregori, Reville, and Miniati, 2015; Lebedev, Frank, and Ryutov, 2019; Takabe and Kuramitsu, 2021; Blackman and Lebedev, 2022).

An important component in many HED laboratory plasmas is the dynamics of the electromagnetic fields. In ICF, the application of strong magnetic fields is sometimes used to help confine and heat the plasma (Slutz *et al.*, 2010; Chang *et al.*, 2011; Moody *et al.*, 2022). How these fields are compressed, diffuse, and seed instabilities are critical questions for controlling the fusion process. Electromagnetic fields are also fundamental to many kinetic processes studied with HED experiments, including collisionless shocks, filamentary instabilities, jets, magnetic reconnection, and turbulence. Measuring electromagnetic fields is thus vital for helping answer many key open questions in HED plasma physics. However, owing to the high plasma densities and temperatures, short timescales, and/or small volumes, measuring such fields with existing x-ray, optical, and electronic diagnostics is extremely challenging.

Proton imaging is a diagnostic technique in which the deflection of a laser-driven proton probe by Lorentz forces in a plasma can be used to infer an image of the path-integrated strength of the electromagnetic fields. For typical proton energies of several MeV, proton imaging is well suited to

studying HED plasmas with strong fields for the following reasons: (1) the protons are “stiff” enough that they experience only small deflections for typical field strengths, allowing the detected proton position to be related simply to the initial proton position in order to infer field strengths; (2) for many experiments, the protons traverse the experimental plasma on timescales that are short compared to dynamical timescales, providing a relatively static snapshot of the fields; (3) the proton images have high spatial resolution owing to (i) the small source size of laser-driven proton beams as well as (ii) their high laminarity; (4) the proton beam, being locally of much lower density than the probed plasma, does not perturb it; and (5) the dependence of the proton deflections on proton energy or geometry is different for electric and magnetic fields, enabling the contribution from each to be distinguished using different proton energies or probing from different directions. We note that proton imaging is also referred to as proton radiography or proton deflectometry in the literature, where the former can be used to describe the imaging of proton scattering and stopping from either density or electromagnetic fields and the latter is often used when one directly measures proton deflections with, for example, a mesh or grid. In this review, we focus primarily on proton deflections from electromagnetic fields rather than from collisions; however, because collisional scattering can have a non-negligible effect on proton images of HED experiments involving cold and/or dense plasmas, we consider its effect at various points in our review.

We illustrate the basic concept that underlies proton imaging with a schematic of a proton-imaging setup (shown in Fig. 1). Protons from a point source pass through the plasma of interest, are deflected by electromagnetic fields, and then travel ballistically to a detector, where they form an image of the field structures in the plasma. Inhomogeneous electromagnetic fields in the plasma plane differentially deflect protons with distinct incident trajectories, which in turn gives rise to inhomogeneous proton fluence on the detector. This allows the path-integrated strengths of the electromagnetic fields to be estimated by relating the proton-fluence variations on the detector to the displacement experienced by those protons as they pass through the fields in the plasma.

The diagnostic is typically configured in the paraxial limit, in which the characteristic scale ℓ_{EM} of electromagnetic fields in the plasma being probed is much smaller than the distance r_s between the source and the plasma ($\ell_{EM} \ll r_s$), and in a point-projection geometry, in which the distance r_d from the

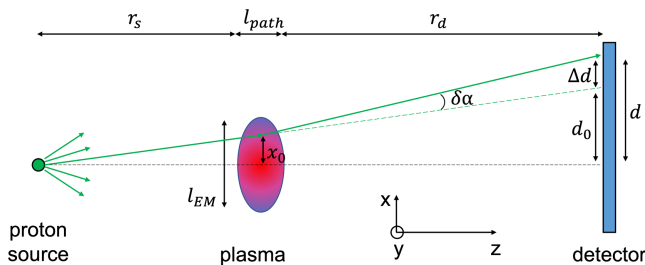


FIG. 1. Schematic of a proton-imaging setup.

plasma to the detector greatly exceeds the path length l_{path} of the protons through the plasma ($r_d \gg l_{\text{path}}$). Consequently, for sufficiently large proton energies (with characteristic deflection velocities that are much smaller than the incident velocities) the path-integrated electromagnetic-field strengths can be related to the deflection angle $\delta\alpha$ of a proton. Under these approximations and limiting to deflections along \hat{x} without loss of generality, $\delta\alpha$ is given by (see Fig. 1)

$$\delta\alpha = \frac{e}{m_p v_p^2} \int_0^{l_{\text{path}}} ds \left[E_x + \frac{(\mathbf{v}_p \times \mathbf{B})_x}{c} \right], \quad (1)$$

where e is the elementary charge, m_p is the mass of a proton, c is the speed of light, \mathbf{v}_p (v_p) is the protons' velocity (speed), and \mathbf{E} and \mathbf{B} are the electric and magnetic fields in the plasma, respectively. Here and in the rest of the review we express equations in centimeter-gram-second units. The final position d of the proton in the image plane at the detector will be

$$d = d_0 + \Delta d = \mathcal{M}x_0 + r_d \delta\alpha, \quad (2)$$

where x_0 is the initial transverse position of the proton in the plasma, d_0 is the undeflected proton position in the detector plane accounting for magnification $\mathcal{M} \equiv (r_s + r_d + l_{\text{path}})/r_s \approx (r_s + r_d)/r_s$, and Δd is the displacement due to the deflection of protons by electromagnetic fields in the plasma. Thus, the path-integrated fields can be inferred from

$$\int_0^{l_{\text{path}}} ds \left[E_x + \frac{(\mathbf{v}_p \times \mathbf{B})_x}{c} \right] = \frac{m_p v_p^2 r_s + r_d}{e r_s r_d} (x - x_0), \quad (3)$$

where $x = d/\mathcal{M}$ is the deflected position rescaled to the plasma plane provided that the initial and final positions x_0 and x of the protons are known. The salient problem, which is considered in Sec. III, is then inferring the displacement of the protons from the proton-fluence inhomogeneities that are directly measured.

A useful metric for classifying different types of proton-fluence inhomogeneities that can arise due to these proton displacements is the *contrast parameter*

$$\mu \equiv \frac{r_d \delta\alpha}{\mathcal{M} \ell_{EM}} \sim \frac{\delta\Psi}{\Psi_0}, \quad (4)$$

where Ψ_0 is the mean proton fluence and $\delta\Psi$ is the magnitude of the inhomogeneities. For $\mu \ll 1$, the relation between the path-integrated fields and inhomogeneities is approximately linear, and the measured proton-fluence distribution is proportional to the path-integrated charge (for purely electrostatic fields) distribution or current-density (for purely magneto-static fields) distribution, respectively. As μ increases, the proton-fluence distribution becomes spatially distorted compared to the path-integrated charge-density and current-density distributions, with regions of focused and defocused fluence; however, qualitatively the image is still similar to these density distributions. When μ becomes larger than some critical value $\mu_c \sim 1$, proton trajectories cross before reaching the detector, leading to the formation of so-called caustic

structures in images (Kugland, Ryutov *et al.*, 2012). Caustics, which are more commonly encountered and discussed in the field of geometric optics, have specific characteristics (for example, their profile and scale) that are insensitive to the characteristic electromagnetic fields that are being imaged, so the presence of caustics in a proton image makes the interpretation of the image more difficult. The contrast parameter μ and caustic formation are important concepts in the theory of proton-imaging analysis; a more detailed exposition of them is given in Sec. III.C.3.

Proton imaging has several advantages over other methods for measuring electromagnetic fields in HED plasmas and is the only practical means for measuring electric fields. Magnetic flux (“*b*-dot”) probes (Everson *et al.*, 2009), which consist of one or more loops of wire inserted into the plasma to measure magnetic flux through Faraday’s law, are frequently used in plasma experiments. However, they are perturbative in typical HED plasma experiments since their spatial extent is often a significant fraction of the size of such plasmas, which also makes their spatial resolution poor. Additionally, they do not measure electric fields and are sensitive to electromagnetic pulses (EMPs) from high-intensity laser-target interactions (Bradford *et al.*, 2018). Faraday-rotation or Cotton-Mouton polarimetry (Segre, 1999) are noninvasive laser-based optical probe diagnostics of magnetic fields that are insensitive to EMPs, but since the former measures $\int n_e B_{\parallel} dz$ (where B_{\parallel} is the component of the magnetic field parallel to the probe beam) and the latter measures $\int n_e B_{\perp}^2 dz$ (where B_{\perp} is the magnitude of the perpendicular field), the two approaches require a simultaneous density measurement. As with *b*-dot probes, polarimetry does not measure electric fields. Polarimetry measurements are also generally limited to underdense plasmas and can be difficult to implement due to refraction in plasmas with the large density gradients commonly found in HED experiments. The Zeeman effect can be used to measure magnetic fields (Stamper, 1991) by measuring the splitting of spectral lines, but field magnitudes in HED experiments are typically too small to resolve with this technique, or the measurements are highly limited (Rosenzweig *et al.*, 2020). Similarly, Thomson scattering, which measures scattered laser light from a plasma, can be used in principle to measure magnetic fields, but the required field strengths are much larger than those achieved in most HED experiments (Froula *et al.*, 2011). As a result, proton imaging has become a standard diagnostic of electromagnetic fields at many HED facilities.

Additional historical context for the development of proton imaging is presented in Sec. I.B. In Sec. II we discuss key components of experimental techniques and design for proton-imaging setups, including a comparison of proton sources and detectors. In Sec. III we present an overview of the theory of proton-imaging analysis, including both forward and inverse modeling. In Sec. IV we survey a wide variety of phenomena that have been investigated using proton-imaging experiments. In Sec. V we discuss the frontiers of proton imaging, including advanced proton sources, detectors, analysis techniques, and setup schemes. Finally, in Sec. VI we summarize our review and discuss the outlook for the field of proton imaging.

B. Historical development

The first charged-particle-imaging experiments measuring electromagnetic fields in plasmas date back to the 1970s (Mendel and Olsen, 1975) and utilized accelerators as a source of ions. However, the long pulse length of ions from conventional accelerators and the difficulty of combining externally produced ion beams with experiments limited the application of this technique to HED plasmas. Not until the discovery of laser-driven, MeV proton sources was proton imaging regularly employed on HED facilities.

The development of multi-MeV, pointlike proton sources useful for proton imaging was first demonstrated two decades ago (Borghesi *et al.*, 2001). The proton sources were generated by focusing high-intensity lasers onto thin foils; this generated MeV protons via a process called target normal sheath acceleration (TNSA), which was first described by Wilks *et al.* (2001). Radiochromic film stacks (Borghesi *et al.*, 2001) and allyl diglycol carbonate, Columbia resin no. 39 (CR-39) nuclear-track detectors (Clark *et al.*, 2000; Maksimchuk *et al.*, 2000) were both initially used to image the protons, but the low-fluence saturation limit of CR-39 and issues with data interpretation (Clark *et al.*, 2006; Gaillard *et al.*, 2006) led to its disuse for TNSA protons. Soon after these initial experiments, the first uses of TNSA-generated protons for measuring electromagnetic fields in HED plasmas were reported, with electric fields being characterized in ICF and laser-produced plasmas (Borghesi *et al.*, 2001, 2002b). Meshes to directly measure the proton deflections were first added a few years later (Mackinnon *et al.*, 2004).

Around the same time that TNSA proton sources were being developed, a second type of laser-driven proton source based on capsules filled with deuterium helium-3 (D^3He) gas was being developed in connection with direct-drive ICF experiments (Li *et al.*, 2002; Smalyuk *et al.*, 2003). When imploded, these capsules emit ~ 3 and ~ 15 MeV protons as fusion by-products. A distinctive feature of D^3He -capsule proton sources is their narrow energy spectra, which contrasts with the broadband proton energy spectra generated by TNSA. Compared to TNSA proton sources, the proton fluence from D^3He sources is significantly lower, requiring the use of low-fluence CR-39 detectors (Séguin *et al.*, 2003). In 2006, the use of a D^3He proton source to image electromagnetic fields in laser-produced plasmas was first reported (Li *et al.*, 2006b).

A key challenge of proton imaging is recovering the path-integrated electromagnetic fields based on the measured proton fluence. The first approach chronologically, taken shortly after the initial deployment of high-intensity laser sources, was the development of numerical forward models that take a known electromagnetic-field configuration and generate a synthetic proton-fluence image that can be compared to the measured image. Quantitative analysis of such a comparison allowed for the optimal choice of characteristic parameters of the proposed electromagnetic field. These initial modeling efforts were employed to measure electric fields using data from TNSA proton sources (Borghesi *et al.*, 2003; Romagnani *et al.*, 2005) and, with subsequent application, to determine electric and magnetic fields probed with D^3He

TABLE I. Comparison of the typical proton-imaging source properties and characteristics. CPA, chirped pulse amplification.

| | TNSA | D ³ He |
|--|--|---|
| Typical laser driver (energy, pulse width) | > 50 J, ~ps ~1 J, ~30 fs | ~10 kJ, ~ns |
| Facility required | High-energy CPA laser | ICF facility [such as OMEGA (Boehly <i>et al.</i> , 1995), NIF (Moses <i>et al.</i> , 2009), LMJ (Lion, 2010), Gekko-XII (Yamanaka <i>et al.</i> , 1981), and Shenguan-II (He, 2016)] |
| Typical target | Flat, metallic foil, ~10–25 μm thick | D ³ He-filled capsule (18 atm) Capsule wall thickness ~2.0 μm Capsule diameter ~420 μm |
| Source size | ~10 μm | ~40 μm (burn FWHM) |
| Source time; cf. laser driver | Instantaneous | ~450 ps (capsule bang time) |
| Proton temporal spread at source | ~ps | 100 ps |
| Spectral characteristics | Maxwellian-like up to ~60 MeV | DD, ~3.3 MeV D ³ He, ~14.7 MeV |
| Typical proton yield | 10 ¹¹ –10 ¹³ (total in the beam) | DD, ~1 × 10 ⁹ D ³ He, ~2 × 10 ⁹ |
| Proton directionality | Beam with ~30° divergence | 4π emission |
| Typical detector | RCF stack | CR-39 |

sources (Li *et al.*, 2006b). Analytical models relating electromagnetic fields to their proton images were also developed at around the same time (Borghesi *et al.*, 2002b; Romagnani *et al.*, 2005), but the first detailed discussion of the analytical theory of proton imaging was not published until the work of Kugland, Ryutov *et al.* (2012). Obtaining direct measurements of the fields required the development of techniques to extract proton deflections from the proton-fluence profiles. This was first done through proton deflectometry (Romagnani *et al.*, 2005; Li *et al.*, 2007; Petrasso *et al.*, 2009), in which a mesh placed between the proton source and detector provided a direct reference for how the protons were deflected. In many experiments, though, adding a mesh is not practical. For these cases, a variety of numerical inversion schemes were developed and first reported in 2017 (Bott *et al.*, 2017; Graziani *et al.*, 2017; Kasim *et al.*, 2017).

II. EXPERIMENTAL TECHNIQUES

Proton imaging has developed significantly over the past two decades and is now commonly used at many HED experimental facilities. In this section we describe each component needed to perform the measurement. First, we discuss different proton sources and the methods for producing protons, as well as the properties of the protons generated. Second, we describe the standard detectors used to measure the protons and the trade-offs associated with each. Last, we discuss how the geometry of the experiment affects proton measurements and additional considerations when one designs proton-imaging setups.

A. Proton sources

There are two main types of proton sources that have been developed for proton-imaging experiments: (1) proton beams accelerated by a high-intensity laser through the so-called TNSA mechanism, and (2) protons produced from nuclear fusion reactions resulting from laser-driven implosions of D³He-filled targets. In the following we review the general

characteristics of these two sources, which differ significantly in terms of properties and capabilities. Table I comparatively summarizes the main properties of these sources.

1. Target normal sheath acceleration

Since the first reports of multi-MeV proton beams produced from laser-irradiated foils in 2000 (Clark *et al.*, 2000; Maksimchuk *et al.*, 2000; Snavely *et al.*, 2000), proton acceleration has been one of the most active fields of research employing high-power, short-pulse lasers (Macchi, Borghesi, and Passoni, 2013). TNSA is the mechanism that has been most studied and has been widely employed for applications. TNSA was proposed as an interpretative framework (Hatchett *et al.*, 2000; Wilks *et al.*, 2001) of the multi-MeV proton observations reported by Snavely *et al.* (2000), obtained on the NOVA Petawatt laser at Lawrence Livermore National Laboratory (LLNL). The scheme typically employs mid-infrared (0.8–1 μm wavelength), multi-hundred-TW short-pulse (30 fs–10 ps pulse duration) laser systems that generate on-target intensities in the range of 10¹⁹–10²¹ W cm⁻².

A schematic of the TNSA process is shown in Fig. 2. A high-intensity laser pulse interacts with a solid foil target with a thickness of around a few microns. At these intensities, the laser pulse, focused on the foil surface, can efficiently couple energy into relativistic electrons, mainly through ponderomotive processes [such as the $J \times B$ mechanism (Kruer and Estabrook, 1985)]. The average energy of the electrons is typically of the order of MeV, so their collisional range is much larger than the foil thickness, and they can propagate to the rear of the target. As the electrons expand into the vacuum they establish a space-charge field that ionizes the rear surface and drives the acceleration of ions from surface layers. While a limited number of energetic electrons will effectively leave the target (Link *et al.*, 2011), most of the hot electrons are confined to within the target volume by the space charge and form a sheath extending by approximately a Debye length $\lambda_D = \sqrt{k_B T_{e,\text{hot}} / 4\pi n_{e,\text{hot}} e^2}$ from the initially unperturbed rear

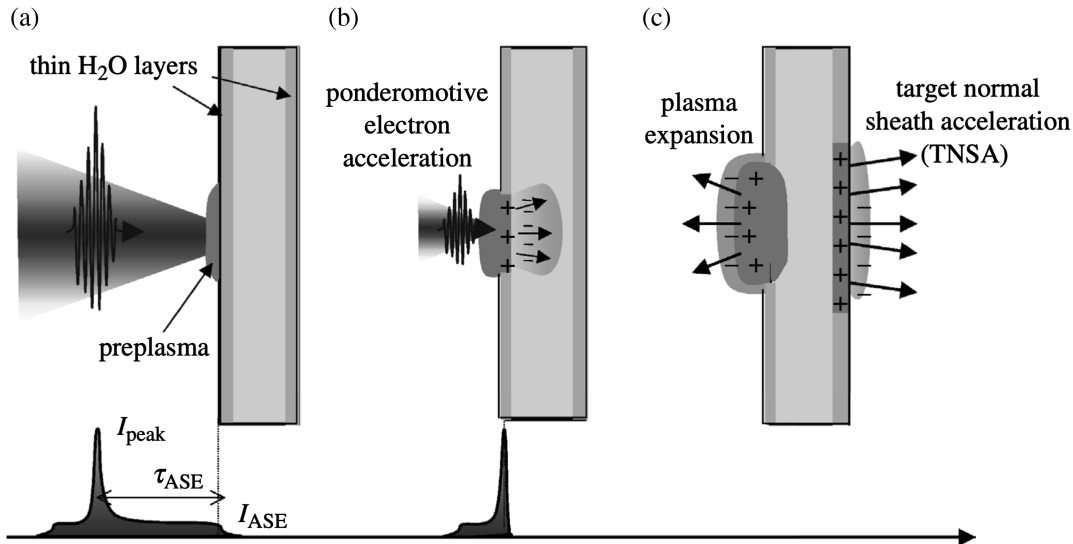


FIG. 2. Schematic of the main processes involved in the TNSA mechanism. (a) First, a laser prepulse impinges upon and heats a thin target to form a preplasma. The target contains layers of proton-rich hydrocarbons as common contaminants. (b) Second, the peak of the pulse arrives, efficiently heating electrons to relativistic temperatures. These electrons expand and propagate through the target. (c) Third, the hot electrons emerge into the vacuum and form an electron sheath with a strength of \sim TV/m. This field ionizes the rear surface such that ions are accelerated to multi-MeV energies. Adapted from McKenna *et al.*, 2006.

surface, where k_B is Boltzmann's constant and $n_{e,\text{hot}}$ and $T_{e,\text{hot}}$ are the density and temperature of the superthermal (*hot*) electrons. The electric field in the sheath is proportional to $(n_{e,\text{hot}}T_{e,\text{hot}})^{1/2}$ (Mora, 2003; Schreiber *et al.*, 2006). For a typical interaction, the sheath field reaches amplitudes in the TV/m range. Under standard experimental conditions, contaminant layers (hydrocarbons, water, etc.) exist on the surface of any target (Allen *et al.*, 2004). Therefore, protons are most efficiently accelerated by TNSA due to their favorable charge-to-mass ratio and shield other ion species from experiencing the strongest accelerating fields. This makes TNSA a robust, efficient, and easily implementable mechanism for accelerating protons.

The energy spectra of TNSA proton beams are broadband, typically with an exponential profile up to a high-energy cutoff; see Fig. 3(a). The highest TNSA energies reported are of the order of 85 MeV (Wagner *et al.*, 2016), obtained with large PW-class laser systems, and available data generally show that at equal intensities longer pulses (\sim picosecond

duration) containing more energy generally accelerate ions more efficiently than pulses with widths of tens of femtoseconds (Macchi, Borghesi, and Passoni, 2013). However, using state-of-the-art femtosecond systems and stringent control of the laser properties has recently allowed the energies of accelerated protons to be increased up to 70 MeV (Ziegler *et al.*, 2021).

Reported scaling laws for the proton energies as a function of laser intensity vary from a ponderomotive $I^{0.5}$ dependence for subpicosecond pulses (Macchi, Borghesi, and Passoni, 2013) to a near-linear dependence observed for ultrashort laser pulses over restricted intensity ranges (Zeil *et al.*, 2010); see Figs. 3(b) and 3(c). Superponderomotive scaling for multi-kilojoule, multipicosecond lasers has also been reported (Flippo *et al.*, 2007; Mariscal *et al.*, 2019). Nevertheless, secondary factors such as target thickness, target material, target size, and laser contrast (Kaluzka *et al.*, 2004; Fuchs *et al.*, 2007; Yogo *et al.*, 2008; Schollmeier *et al.*, 2015) also play an important role in TNSA accelerating energy performance.

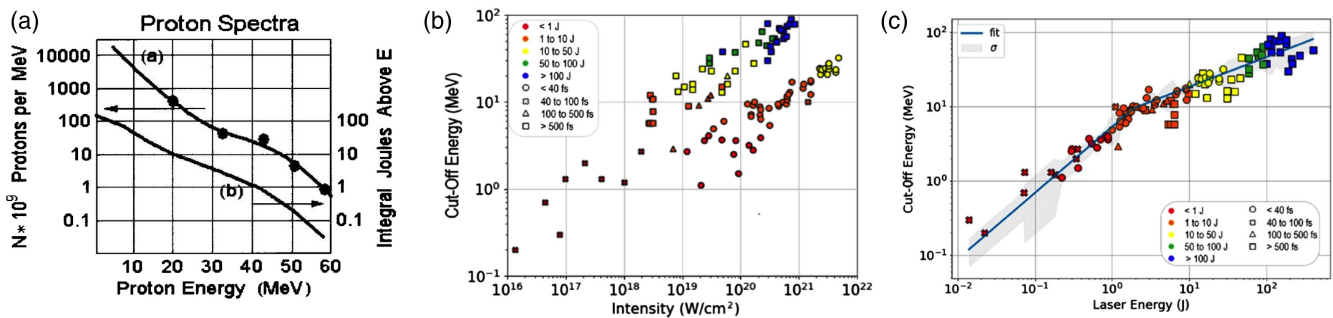


FIG. 3. (a) TNSA spectrum obtained on the NOVA Petawatt laser at LLNL, expressed in the number of protons per MeV (left scale). Adapted from Snavely *et al.*, 2000. TNSA cutoff energies plotted against (b) laser intensity on target and (c) laser energy. The data are from a select number of experiments where a scan in laser energy was performed. Adapted from Zimmer *et al.*, 2021.

Having a sharp density interface at the rear target surface is key to efficient TNSA acceleration. For pulses with a duration longer than ~ 1 ps, the rear target surface evolves before the electrons associated with the peak intensity arrive, limiting the maximum acceleration (Schollmeier *et al.*, 2015; Campbell *et al.*, 2019).

If the laser pulse has a significant “prepulse,” or energy arriving before the peak of the pulse, ionization of the material can begin before the main peak of the pulse arrives; see Fig. 2. The effect of the prepulse can be twofold: it can create a plasma at the front of the target that alters the electron heating (usually enhancing the efficiency), and it can send a shock through the target that breaks out to form a preplasma on the rear surface. Additionally, the interaction that is being probed may also cause preplasma at the rear of the target. In either case, this preplasma at the rear surface can inhibit proton acceleration (Kaluzza *et al.*, 2004; Fuchs *et al.*, 2007; Higginson *et al.*, 2021). For this reason, a shield to protect the proton source foil is often used to prevent these effects (Mackinnon *et al.*, 2006; Zylstra *et al.*, 2012).

The characteristics of the beams accelerated via TNSA are much different than those of conventional rf beams, with some superior properties that are particularly advantageous for use as a backlighter in proton-imaging applications. These result from the short duration of the acceleration process (Fuchs *et al.*, 2006; Schreiber *et al.*, 2006; Dromey *et al.*, 2016) and from the fact that, unlike other ion sources, protons are cold when accelerated with minimal transverse energy spread. The beams are therefore highly laminar (Borghesi *et al.*, 2004) and are characterized by ultralow transverse emittance [as low as 0.004 mm mrad; see Cowan *et al.* (2004)] and by ultrashort (\sim picosecond) duration at the source (Dromey *et al.*, 2016). As a consequence, the emission properties of a TNSA beam can be described in terms of a virtual source that is much smaller than the region from which the protons are emitted and typically located at a small distance in front of the target (Borghesi *et al.*, 2004). The proton-beam properties for imaging have been demonstrated to be optimum for \sim picosecond duration laser pulses (Campbell *et al.*, 2019) to limit emittance growth. If the driving laser pulse duration is longer than ~ 1 ps, magnetic-field instability growth on the rear surface deflects protons as they are accelerated (Nakatsutsumi *et al.*, 2018). Another key characteristic of TNSA proton beams is that they are bright, with

10^{11} – 10^{13} protons per shot with energies $> \text{MeV}$, distributed across a broadband spectrum with a Boltzmann-like distribution. The proton-beam divergence is typically $\lesssim 30^\circ$, with the divergence decreasing with increasing energy (Nürnberg *et al.*, 2009).

The homogeneity of the transverse profile within a beam has been shown to be affected by the laser intensity profile at the target front (Fuchs *et al.*, 2003), as well as by instabilities occurring within the target, particularly within insulators, which tend to degrade the uniformity of the profile (Fuchs *et al.*, 2003; Ruyer *et al.*, 2020). Metallic targets typically induce smoother beams than insulators (Quinn *et al.*, 2011), and are therefore normally preferred for imaging applications.

2. D^3He

A different approach to generating protons is to use the fusion reaction products from an inertial implosion. These sources were first developed in the context of proton backlighters for ICF experiments at the Omega laser facility (Li *et al.*, 2006a, 2006b) and have since been ported to the National Ignition Facility (NIF) (Zylstra *et al.*, 2020). Contrary to the TNSA method, such a backlighter is formed by direct laser irradiation of a capsule filled with D^3He gas.

The D^3He backlighter platform uses a shock-driven implosion mode called an exploding pusher. As schematically illustrated in Fig. 4, the physical process involved in this scheme comprises three steps. First, multiple laser beams directly and symmetrically illuminate a thin-glass-shell capsule surface. Second, the strong laser absorption drives a strong spherical shock propagating radially toward the capsule center. Finally, the converging shock collapses in the center and bounces back, resulting in an increase of the ion temperature and fuel density, which leads to nuclear fusion reactions and burn. The nuclear “bang time” is usually defined as the time of peak fusion yield, and the nuclear “burn time” is defined by the full width at half maximum (FWHM) of the fusion product spectrum.

The nuclear reaction results in the generation of monoenergetic 3.0 MeV DD protons [$\text{D} + \text{D} \rightarrow \text{T} + p$ (3.0 MeV)] and 14.7 MeV D^3He protons [$\text{D} + ^3\text{He} \rightarrow \alpha + p$ (14.7 MeV)], with typical yields of $\sim 1 \times 10^9$. These fusion products and

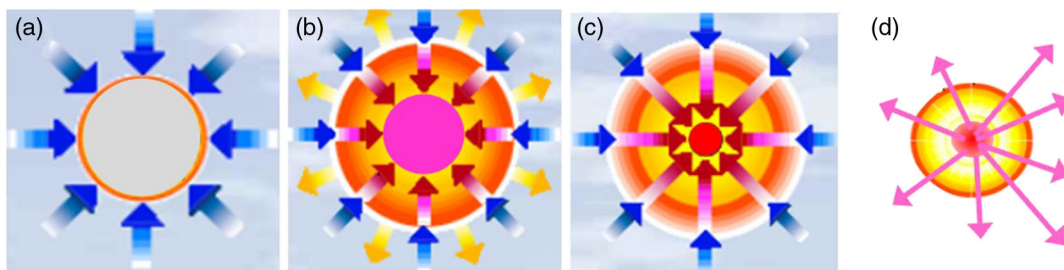


FIG. 4. Schematic of an exploding-pusher mode of capsule implosion and fusion in direct-drive inertial-confinement fusion. (a) Multiple laser beams directly and symmetrically illuminate the thin-glass-shell capsule surface. (b) The explosion of the shell caused by laser energy absorption drives a strong spherical shock propagating radially toward the capsule center. (c) The converging shock collapses in the center and bounces back, resulting in an increase of ion temperature and fuel density, and (d) the facilitation of nuclear fusion reactions and burn.

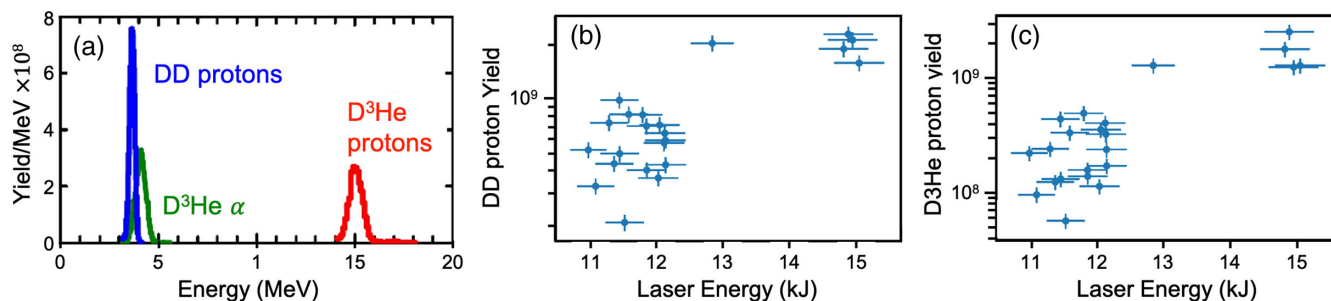


FIG. 5. (a) Typical spectra of fusion products generated in a $D^3\text{He}$ -filled, thin-glass-shell, laser-driven exploding pusher as implemented for backlighters on the Omega laser facility. (b) DD and (c) $D^3\text{He}$ proton yields as a function of laser energy on the capsule. Adapted from Johnson *et al.*, 2021.

relative proton numbers are shown in Fig. 5(a). More recently a tripartite backlighter platform utilizing a $DT^3\text{He}$ capsule implosion was developed that provided 9.5 MeV deuterons from $T + ^3\text{He} \rightarrow \alpha + d$ (9.5 MeV), in addition to the 3.0 MeV DD and 14.7 MeV $D^3\text{He}$ protons (Sutcliffe *et al.*, 2021). Note that the interaction of the drive lasers with plasmas ablated from the capsule surface can generate hot electrons that escape from the capsule surface, which can lead to electric charging of the imploding capsule that can “upshift” the proton energies. For a typical implosion driven by a laser intensity of $10^{15} \text{ W cm}^{-2}$, \sim megavolt electric potentials resulting in an $\sim 0.5\text{--}1.0$ MeV acceleration of fusion protons have been measured (Hicks *et al.*, 2000; Rygg *et al.*, 2008).

The typical implosion lasers consist of 0.6–1 ns square pulses without phase plates and cumulative energies of ~ 10 kJ. The capsules have diameters of approximately 420 μm , with a wall thickness of ~ 2 μm . The capsule bang time is approximately 450 ps, followed by a ~ 100 ps burn during which the protons are generated. During the implosion the capsules reach a minimum burn size of ~ 40 μm (FWHM), which sets the spatial resolution of the resulting proton beams.

Recent studies have started to explore how proton yield from $D^3\text{He}$ sources varies with laser and capsule parameters; see Figs. 5(b) and 5(c). By statistically sampling several hundred backlighter shots, it was found that the total laser energy on the capsule and the asymmetry of the laser drive were the most important predictors of backlighter performance (Johnson *et al.*, 2021). As a result, the best proton yields (both DD and $D^3\text{He}$) can be attained using as many drive beams as possible (at least 9 kJ is recommended) while keeping the capsule illumination as symmetric as possible; see Johnson *et al.* (2021) for details. In general, the combination of high asymmetry and a small number of beams should be avoided whenever possible.

$D^3\text{He}$ protons have several unique features compared to TNSA protons. First, the fusion-generated protons are monoenergetic, with a typical energy uncertainty of about 3% (Li *et al.*, 2006a) due to the finite nuclear burn region and energy straggling on the backlighter. Second, the different characteristic energies of the DD and $D^3\text{He}$ protons naturally result in distinct times of flight for each proton energy, which can provide a temporal resolution of ~ 100 ps. Third, a uniform and symmetric emission of fusion products provides a 4π solid angle isotropic proton fluence, though electric

charging of the capsule may distort this (Manuel, Zylstra *et al.*, 2012).

B. Detectors

Each proton source is associated with a corresponding detector, namely, radiochromic film (RCF) for TNSA protons and CR-39 for $D^3\text{He}$ protons. In Secs. II.B.1–II.B.3 we discuss the properties and characteristics of these detectors, which play a key role, along with the beam properties, in determining the features of the proton images. Mention is also made of other detectors that have been used, albeit less frequently.

1. Film

RCFs are commonly used in dosimetry for a wide range of radiation sources (electrons, protons, and photons) for medical, industrial, and scientific applications. This is a high-dose, high-dynamic-range film that is widely used in a clinical context for x-ray dosimetry (Niroomand-Rad *et al.*, 1998). RCF has become a popular choice for spectral and angular characterization of laser-driven proton beams (Nürnberg *et al.*, 2009; Schollmeier *et al.*, 2014), and the main detector of choice for TNSA-based proton imaging, thanks to its ease of use and effective performance at the particle fluences of typical experimental arrangements. The films consist of one or more active layers containing a microcrystalline monomeric dispersion buried in a clear plastic substrate. Different types are available, under the commercial GafChromic name, that have varying active layer thicknesses and compositions and consequently different sensitivities to ionizing radiation. Currently popular varieties are HD-V2 and EBT3.

There are a number of features that make RCF particularly attractive. RCF is a passive detector, the color and optical density of which is immediately, permanently, and visibly changed upon irradiation as a consequence of polymerization processes in the active layer, without the need for processing. The subsequent change in optical density can be calibrated against the radiation dose absorbed in the active layer of the film. Therefore, it is possible to extract information on particle fluence within the layer.

RCF can be digitized using inexpensive commercial photo-scanners (photo-type flatbed scanners), which are fast and offer high spatial resolution (1600 dpi, or 63 dots/mm, resulting in a resolution of 16 μm in most cases) and 16 bits

per channel. The intrinsic spatial resolution of RCF is higher (typically of micron scale) than the resolution of the scanners. RGB scanning provides separate color channels and produces images with different contrasts or sensitivities and provides options for further extending the dynamic range of the film. Conversion of the scanned images into doses requires a prior calibration of the film, which is typically obtained by exposing the films to known doses delivered by well-characterized fluxes of protons in conventional accelerators (Chen *et al.*, 2016; Bin *et al.*, 2019; Xu *et al.*, 2019).

In standard experimental configurations, RCFs are used in a stack arrangement such that each layer acts as a filter for the following ones in the stack. Sometimes additional filter layers, typically aluminum foils, are used as spacers. The signal in a given film within the stack will be due only to protons having energy $E \geq E_B$, where E_B is the energy reaching the Bragg peak within the active layer of the film. In the first approximation, for a Boltzmann-like spectrum such as those typically produced by TNSA, the dose deposited in a layer can be taken as deposited mostly by protons with $E \sim E_B$. As we see in Sec. II.C.4, this property is at the basis of the unique temporal characterization capabilities of TNSA proton imaging. An example of an RCF stack is shown in Fig. 6 and illustrates the color change of the film and the reduction in the beam divergence at higher proton energies.

2. CR-39

The D^3He backlighter is ideally complemented by imaging detectors made of CR-39 (Séguin *et al.*, 2003). Although the process of reading out the data recorded on CR-39 is complicated (as we later discuss), the great advantage is that it records the exact position of every individual incident charged particle in the detector plane to an accuracy of $\sim 2 \mu\text{m}$, as long as the maximum incident particle fluence is smaller than about 10^6 per cm^2 . These fluence limit and saturation effects at higher flux (Gaillard *et al.*, 2007) are why CR-39 is not typically used for TNSA proton-beam detection.

CR-39 polymer is part of a class of solid-state nuclear-track detectors that have been used for decades in many high-energy

particle counting applications, from radioactive dating to cosmic rays and neutrons; see Fleisher, Price, and Walker (1965) and references therein. It has the useful property of being relatively insensitive to other forms of ionizing radiation, like gamma rays, x rays, or electrons, and is nearly 100% efficient at detecting ions in a given energy range. Consequently, CR-39 has become the workhorse for D^3He capsule backlighter experiments. It has also been used to calibrate other detectors due to its high efficiency and known response (Harres *et al.*, 2008; Mančić *et al.*, 2008). CR-39 is typically arranged in a two-layer stack with associated filters such that one layer is sensitive to 3.0 MeV DD protons and one layer is sensitive to 15 MeV D^3He protons.

CR-39 is a transparent plastic with chemical composition $C_{12}H_{18}O_7$ (Fews and Henshaw, 1982; Séguin *et al.*, 2003, 2016). A charged particle of appropriate energy passing through it leaves a trail of damage along its path in the form of broken molecular chains and free radicals. The amount of local damage along the path is related to the local rate at which energy is lost by the particle (dE/dx , where x is the distance along the path). The length of the path is the range of the particle in the plastic. Particle paths can be made visible by etching the CR-39 in NaOH (Fews and Henshaw, 1982; Gaillard *et al.*, 2007); the etch time is typically between 0.5 and 5 h (based on characteristics of the experiment such as the expected backlighter yield). The surface of the plastic is etched away at a “bulk etch rate,” while damaged material along a particle path etches at a faster “track etch rate.” If a particle path is normal to the plastic surface, the result of etching is a conical pit, or “track,” with a sharply defined, round entrance hole.

Retrieving information about all individual particle tracks in an exposed piece of CR-39 involves scanning the entire CR-39 surface with an automated microscope system. The bottom panel of Fig. 7(c) shows a sample microscope image of D^3He -proton tracks, each of which appears as a dark circle on a light background. The location of each pit shows where a proton entered, and its diameter provides a measure of dE/dx for the proton. Since dE/dx is different for particles of a given type but different energies, the diameter can provide a measure of particle energy (after passing through any filters in the detector pack). dE/dx is also different for different particle types, so diameters can often be used to identify the particle type if the energy is known (see Fig. 8), or to estimate the energy if the particle type is known (Sinénian *et al.*, 2011; Zylstra *et al.*, 2011; Lahmann *et al.*, 2020). One can use not only different particles or source energies to form images at different times [due to the time of flight; see Li *et al.* (2009)] but also the known down-scattered energies of one of the monoenergetic particles to produce separate images of the same target at the same time; see Fig. 7.

The optical magnification used in the scanning microscope system is usually (but not necessarily) chosen so that one camera frame covers the area that will be used for one pixel in the final desired proton image of particle fluence versus position. That area is often chosen to be about $300 \times 300 \mu\text{m}^2$. Each such camera image is evaluated with special algorithms that identify every individual track and determine its position coordinates, its diameter, its optical contrast, and its

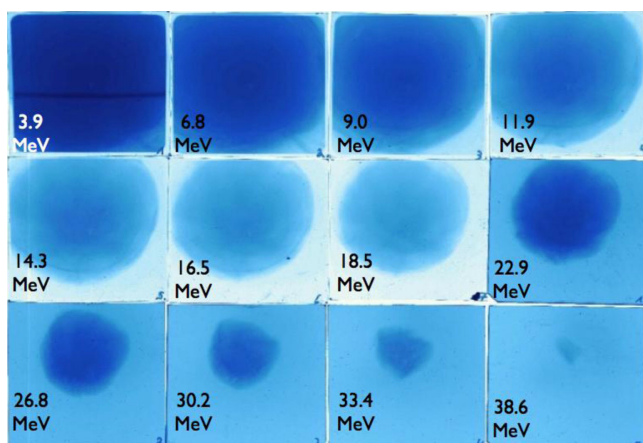


FIG. 6. RCF stack obtained at PHELIX, consisting of seven films of the type HD-810 and five films of the type MD-55. The proton Bragg peak energy is given for each film layer. Adapted from Bolton *et al.*, 2014.

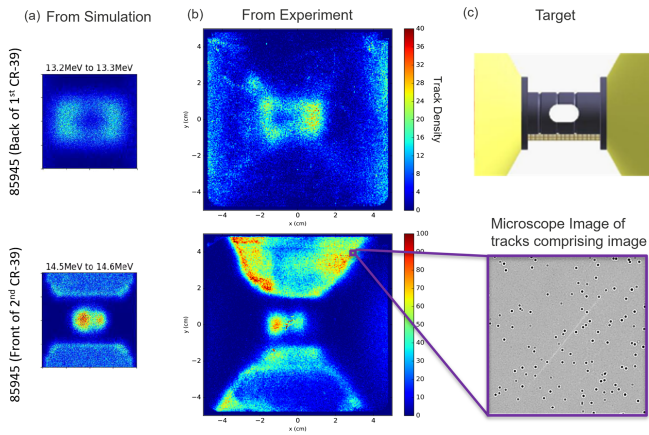


FIG. 7. Proton images using a D^3He source. (a) Synthetic proton images of the target shown at the top of (c), several nanoseconds after lasers have driven shocks into the gray tube from either end. The top image is of 13 MeV protons, and the bottom image is of 14.7 MeV protons. These are the detected energies from protons born at 14.7 MeV and down scattered in energy by the target, allowing different aspects of the target to be imaged with a monoenergetic source. (b) The same images from the experiment taken from a two-piece stack of CR-39. The top image of down-scattered 13 MeV protons is from the rear side of the first piece of CR-39, while the bottom image of 14.7 MeV protons is from the front side of the second piece of CR-39. The bottom image of (c) shows an enlargement of CR-39. Each dark circle is a particle track, and the faint diagonal line is due to laser light from a microscope’s autofocus mechanism. This image corresponds to about $1.6 \times 10^{-4} \text{ cm}^2$, which is equivalent to 15% of the area of one pixel in the experimental images. Adapted from Lu *et al.*, 2020.

eccentricity (Séguin *et al.*, 2003). All of these measured parameters are recorded, and the microscope moves on to the next frame, continuing until the entire surface is covered. The resultant “scan data” file is saved for later processing, in which the final proton image is made by going through all of the recorded track information after deciding which display resolution is desired (frequently one microscope frame for each pixel) and counting the number of tracks in each “pixel” area that satisfies carefully chosen limits on diameter, contrast, and eccentricity (Séguin *et al.*, 2003). Examples are given in Sec. IV.I.

3. Other detectors

While passive, single-use detectors such as RCF and CR-39 have been used in the vast majority of proton-imaging experiments thus far, the use of microchannel plates (MCPs) has been also reported in the literature. MCPs, which are high-gain, spatially resolved electron multipliers (Bolton *et al.*, 2014), have often been used in proton acceleration experiments, mostly in the dispersion plane of a magnetic spectrometer or Thomson parabola (Harres *et al.*, 2008). An arrangement reported by Sokollik *et al.* (2008) extended this use to a streaked deflectometry approach in which a TNSA beam is analyzed, after backlighting a target, in a magnetic spectrometer coupled to an MCP. Use of MCPs as a proton-imaging detector in a standard projection arrangement was

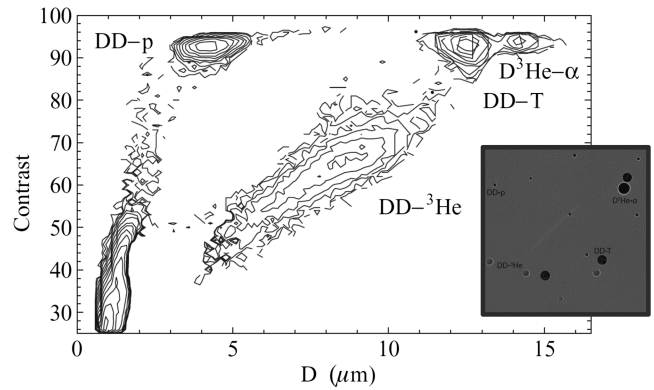


FIG. 8. Contour plot of the number of tracks vs the track contrast and diameter for the piece of CR-39 shown in the inset. The four particle species visible are labeled on the plot (compare to the inset image). Intrinsic CR-39 noise appears in the low-contrast low-diameter regime. Contours represent a constant number of tracks per unit contrast and diameter; the values of this quantity corresponding to plotted contours form a geometric series with a ratio of 2. As defined in this review, a high contrast number is a dark track, while a low contrast number is a light track. Adapted from Zylstra *et al.*, 2011.

also reported by Sokollik *et al.* (2008). In this case the selection of a temporal snapshot is done by temporal gating of the MCP on nanosecond timescales, which is reflected in a temporal resolution of $\sim 60 \text{ ps}$ at the interaction plane and significant integration of the investigated ultrafast phenomenon (the explosion of a laser-irradiated water droplet).

Initial tests with scintillator plates (Tang *et al.*, 2020) have indicated that by selecting appropriate detector parameters these can be used as an alternative to RCF, with the advantage of being suited to repeated use. The main disadvantages of scintillator detectors for proton imaging are (1) the energy resolution is reduced compared to RCF due to the thickness of the detector material, and (2) it is difficult to extract the signal from different detector layers. A novel setup devised by Huault *et al.* (2019) using a concertina design of scintillators has been used to observe the proton energy-spectra and proton-beam divergence simultaneously. See Sec. V.B for further discussion.

C. Diagnostic geometry and other considerations

A diagram of a typical proton-imaging setup as deployed in an experiment is shown in Fig. 9. The source can be either TNSA- or D^3He -generated protons, with corresponding detectors of either RCF or CR-39, respectively. During an experiment, the protons are emitted by the source, propagate a distance r_s to the interaction region where they acquire small deflections due to the electromagnetic fields, and then travel ballistically a distance r_d to the detector. In a number of experiments (Paudel *et al.*, 2012; Ahmed *et al.*, 2016; Obst-Huebl *et al.*, 2018; Ferguson *et al.*, 2023), self-probing arrangements have also been demonstrated, where the TNSA protons accelerated from a foil are used to probe phenomena initiated by the same laser pulse that has accelerated them, for instance, in parts of the same target from which they are emitted, or in the surrounding medium.

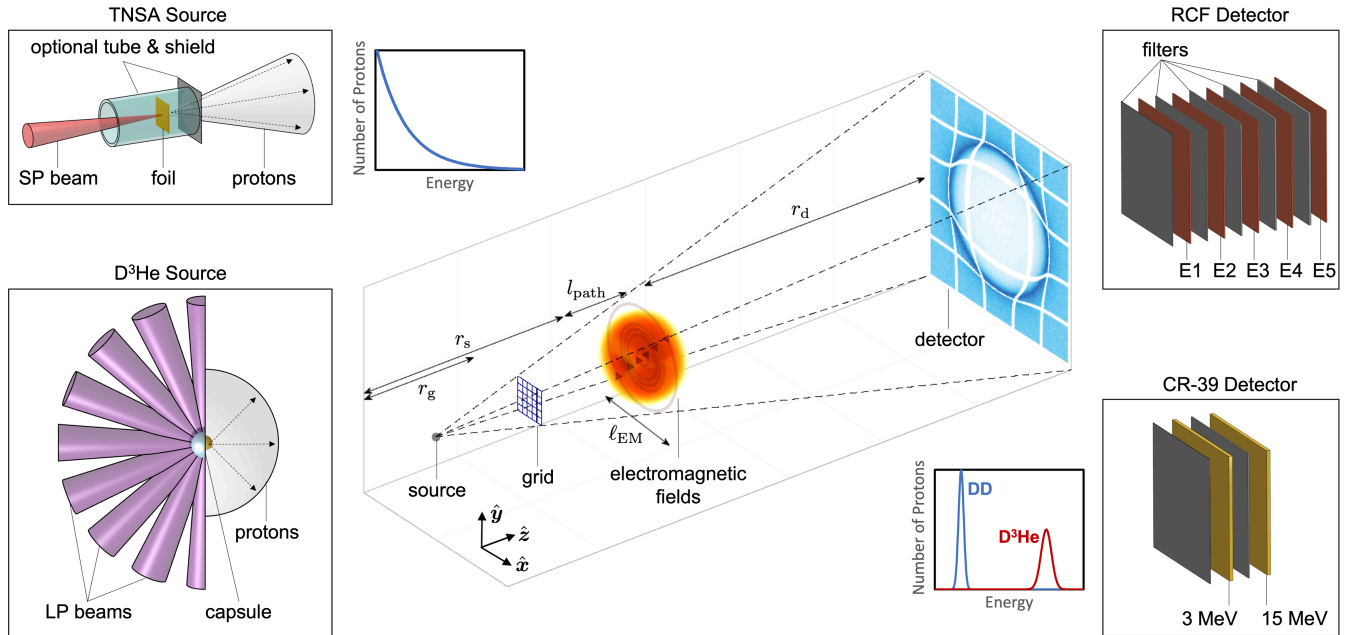


FIG. 9. Diagram illustrating the main components of a proton-imaging diagnostic. Left panels: typical proton sources. TNSA protons are generated using a short-pulse (SP) laser to irradiate a thin foil, which emits protons in a beam with a broadband energy profile. D^3He protons are generated using long-pulse (LP) lasers to drive the implosion on a thin-shell capsule, which isotropically emits monoenergetic DD and D^3He protons as fusion by-products. Right panels: typical proton detectors. TNSA protons are collected on a stack of RCFs that provides energy resolution. D^3He protons are collected on CR-39, one for each proton energy. Center diagram: typical proton-imaging setup in a magnified point-source configuration, including source, optional mesh, the plasma under study, and detector (not drawn to scale).

Typical implementations of TNSA and D^3He sources and examples of detector stacks are also shown in Fig. 9. A standardized TNSA source target has been developed at OMEGA EP (Zylstra *et al.*, 2012), in which a thin foil is mounted within a plastic tube, with a thin protective foil mounted over the end. This shields the TNSA foil from radiation and plasma emerging from the object under study. The tubes are transparent, which allows alignment of the laser focus to the foil via target chamber cameras. The TNSA foil is driven by a short-pulse laser, which can be moderately off axis to allow some setup flexibility. The resulting protons are emitted in a cone normal to the TNSA foil with a broadband energy distribution.

Likewise, a standard D^3He source capsule has been developed for both OMEGA (Li *et al.*, 2006a, 2006b) and NIF (Zylstra *et al.*, 2020). The capsules are mounted on stalks and driven by a relatively symmetric set (typically > 20) of long-pulse beams, resulting in protons emitted into 4π with monoenergetic energy distributions. A comparison of TNSA and D^3He proton sources and detectors is summarized in Table I.

1. Magnification

Typical setups take advantage of the small source size of the protons and obtain a magnified image onto a larger detector, with magnification

$$\mathcal{M} = \frac{r_d + r_s + l_{\text{path}}}{r_s} \approx \frac{r_d + r_s}{r_s}. \quad (5)$$

Such a setup is often used to magnify the image from the plasma size (millimeters to 1 cm) to the detector size (typically several centimeters). The magnification also improves the spatial resolution at the plasma plane by a factor \mathcal{M} compared to the detector's spatial resolution. Note that r_d is in principle different for each layer in the detector stack. This can be especially important for the analysis of TNSA detector stacks, which can have a large number of layers. Additionally, in experiments where the interaction length l_{path} is large, there can also be a significant variation in \mathcal{M} . An example of this is discussed in Sec. IV.G.

Experimental design should consider the size of the interaction such that the proton beam has expanded to overfill the region of interest. A small-angle approximation is often used to assume that the proton beam along the probing axis travels the same distance as the protons at the edge of the detector (or the beam if it is smaller). TNSA proton beams typically have a divergence of less than 30° , meaning that the small-angle approximation is reasonable in most cases, whereas the D^3He implosion is an isotropic source, so a limited solid angle should be used. Similarly, when calculating the energy of the protons for a particular RCF stack layer, the extra distance within material traveled by the protons at the edge of the beam is usually ignored.

2. Meshes and grids

An optional mesh can be used to break the initial proton beam into beamlets, which in a proton deflectometry approach (Mackinnon *et al.*, 2004) facilitates measurement of the fields via a direct tracking of beamlet deflections. The meshes used

are typically commercial transmission electron microscopy grids that are available in a variety of pitches, hole widths, and bar widths and are manufactured from relatively high- Z metals such as copper, nickel, and gold. The thickness of the meshes is typically such that a shadow is imprinted on the proton beam via multiple scattering in the mesh bars (Borghesi *et al.*, 2004). By geometric arguments the mesh magnification of the detector is (see Fig. 9)

$$\mathcal{M}_{\text{mesh,d}} = \frac{r_d + r_s + l_{\text{path}}}{r_g}. \quad (6)$$

The spatial resolution is in turn set by the projection of the mesh period p onto the plasma plane, i.e., $(r_s/r_g) \times p$.

The period of the mesh should ideally be chosen such that a sufficient number of mesh elements is projected across the probed region of interest. The period of the mesh should also be larger than the source size so that the mesh is not overly smeared out when projected.

A variation on the beamlet technique is to use an object (such as a mesh, mask, or pepperpot) to subaperture the proton beam into many beamlets (Sokollik *et al.*, 2008; Johnson *et al.*, 2022), down to a few ‘‘pencil’’ beamlets (Lu *et al.*, 2020), or even just down to a single beamlet (Chen *et al.*, 2020). This allows one to probe areas of specific interest in a limited fashion that is more easily detectable (in terms of deflection) or to streak the beamlet in time.

3. Spatial resolution

As is typical of all projection backlighting schemes, the intrinsic and ultimate spatial resolution of proton images is determined by the size of the proton source. For D^3He capsules this is set by the burn volume of the implosion, which has been measured to be typically 40 μm FWHM (Manuel, Zylstra *et al.*, 2012); see Sec. II.A.2. For TNSA targets the relevant size is instead the ‘‘virtual’’ source size resulting from the beam’s laminarity and emittance (Borghesi *et al.*, 2004); see Sec. II.A.1. This is typically of the order of 10 μm FWHM (Borghesi *et al.*, 2004; Wang *et al.*, 2015; Li *et al.*, 2021), set by the size of the laser focal spot, but can vary from experiment to experiment.

Scattering of the protons in the plasma being probed can (and often does) degrade the spatial resolution from the previously given values, particularly for dense plasmas. The magnitude of the scattering will depend on its density and dimensions, as well as on the proton energy, and typically leads to a Gaussian distribution of angles with some $1/e$ radius θ_{SC} , which can be evaluated using Monte Carlo calculations (Ziegler, Ziegler, and Biersack, 2010) or through empirical formulas (Highland, 1975; Kanematsu, 2008). This causes a resolution degradation characterized by a $1/e$ spatial width of the order of $r_d\theta_{\text{SC}}/\mathcal{M} \sim r_s\theta_{\text{SC}}$ in units of distance in the plasma plane (Li *et al.*, 2006a). For low- Z plasmas with electron number densities that are $\lesssim 10^{20} \text{ cm}^{-3}$, this degradation is typically small compared to the effect of the finite source size [see Bott *et al.* (2017), Appendix B]; however, for experiments with higher-density plasmas ($\gtrsim 10^{22} \text{ cm}^{-3}$), scattering significantly reduces the resolution. In such experiments, scattering is an important effect to take into

consideration for an accurate determination of the fields associated with the proton image; see Sec. III.B.2. A similar effect will be caused by scattering in any protective foil (TNSA sources), although the foil thickness is typically chosen in order to minimize the angular spread of the beam.

By contrast, the characteristics of the detector do not usually have a significant effect on the spatial resolution of proton images. Scattering in the detector, which can occur when protons cross a stack on the way to the layer where they are detected, normally leads to a negligible resolution loss once the magnification is taken into account. Similarly, the intrinsic spatial resolution of the detector is typically high, of the order of microns, and therefore does not contribute to the spatial resolution of the diagnostic when registered back to the plasma plane.

Another potential source of degradation of the spatial resolution arises in the presence of a background magnetic field (as used for magnetized plasma experiments), as the energy-dependent deflection of protons within the energy response curve of a layer may lead to blurring of the proton image along the deflection direction. This effect was discussed by Arran, Ridgers, and Woolsey (2021).

4. Temporal resolution and multiframe capability

There are three primary factors contributing to the temporal resolution of proton images (Sari *et al.*, 2010a):

- (1) The temporal duration of the source δt_p . As discussed, this is of the order of ~ 1 ps for TNSA beams for picosecond drivers [shorter for femtosecond drivers (Fuchs *et al.*, 2006)] and ~ 100 ps for the D^3He capsules. This is the factor that determines the ultimate temporal resolution possible for a proton image and the dominant factor for probing with D^3He protons.
- (2) The transit time δt_t of the protons through the region where the transient fields are located. This is related to the spatial scale over which the fields under investigation extend and is therefore intrinsic to the phenomenon under investigation. If the fields change on the timescale of the proton transit, the information will be temporally averaged over a time

$$\delta t_t \sim \frac{l_{\text{path}}}{v_p} \sim l_{\text{path}} \left(\frac{m_p}{2\epsilon_p} \right)^{0.5}, \quad (7)$$

where ϵ_p and v_p are the energy and velocity of the protons, respectively. For example, for 10 MeV protons crossing a 100 μm region, one has $\delta t_t \sim 2$ ps.

- (3) The time-of-flight uncertainty (from the source to the plasma being probed) δt_d resulting from the energy resolution $\delta\epsilon_p$ of the detector is given by

$$\delta t_d \sim r_s \left(\frac{m_p}{2\epsilon_p^3} \right)^{0.5} \delta\epsilon_p, \quad (8)$$

which can also be of the order of ~ 1 ps. More detailed considerations associated with a multilayer RCF stack are given later.

While δt_d and δt_t are typically not relevant to determine the resolution for D^3He -proton images (where the source duration

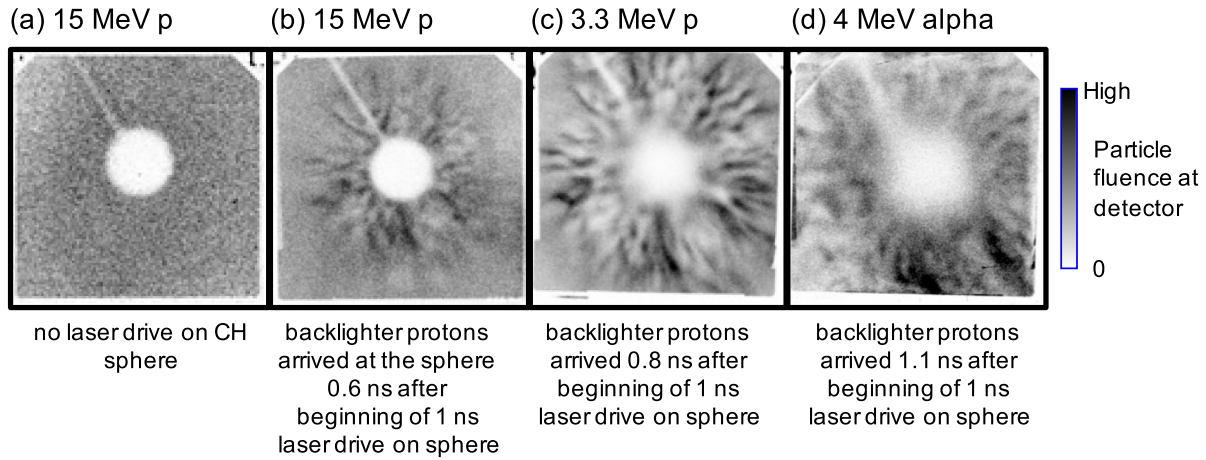


FIG. 10. Proton images of a laser-driven, solid 840 μm diameter CH sphere, made using a setup similar to Fig. 9. (a) Image recorded with no laser drive on the CH sphere. (b)–(d) Images recorded with laser drive for three different particle types and energies. Adapted from Séguin *et al.*, 2012.

is the dominant factor), they all can contribute significantly to the temporal resolution for experiments employing TNSA protons. Under standard experimental conditions and depending on the specific experimental arrangement, this is typically in the range of 1–5 ps.

Both TNSA and D^3He sources emit protons in a burst, which is typically shorter (or much shorter in the case of TNSA) than the time of flight to the plasma r_s/v_p . For $r_s = 1$ cm, for example, this would be ~ 180 ps for 15 MeV protons and ~ 400 ps for 3 MeV protons. Consequently, a multiframe capability can be achieved using energy-resolving detectors (as RCF or CR-39 stacks), where stacking up images from different proton energies provides information on the temporal dynamics of the system over time intervals of the order of hundreds of picoseconds. Obtaining multiple snapshots enables one to follow the temporal dynamics of the same event, which is particularly useful under conditions where there is a pronounced shot-to-shot variability.

For D^3He sources, different frames can be obtained by employing the different fusion products produced during the implosion; see Fig. 9. An example of the application of this capability is provided in Fig. 10. The structure of the detector

pack involves two metal filters and two separate layers of CR-39. The first CR-39 layer is preceded by one of the metal filters, which helps protect the CR-39 from debris while still allowing the detection of ~ 3 MeV DD protons. A second filter is placed before the second CR-39 layer and acts to help slow down the ~ 15 MeV D^3He protons to energies of 1–6 MeV, which is the best energy range for detecting protons on the CR-39.

The broadband spectrum of TNSA sources allows sequential temporal frames to be recorded in consecutive layers of an RCF stack. When using high-energy TNSA protons from a petawatt-class laser system, one can obtain up to several tens of temporally separated proton images of the interaction. In the multiframe approach, every layer is labeled temporally with the time of flight (calculated from the source to the center of the film pack) of the energy at which the relevant response curve is maximized (essentially the energy reaching the Bragg peak in the active layer of the RCF). Figure 11(a) shows the energies reaching the Bragg peak at a certain depth in the RCF pack and the corresponding time of flight for different source-object separations. The active layers of different RCFs (for instance, separated by ~ 100 μm distances

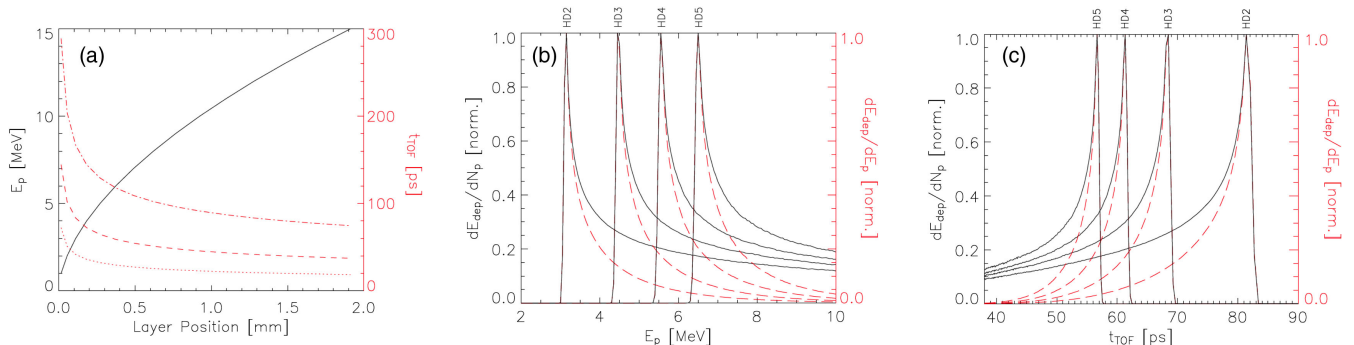


FIG. 11. (a) Bragg peak proton energy vs depth in the RCF stack (solid curve) and corresponding time of flight for three different values of the source-object separation r_s (dotted line, 1 mm; dashed line, 2 mm; dash-dotted line, 3 mm). (b) Normalized energy response curves for an RCF stack made of several layers of HD810 (solid curve). (c) Normalized temporal response curve for the stack configuration in (a) and a source-plasma distance of 3 mm (solid curve). The red dashed curves in (b) and (c) are response curves multiplied by a typical TNSA exponential spectrum with temperature of 2 MeV. Adapted from Romagnani, 2005.

in a stack consisting of HD films) will therefore contain snapshots taken at discrete time values along the red curves in Fig. 11(a). An example of energy and temporal response for four consecutive layers (the second to the fifth) in an RCF stack is shown in Fig. 11(b) (Romagnani, 2005), based on SRIM (stopping and range of ions in matter) (Ziegler, Ziegler, and Biersack, 2010) calculations. The energy response of a layer is dependent on the spectral profile of the proton beam, and Fig. 11 highlights the difference between the response to a flat spectrum and a more realistic Boltzmann-type spectrum with a finite temperature (which in an experimental setting can be obtained from a dedicated spectral characterization of the proton beam). Taking into account the energy-dependent time of flight from source to object, the energy response of Fig. 11(b) translates into the temporal response for each layer shown in Fig. 11(c). The figure highlights the multiframe capability of the diagnostic arrangement, where each layer primarily contains information about a particular time in the evolution of the transient plasma being probed. As is visible in Fig. 11(a), as the time-of-flight curve becomes shallower for increasing depth, the temporal separation between the snapshots obtained in consecutive layers decreases for deeper layers and higher proton energies. The detector-limited temporal resolution of the snapshots also increases for deeper layers, in correspondence to a more selective energy response. By focusing, for example, on layer HD5 in Fig. 11(a) (red dashed curve), one obtains $\delta\epsilon_p$ (FWHM) ~ 0.2 MeV, which, for $r_s = 3$ mm and employing Eq. (8), corresponds to δt_d (FWHM) ~ 2.5 ps. For deeper layers in the pack δt_d becomes of the order of 1 ps or less, depending on the energy of the protons.

A suitable choice of parameters allows interframe time steps of the order of picoseconds or less to be obtained, as achieved in the data of Fig. 12 (Romagnani *et al.*, 2005). In this experiment r_s was reduced to 1 mm, which, coupled to a proton spectrum with a cutoff at ~ 12 MeV, leads to ~ 1 ps temporal frame spacing at the higher end of the spectrum. For example, the eighth and ninth layers in an HD pack would select, respectively, energies of $\epsilon_{p_1} \sim 9$ and $\epsilon_{p_2} \sim 10$ MeV, leading to an interframe temporal separation $\delta t_{if} \sim r_s (m_p/2)^{0.5} [(1/\epsilon_{p_1})^{0.5} - (1/\epsilon_{p_2})^{0.5}] \sim 1$ ps. Detecting highly transient features [such as the sheath field in Fig. 12 (c), which was seen to exist for about 1 ps] therefore becomes possible if one carefully times the proton probe relative to the interaction such that protons of sufficiently high energy transit

through the region of interest at the appropriate time; this is done by appropriately adjusting the relative timing of the laser pulse accelerating the probe protons and the interaction pulse [labeled as CPA_1 and CPA_2 in Fig. 12(a)]. Under these conditions the dominant factor in determining the temporal resolution is often the proton transit time δt_t .

When probing ultrafast phenomena, it is often necessary to consider time-of-flight variations across a single RCF layer. These arise from the longer path of protons, propagating obliquely and intercepting the RCF layer at an angle, compared to the protons propagating on axis, which can lead to temporal differences of the order of picoseconds across the RCF layer. This is important, for example, when imaging field structures moving at speeds close to c across the field of view of the proton images (Kar *et al.*, 2007; Ahmed *et al.*, 2016). A modified projection arrangement specifically designed for the detection of ultrafast moving fronts was described by Quinn *et al.* (2009b).

In cases where the field configuration probed is complex and changes on timescales of the order of the interframe separation or faster, additional complications may arise in the interpretation of the RCF data due to the fact that the dose deposited in a specific layer by protons stopping deeper in the stack will carry information on the field distribution at earlier times than the time determined by the Bragg peak energy [Fig. 11(a)]. The identification of these ghosting artifacts (Quinn, 2010) (which will typically be fainter than the main features in a layer) is an important part of the analysis, which is facilitated by the observation of the dynamics over several RCF layers and extended the temporal range. Several deconvolution techniques exist (Breschi *et al.*, 2004; Nürnberg *et al.*, 2009; Kirby *et al.*, 2011) for removing the contribution of higher-energy protons from preceding layers in the context of the spectral characterization of TNSA proton beams, which in principle could be applied for removing temporally spurious contributions in proton-imaging data and for increasing the temporal purity and resolution of single RCF layers. However, this becomes complex in the case of a dynamically changing dose distribution; this approach has not been reported thus far to our knowledge. Instead, forward modeling employing particle tracers and dynamically evolving field distributions (see Sec. III.B) can be used to produce synthetic radiographs for comparison with the experimental data and the identification of overlapping temporal features (Ramakrishna *et al.*, 2008; Kar *et al.*, 2016).

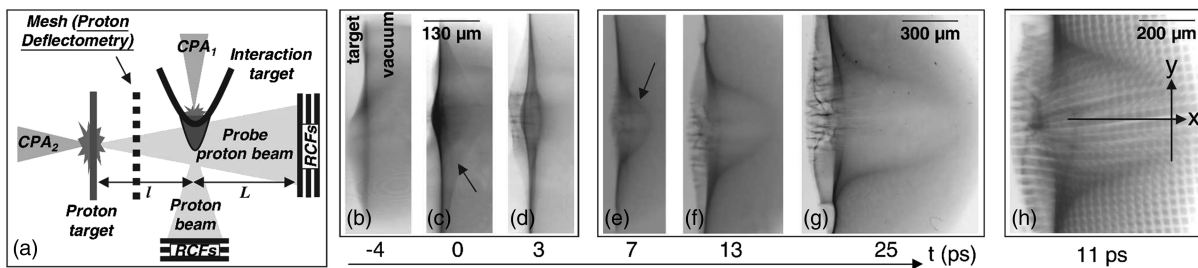


FIG. 12. Proton probing of the expanding sheath at the rear surface of a laser-irradiated target. (a) Setup of the experiment. A proton beam is used as a transverse probe of the sheath. (b)–(g) Temporal series of proton images in a time-of-flight arrangement. The probing times are relative to the peak of the interaction. (h) Deflectometry image where a mesh is placed between the probe and the sheath plasma for a quantitative measure of proton deflections. Adapted from Romagnani *et al.*, 2005.

III. THEORY OF PROTON-IMAGING ANALYSIS

A. Basics

As explained in the [Introduction](#), the physics that underpins the proton-imaging diagnostic is simple. With the exception of interactions with dense HED plasma or matter (see [Sec. II.C.3](#)), the characteristic speeds of imaging-beam protons are sufficiently large that collisional interactions between the beam protons and the plasma being probed are usually negligible ([Kugland, Ryutov *et al.*, 2012](#); [Bott *et al.*, 2017](#)). In addition, the characteristic density of proton-imaging beams is sufficiently low that the beam does not perturb the plasma via either collisionless plasma interactions or space-charge effects ([Kugland, Ryutov *et al.*, 2012](#)). As a result, the protons that constitute typical imaging beams behave like test particles, as they are deflected by electromagnetic forces associated with fields already present in the plasma prior to the arrival of the proton beam. Thus, the proton beam's profile post interaction encodes information about the inherent electric and magnetic fields of the plasma.

The trajectory of charged particles through electric and magnetic fields (and the final velocity of those particles post interaction) can be complicated in the general case of arbitrary proton speeds and characteristic field strengths; proton-imaging setups typically overcome this issue with their use of fast multi-MeV protons (see [Sec. II.A](#)) and careful geometric design to restrict the set of possible proton trajectories. For most laser-plasma experiments currently performed, the magnitude of deflection angles due to plasma-generated electromagnetic fields is small for multi-MeV protons, and thus the electromagnetic fields in the plasma are approximately sampled along the unperturbed, linear trajectories of the beam protons.¹ Therefore, for an incident proton with velocity $\tilde{\mathbf{v}}$ (and whose unperturbed trajectory has position vector $\tilde{\mathbf{x}}$) it can be shown by time integrating the proton's equation of motion that the velocity perturbation $\Delta\mathbf{v}_\perp$ acquired in the directions perpendicular to $\tilde{\mathbf{v}}$ as the proton passes through a plasma containing an electric field \mathbf{E} and a magnetic field \mathbf{B} is

$$\Delta\mathbf{v}_\perp \approx \frac{e}{m_p v_0} \int_0^{l_{\text{path}}} ds \left\{ \mathbf{E}_\perp[\tilde{\mathbf{x}}(s)] + \frac{\tilde{\mathbf{v}} \times \mathbf{B}_\perp[\tilde{\mathbf{x}}(s)]}{c} \right\}, \quad (9)$$

where e is the elementary charge, m_p is the proton mass, c is the speed of light, l_{path} is the distance covered by the proton as it traverses the plasma, $v_0 \equiv |\tilde{\mathbf{v}}|$ is the proton's initial speed, and s is the path length. The deflection angle $\delta\alpha$ of each proton is $\delta\alpha \approx |\Delta\mathbf{v}_\perp|/v_0$; cf. [Eq. \(1\)](#) of [Sec. I.A](#). Because the unperturbed trajectories of beam protons are linear, angular deflections of the proton beam are thus directly relatable to line-integrated electromagnetic fields in the plasma (or, more specifically, to the components of the fields that are perpendicular to the proton beam's incident direction of motion). As a given proton is interacting with electromagnetic fields, it will also acquire a perpendicular displacement $\Delta\mathbf{x}_\perp$ in

¹Several subtle caveats exist to this statement; we discuss them subsequently.

addition to a velocity displacement $\Delta\mathbf{v}_\perp$, which in principle complicates the interpretation of a nonuniform proton-beam profile. However, by ensuring that the distance r_d from the plasma to the detector is much larger than l_{path} (a geometric setup of this form is known as point-projection geometry), it follows that the measured displacement $\Delta\mathbf{d}_\perp$ of protons from their projected position $\mathbf{d}_{\perp 0}$ in the absence of any electromagnetic fields is dominated by the displacement acquired as protons free stream at their slightly perturbed velocity $\Delta\mathbf{d}_\perp \approx r_d \Delta\mathbf{v}_\perp / v_0$, with $|\Delta\mathbf{d}_\perp| \approx r_d \delta\alpha \gg |\Delta\mathbf{x}_\perp|$.

Historically this conclusion has been leveraged to discern properties of the electromagnetic fields in the plasma using a proton beam in two ways. The simpler technique is to introduce a well-defined spatial modulation to the profile of the proton beam prior to its interaction with any electromagnetic fields using a grid (see [Sec. II.C.2](#)): only protons that do not intersect the grid are subsequently detected. Any distortions $\Delta\mathbf{d}_g$ to the grid-induced profile detected post interaction (which provide a direct measure of $\Delta\mathbf{d}_\perp$) can then be attributed to angular deflections caused by electromagnetic fields in the plasma, and the line-integrated values of two components of those fields estimated via

$$\int_0^{l_{\text{path}}} ds \left\{ \mathbf{E}_\perp[\tilde{\mathbf{x}}(s)] + \frac{\tilde{\mathbf{v}} \times \mathbf{B}_\perp[\tilde{\mathbf{x}}(s)]}{c} \right\} \approx \frac{m_p v_0^2}{e r_d} \Delta\mathbf{d}_g. \quad (10)$$

This technique is typically known as proton deflectometry and has been successfully used in a number of different laser-plasma experiments to provide measurements of electromagnetic fields ([Romagnani *et al.*, 2005](#); [Li *et al.*, 2007](#); [Petrasso *et al.*, 2009](#); [Willingale *et al.*, 2011b](#); [Tubman *et al.*, 2021](#)). The main advantage of this approach is its conceptual simplicity. However, it does have a few issues. Determining the exact projection of the initial profile in the absence of any deflections is not always a trivial matter, because confounding factors such as imperfect target fabrication can mean that a deflectometry grid's position is not always consistent from shot to shot. Blurring of the mesh due to the ablation of actual physical grids by strong x-ray radiation that inevitably arises during the course of laser-plasma experiments can also inhibit successful tracking of the grid's distortion ([Johnson *et al.*, 2022](#); [Malko *et al.*, 2022](#)). In some circumstances, the grid itself can become charged, resulting in apparently distorted grids when there is in fact no interaction of the proton beam with plasma electromagnetic fields ([Palmer *et al.*, 2019](#)). The resolution of electromagnetic-field measurements is also limited to that of the grid; this constraint is inevitably much larger than the theoretical resolution that can be achieved given typical proton source sizes; see [Sec. II.A](#). Finally, in cases of highly nonuniform deflections, successfully tracking the grid's distortion is not always possible ([Willingale *et al.*, 2010b](#)).

A second approach that attempts to overcome these issues is to assume approximate transverse uniformity of such beams prior to their interaction with a plasma being imaged (a property of proton-beam sources that typical experimental setups aim to realize; see [Sec. II.C](#)), and thereby quantitatively relate inhomogeneities in the beam profile detected post interaction on a proton image to electromagnetic fields in

the plasma (Kugland, Ryutov *et al.*, 2012; Bott *et al.*, 2017; Graziani *et al.*, 2017; Kasim *et al.*, 2017). The successful interpretation of detected nonuniformities in proton images in terms of the electromagnetic fields associated with them using either of these approaches requires a theoretically grounded analysis methodology. Historically there have been two methodologies that have been used for this interpretation: particle-tracing simulations and analytical modeling. We discuss the two approaches in Secs. III.B and III.C, respectively.

B. Particle-tracing simulations

1. Overview

Analyzing proton images using particle-tracing simulations is typically done as follows. A candidate model for an electromagnetic-field structure in a particular laser-plasma experiment is proposed; the interaction of the proton beam (whose parameters are chosen to be the same as those used experimentally) with that field structure is simulated using a test-particle-tracing code; a simulated proton image associated with that proton beam is then generated; and finally the simulated image is compared with the experimental one, with the candidate model deemed to be reasonable if there is qualitative (or, ideally, quantitative) agreement. Particle-tracing simulations provide a powerful approach for analyzing proton-imaging data because they make relatively few assumptions about the nature of the interaction between the proton beam and the plasma being imaged.

Arguably the most important question to consider when using particle-tracing simulations to analyze proton images involves how to construct an appropriate candidate model for the electromagnetic field. There are two approaches to addressing this question that have been used for analyzing data from previous laser-plasma experiments. The first is to use the electromagnetic fields generated by a high-energy-density-physics (HEDP) code of the relevant laser-plasma experiment. The second involves introducing a physically motivated parametrized model and optimizing the model's parameters using an algorithmic best-fit procedure. These approaches are often used complementarily, with the output of a HEDP code serving as the inspiration for a simpler, parametrized model. The two approaches are discussed in Secs. III.B.3 and III.B.4, respectively. Irrespective of the

approach used to construct the candidate electromagnetic-field model, the successful use of particle-tracing simulations relies upon efficient particle-tracing algorithms; we therefore discuss these algorithms first.

2. Particle-tracing algorithms

The process underpinning a typical particle-tracing algorithm is illustrated in Fig. 13. Particle-tracing simulations typically employ a Monte Carlo method. To begin, synthetic protons are generated at the location of the proton source and assigned a velocity that, aside from being constrained to have a prespecified magnitude and an orientation with a cone of a certain solid angle, is random. These particles are then traced to the compact domain in which the possibly time-dependent electromagnetic fields are defined. In this domain, the non-relativistic equation of motion for protons under the action of the Lorentz force associated with the electromagnetic fields is numerically integrated along particle trajectories. This integration is implemented using efficient numerical schemes in typical particle-tracing simulations so that the simulations can be run quickly for millions of synthetic protons (Birdsall and Langdon, 1985; Welch *et al.*, 2004; Vay, 2008).

Once a given synthetic proton has completed its interaction with the electromagnetic field, the output can then be included in various particle diagnostics: most immediately synthetic proton images, but also other outputs such as deflection maps. The synthetic images can then be compared with experimental ones; for simple electromagnetic-field distributions (see Sec. III.B.4), quantitative comparison metrics between the synthetic and experimental images can then be used to refine the field distribution. There are several bespoke particle-tracing simulation codes optimized for proton-imaging analysis, including PTRACE (Schiavi, 2008), qTrace (Romagnani *et al.*, 2005), the proton-imaging unit of the HEDP code FLASH (Fryxell *et al.*, 2000; Tzeferacos *et al.*, 2015), and PlasmaPy (PlasmaPy Community, 2023).

While the most basic particle-tracing codes typically make several physically motivated assumptions about the proton beam's properties and the physics of its interaction with the plasma through which it is passing, one of the strengths of the particle-tracing approach is that it is often feasible to relax these assumptions. For example, while most proton-imaging particle-tracing codes assume a point source of monoenergetic

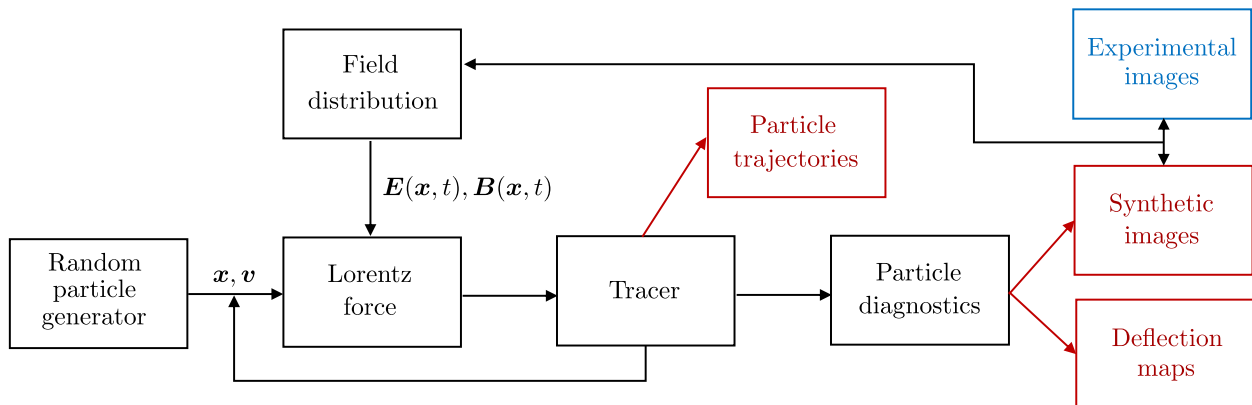


FIG. 13. Workflow for a typical particle-tracing algorithm. Courtesy of L. Romagnani.

protons created instantaneously with a smooth spatial profile, it is a simple matter to include a finite source size or emission time, use a predefined spectrum of proton energies, or incorporate realistic random departures from laminarity. It is also not too challenging to include some additional physics beyond the simple action of Lorentz forces. For example, in dense plasmas scattering or energy loss of beam protons due to Coulomb collisions must be modeled in order to obtain realistic synthetic proton images; see Sec. II.C.3. When this is done, successful measurements of electromagnetic fields in dense plasma can be made: Romagnani *et al.* (2019) used qTrace particle-tracing simulations that included a scattering model to successfully diagnose the time evolution of fast-electron-induced current filaments in dielectric foams, while Lu *et al.* (2020) showed that, provided that scattering was included in supporting particle-tracing simulations, magnetic fields generated by the Biermann battery at a shocked shear layer in a dense foam could be observed. Particle-tracing simulations of proton beams that have been performed using full particle-in-cell (PIC) codes (Huntington *et al.*, 2015) are capable of including another physics effect (albeit one that is usually not important): the beam’s feedback on the electromagnetic fields being imaged via collisionless interaction mechanisms.

3. Combined modeling with HEDP codes

Because of the complexity of the physics inherent in most laser-plasma experiments, as well as the difficulties involved in diagnosing such experiments, HEDP simulation codes are typically used to help design, implement, and interpret their results. Depending on the experiment, the state-of-the-art codes that are run at the present time are magnetized fluid codes [for instance, FLASH, LASNEX (Zimmerman *et al.*, 1977), GORGON (Chittenden *et al.*, 2004), RAGE (Gittings *et al.*, 2008), and HYDRA (Langer, Karlin, and Marinak, 2015)], particle-in-cell codes [for instance, OSIRIS (Fonseca *et al.*, 2002), EPOCH (Arber *et al.*, 2015), PSC (Germaschewski *et al.*, 2016), SMILEI (Derouillat *et al.*, 2018), and VPIC (Bird *et al.*, 2022)], or hybrid codes [for instance, ZEPHYROS (Kar *et al.*, 2009; Ramakrishna *et al.*, 2010), CHICAGO (Thoma *et al.*, 2017), and dHybrid (Gargaté *et al.*, 2007)], all of which output electromagnetic fields. Thus, choosing to use the outputs from such codes as inputs for electromagnetic-field candidates in particle-tracing simulations of proton images is a natural approach. For the outputs of such particle-tracing simulations to provide a plausible comparison with experimental data, the HEDP simulation should be either three dimensional or two dimensional with symmetry, with good spatial (temporal) resolution over sufficiently large spatial (temporal) scales. Aside from the ease of implementation if HEDP simulations have already been completed, this approach can be particularly advantageous if complex electromagnetic-field geometries arise (see Fig. 20 in Sec. IV.C for an example); constructing parametrized electromagnetic-field models from scratch in such situations is laborious. That being said, relying solely on synthetic images derived from HEDP simulations can become problematic if those images turn out to be qualitatively and/or quantitatively distinct from the experimental data they are meant to model. If this situation

arises, it is often challenging to determine how to “correct” the outputs from HEDP simulations systematically.

4. Parametrized field models

Provided that the morphology of experimentally observed proton-fluence inhomogeneities is not too complex, it is often the case that a simple parametrized analytical model for a candidate electromagnetic-field, motivated by considerations of the physical mechanism(s) responsible for generating that field, can be constructed. The optimal choice of the parameters can then be found iteratively using particle-tracing simulations: given a first guess of parameters, a synthetic image is generated and then compared with the experimental image, with the quantitative differences between the outputs then used to determine a revised set of parameters, etc. (Romagnani *et al.*, 2005, 2008a; Cecchetti *et al.*, 2009). We note that in practice previous instances of particle-tracing simulations that have involved updating a parametrized electromagnetic-field model via a direct comparison between synthetic images and actual data do not explicitly report the rate of convergence to the best-fit parameters. This approach can prove helpful if 3D HEDP simulations of a given experiment have not been performed or are producing outputs that are discrepant with experimental data. By construction the technique will recover a good fit to the experimental data for simple proton-fluence inhomogeneities; however, for inhomogeneities lacking symmetry, successfully devising an appropriate analytical model with only a few parameters becomes difficult. Examples of this approach being applied to proton-imaging data are presented in Figs. 16 and 22 in Sec. IV.

C. Analytical modeling

1. Overview

The second methodology for interpreting proton images that has been utilized historically is analytical modeling: that is, relating the line-integrated values of electromagnetic fields to inhomogeneous distributions of the detected proton fluence analytically under a set of simplifying assumptions (Romagnani *et al.*, 2005; Kugland, Ryutov *et al.*, 2012). While analytical relations of this type can be used to test particular candidate electromagnetic-field models (analytical forward modeling), they have proven to be particularly helpful in two key regards. First, they provide a direct interpretation of proton-fluence inhomogeneities in terms of either physical properties of the plasma (specifically, path-integrated charge and current structures) or features inherent in point-projection imaging (specifically, caustics); for discussions of both cases, see Sec. III.C.3. Second, analytical theory has been used to show the conditions under which the determination of line-integrated electromagnetic-field structures from proton-fluence inhomogeneities (which we refer to as field reconstruction) is a mathematically well-posed inversion problem, and if those conditions are met, how such field-reconstruction can be carried out systematically.

An analytical theory of proton imaging is not really tractable unless simplifying assumptions about the imaging setup are made; these assumptions are outlined in Sec. III.C.2, as is the theory that follows directly from them. Once the

analytical theory has been established, we then explain in Sec. III.C.3 how that theory can be used for the direct interpretation of proton-fluence inhomogeneities. Finally, the possibility and implementation of field-reconstruction analysis is discussed in Sec. III.C.4.

2. Analytical theory of proton imaging

In addition to the usually justified assumption that imaging protons behave as test particles, most analytical theories of proton imaging make seven key assumptions:

- *Small-angle deflections:* $\delta\alpha \ll 1$. As discussed in Sec. III.A, this assumption generally allows for the trajectories of beam protons to be treated as linear, and thus for deflection angles to be linearly related to line-integrated electromagnetic fields [viz., Eq. (9)]. Using Eq. (10), it can be shown that this condition is equivalent to assuming that the transverse path-integrated electric and/or magnetic field is much smaller than some critical value; specifically, $|\int_0^{l_{\text{path}}} ds \mathbf{E}_{\perp}| \ll m_p v_0^2/e$ or $|\int_0^{l_{\text{path}}} ds \mathbf{B}_{\perp}| \ll m_p c v_0/e$. Relative to 3.3 MeV protons (one of the two main types of fusion protons produced by D³He capsules), these bounds are

$$\left| \int_0^{l_{\text{path}}} ds \mathbf{E}_{\perp} \right| \ll 6.6 \left[\frac{W_0(\text{MeV})}{3.3 \text{ MeV}} \right] \text{ MV}, \quad (11)$$

$$\left| \int_0^{l_{\text{path}}} ds \mathbf{B}_{\perp} \right| \ll 0.26 \left[\frac{W_0(\text{MeV})}{3.3 \text{ MeV}} \right]^{1/2} \text{ MG cm}, \quad (12)$$

where W_0 is the initial energy of the imaging protons. This implies that electric fields with strengths of \sim MV/cm or magnetic fields of megagauss strengths permeating the full extent of a millimeter-scale plasma (a typical size for plasmas created during HED experiments) are required for the small-angle deflection assumption to become invalid. Though such large electric and magnetic fields are routinely realized, for example, during the interaction of medium-energy, high-intensity lasers with solid targets, generating them across such a volume has been realized only on the very-highest-energy laser facilities, such as the NIF (Meincke *et al.*, 2022).

- *Point projection:* $l_{\text{path}} \ll r_d$. The importance of this assumption was also outlined in Sec. III.A: it allows for proton displacements observed at the detector to be treated as being due to velocity perturbations (as opposed to spatial perturbations) acquired through interaction with the electromagnetic fields of the plasma.
- *Small source size:* $a \ll \ell_{\text{EM}}$, where ℓ_{EM} is the characteristic length scale of the electromagnetic field in the direction transverse to the trajectory of the proton beam. This assumption allows the proton-beam source to be treated as a point source.
- *Monoenergetic beam:* $\Delta v_0 \ll v_0$, where Δv_0 is the characteristic spread of proton speeds in the detected imaging beam. This assumption means that the deflection angles of any constituent protons of the imaging

beam that pass along the same trajectory can be treated the same.

- *Instantaneous transit and short pulse:* $\delta t_p \ll \tau_{\text{EM}}$ and $\delta t_p \sim l_{\text{path}}/v_0 \ll \tau_{\text{EM}}$, where δt_p is the characteristic duration of the proton beam, τ_{EM} is the characteristic timescale over which the electromagnetic field evolves in the plasma, and δt_t is the transit time of the protons through the plasma. If both the transit time and pulse duration of the proton beam are short compared to τ_{EM} , then the electromagnetic field can be treated as electrostatic and/or magnetostatic.
- *Paraxial approximation:* $\ell_{\text{EM}} \ll 2r_s$. This approximation allows for the proton beam to be treated as an expanding planar “sheet” as it passes through the plasma.

We note that particle-tracing simulations do not necessarily have to make any of these assumptions when artificial proton images are generated; however, if these assumptions are not valid, a correct interpretation of proton images is much more challenging. More detailed discussions of these assumptions can be found elsewhere (Kugland, Ryutov *et al.*, 2012; Bott *et al.*, 2017).

Under these seven approximations, the effect of the electromagnetic fields on the proton beam can be modeled as a “remapping” of the beam’s two-dimensional transverse profile prior to it reaching the detector: any proton with an initial perpendicular position $\mathbf{x}_{\perp 0} \equiv \tilde{\mathbf{x}}_{\perp}(0)$ that in the absence of any electromagnetic fields would arrive at the detector plane at the position $\mathbf{d}_{\perp 0} = \mathcal{M}\mathbf{x}_{\perp 0}$ [where $\mathcal{M} = (r_d + r_s + l_{\text{path}})/r_s \approx (r_s + r_d)/r_s$ is the magnification; see Sec. I.A] instead arrives at the remapped position

$$\mathbf{d}_{\perp}(\mathbf{x}_{\perp 0}) = \mathcal{M}\mathbf{x}_{\perp 0} + \Delta\mathbf{d}_{\perp}(\mathbf{x}_{\perp 0}), \quad (13)$$

where

$$\Delta\mathbf{d}_{\perp}(\mathbf{x}_{\perp 0}) = \frac{er_d}{m_p v_0^2} \int_0^{l_{\text{path}}} dz \left\{ \mathbf{E}_{\perp} \left[\mathbf{x}_{\perp 0} \left(1 + \frac{z}{r_s} \right) + z\hat{\mathbf{z}} \right] + \frac{\tilde{\mathbf{v}}}{c} \times \mathbf{B}_{\perp} \left[\mathbf{x}_{\perp 0} \left(1 + \frac{z}{r_s} \right) + z\hat{\mathbf{z}} \right] \right\}. \quad (14)$$

In Eq. (14) $\hat{\mathbf{z}}$ is the unit vector normal to the plane of the detector and z is the coordinate along that axis. Conservation of proton number within any infinitesimal surface element of the beam’s transverse profile then implies that the distribution $\Psi(\mathbf{d}_{\perp})$ of protons measured by the detector at position \mathbf{d}_{\perp} is related to the initial distribution $\tilde{\Psi}_0(\mathbf{x}_{\perp 0})$ via

$$\Psi[\mathbf{d}_{\perp}(\mathbf{x}_{\perp 0})] = \sum_{\mathbf{x}_{\perp 0}: \mathbf{d}_{\perp}=\mathbf{d}_{\perp}(\mathbf{x}_{\perp 0})} \frac{\tilde{\Psi}_0(\mathbf{x}_{\perp 0})}{|\det \nabla_{\perp 0}[\mathbf{d}_{\perp}(\mathbf{x}_{\perp 0})]|}. \quad (15)$$

Equation (15), which is the key analytical relationship between inhomogeneities in the detected proton-fluence and path-integrated electromagnetic fields, is interpreted as follows. The fluence $\Psi(\mathbf{d}_{\perp})$ of protons measured at position \mathbf{d}_{\perp} on the detector is equal to the sum of initial proton fluences $\tilde{\Psi}_0(\mathbf{x}_{\perp 0})$ of all of the perpendicular positions $\mathbf{x}_{\perp 0}$ that, after electromagnetic-field-induced deflections, are remapped to \mathbf{d}_{\perp} and divided by a modification factor. This modification factor

characterizes the degree to which the proton beam has been locally focused or defocused at a particular position $\mathbf{x}_{\perp 0}$ due to the beam's deflection. Formally, it is the absolute value of the Jacobian determinant of the mapping defined by Eq. (13). The summation is included because in general it is possible that protons from multiple different initial positions $\mathbf{x}_{\perp 0}$ can in principle contribute to the proton-fluence distribution at the same position \mathbf{d}_{\perp} on the detector if the deflections of those protons cause the beam to self-intersect before they arrive at the detector. In this situation, the mapping (13) is, in the mathematical sense, noninjective (that is, there is not a unique position $\mathbf{x}_{\perp 0}$ that maps to \mathbf{d}_{\perp}). If, by contrast, Eq. (13) is injective, then the summation is unnecessary. For both TNSA and $D^3\text{He}$ proton sources, the initial fluence distribution $\tilde{\Psi}_0(\mathbf{x}_{\perp 0})$ is to a good approximation uniform over small solid angles; see Sec. II. $\tilde{\Psi}_0(\mathbf{x}_{\perp 0})$ is therefore often assumed to be uniform: $\tilde{\Psi}_0(\mathbf{x}_{\perp 0}) \approx \mathcal{M}^2 \Psi_0$, where Ψ_0 is the mean detected proton fluence.

Naively, the mapping (13) seems to depend on four path-integrated components of the electromagnetic field being imaged via the displacement term (14). However, Eq. (14) has a convenient mathematical property: it can be expressed as the gradient of a two-dimensional scalar potential that is a linear combination of path-integrated electromagnetic potentials. More specifically, it can be shown that (Kugland, Ryutov *et al.*, 2012; Bott *et al.*, 2017)

$$\Delta \mathbf{d}_{\perp}(\mathbf{x}_{\perp 0}) \approx -\frac{er_d}{m_p v_0^2} (\nabla_{\perp 0} \int_0^{l_{\text{path}}} dz \left\{ \phi \left[\mathbf{x}_{\perp 0} \left(1 + \frac{z}{r_s} \right) + z\hat{\mathbf{z}} \right] - \frac{v_0}{c} A_{\parallel} \left[\mathbf{x}_{\perp 0} \left(1 + \frac{z}{r_s} \right) + z\hat{\mathbf{z}} \right] \right\}), \quad (16)$$

where ϕ is the electromagnetic scalar potential, \mathbf{A} is the electromagnetic vector potential, and A_{\parallel} is the component parallel to $\hat{\mathbf{v}}$. We deduce that Eq. (13) can be written as

$$\mathbf{d}_{\perp}(\mathbf{x}_{\perp 0}) \approx \nabla_{\perp 0} \psi(\mathbf{x}_{\perp 0}), \quad (17)$$

where

$$\psi(\mathbf{x}_{\perp 0}) \equiv \frac{1}{2} \mathcal{M} x_{\perp 0}^2 + \varphi(\mathbf{x}_{\perp 0}), \quad (18)$$

$$\varphi(\mathbf{x}_{\perp 0}) \equiv \frac{er_d}{m_p v_0^2} \int_0^{l_{\text{path}}} dz \left\{ -\phi \left[\mathbf{x}_{\perp 0} \left(1 + \frac{z}{r_s} \right) + z\hat{\mathbf{z}} \right] + \frac{v_0}{c} A_{\parallel} \left[\mathbf{x}_{\perp 0} \left(1 + \frac{z}{r_s} \right) + z\hat{\mathbf{z}} \right] \right\}. \quad (19)$$

Thus, provided that the assumptions underpinning standard analytical theories of proton imaging are valid, detected proton-fluence inhomogeneities are a function of only two path-integrated scalar functions pertaining to the electromagnetic field: a property of vital importance for successfully realizing field reconstruction; see Sec. III.C.4.

3. Analytical interpretations of proton-fluence inhomogeneities

Using Eq. (15), the relation between path-integrated electromagnetic fields and the distribution of proton fluence

[a relation that is in turn a function of the two-dimensional mapping (13)], it becomes possible to construct a framework that systematically characterizes all classes of proton-fluence inhomogeneities that can arise in images of arbitrary electromagnetic fields into a few different regimes. As explained in Sec. I.A, the key dimensionless parameter that underpins this framework is the contrast parameter μ , which is given by (Kugland, Ryutov *et al.*, 2012; Bott *et al.*, 2017)

$$\mu = \frac{r_d \delta \alpha}{\mathcal{M} \ell_{\text{EM}}^{(d)}}. \quad (20)$$

Physically, this parameter quantifies the relative magnitude $\ell_{\text{EM}}^{(d)} \equiv \mathcal{M} \ell_{\text{EM}}$ of the electromagnetic structures being imaged (including magnification) and the displacements $\Delta d_{\perp} \equiv r_d \delta \alpha$ of protons at the detector acquired due to their interaction with those electromagnetic structures [mathematically, μ quantifies the relative magnitude of the two terms in the mapping (13) when their gradient is taken in the denominator of the fraction present on the right-hand side of Eq. (15)]. Depending on the size of μ , the three regimes of a qualitatively distinct nature for electromagnetic fields with a single characteristic scale are as follows²:

- (1) *Linear regime* ($\mu \ll 1$). In this regime, $\Delta d_{\perp} \ll \ell_{\text{EM}}^{(d)}$, so the characteristic scale of proton-fluence inhomogeneities is similar to that of the electromagnetic fields being imaged. As a result, the relationship between proton-fluence inhomogeneities and path-integrated electromagnetic fields becomes to a good approximation linear (hence the regime's name), with the characteristic size $\delta \Psi$ of those inhomogeneities being small compared to the mean proton fluence Ψ_0 : $\delta \Psi / \Psi_0 \sim \mu \ll 1$. Indeed, in the linear regime proton-fluence inhomogeneities have a simple physical interpretation in terms of path-integrated charge and current densities. For purely electrostatic fields $\delta \Psi / \Psi_0 \propto -\int_0^{l_{\text{path}}} ds \rho$, where ρ is the charge density in the plasma (Romagnani *et al.*, 2005), while for purely magnetic fields $\delta \Psi / \Psi_0 \propto -\int_0^{l_{\text{path}}} ds j_{\parallel}$, where j is the magnetohydrodynamic (MHD) current density (Graziani *et al.*, 2017).
- (2) *Nonlinear injective regime* ($\mu \lesssim \mu_c \sim 1$). In this regime $\Delta d_{\perp} \lesssim \ell_{\text{EM}}^{(d)}$, but with the additional constraint that μ is not larger than some critical value μ_c at which the proton beam self-intersects prior to reaching the detector on account of spatially inhomogeneous deflections; viz., the mapping (13) remains injective, so the summation in Eq. (15) is not needed. As a result of the comparatively large magnitude of Δd_{\perp} compared to $\ell_{\text{EM}}^{(d)}$, the characteristic scales of proton-fluence inhomogeneities are distorted away from those of the path-integrated electromagnetic fields (inhomogeneities with $\delta \Psi > \Psi_0$ are focused, while those with $\delta \Psi < \Psi_0$ are defocused) and the magnitude of proton-

²The characterization of multiscale electromagnetic fields, or fields with sharp gradients, is more subtle; see Kugland, Ryutov *et al.* (2012) and Bott *et al.* (2017).

fluence inhomogeneities in this regime is typically comparable to the mean proton fluence ($\delta\Psi \sim \Psi_0$). The simple physical interpretation of proton-fluence inhomogeneities in terms of path-integrated charge and current structures is no longer quantitative in the nonlinear injective regime, but such relationships still hold qualitatively. We note that the value of μ_c depends on the particular electromagnetic-field structure being imaged but is typically of the order of unity.

- (3) *Caustic regime* ($\mu \geq \mu_c$). In this regime $\Delta d_{\perp} \gtrsim \ell_{\text{EM}}^{(d)}$, with spatial gradients being sufficiently large that the proton beam self-intersects prior to being detected. As explained in Sec. I.A, this self-intersection leads to the emergence of proton-fluence inhomogeneities known as caustics. Caustics have a specific structure that is unrelated to the electromagnetic fields responsible for them: they attain large magnitudes ($\delta\Psi \gg \Psi_0$) in isolated regions and typically occur in pairs; see [Kugland, Ryutov *et al.* \(2012\)](#) for a detailed discussion of caustics. It follows that the interpretation of proton-fluence inhomogeneities in terms of path-integrated electromagnetic fields is more challenging in the presence of caustics than in their absence, though some successful measurements of simple field structures in this circumstance have been made ([Kugland *et al.*, 2012, 2013](#); [Morita *et al.*, 2016](#); [Levesque and Beesley, 2021](#)).

Because μ is directly proportional to the deflection angle $\delta\alpha$, it is linear in the characteristic strength of the electromagnetic field being imaged. By contrast, μ is inversely related to the initial proton energy: for magnetic fields $\mu \propto W_0^{-1/2}$, while for electric fields $\mu \propto W_0^{-1}$. Thus, a given electromagnetic-field structure can be in any one of the contrast regimes, depending on its strength and the energy of protons being used to perform imaging. Varying the dimensional parameters that describe the imaging diagnostic setup (for instance, r_s and r_d) also affects the contrast regime.

We illustrate the key features of the three contrast regimes with a simple numerical example. In this case, we compare the three regimes by choosing one field structure and then generating a sequence of synthetic proton images at increasing characteristic field strengths. We choose an ‘‘ellipsoidal blob’’ magnetic field ([Kugland, Ryutov *et al.*, 2012](#)) given by

$$\mathbf{B} = \frac{B_{\text{max}}}{\sqrt{2}} \frac{\mathbf{x}_{\perp 0} \times \hat{z}}{\ell_{\text{M}\perp}} \exp \left[-\frac{|\mathbf{x}_{\perp 0}|^2}{\ell_{\text{M}\perp}^2} - \frac{(z - z_c)^2}{\ell_{\text{M}\parallel}^2} - \frac{1}{2} \right], \quad (21)$$

where B_{max} is the maximum strength of the field, $\ell_{\text{M}\perp}$ is its perpendicular scale length, $\ell_{\text{M}\parallel}$ is its parallel scale, and z_c is the z coordinate of the field’s central point. The field is visualized in Fig. 14(a).

The spatial distribution of the z component of the MHD current density, which is given by

$$j_z = \frac{cB_{\text{max}}}{8\sqrt{2}\pi\ell_{\text{M}\perp}} \left(1 - \frac{|\mathbf{x}_{\perp 0}|^2}{\ell_{\text{M}\perp}^2} \right) \times \exp \left[-\frac{|\mathbf{x}_{\perp 0}|^2}{\ell_{\text{M}\perp}^2} - \frac{(z - z_c)^2}{\ell_{\text{M}\parallel}^2} - \frac{1}{2} \right], \quad (22)$$

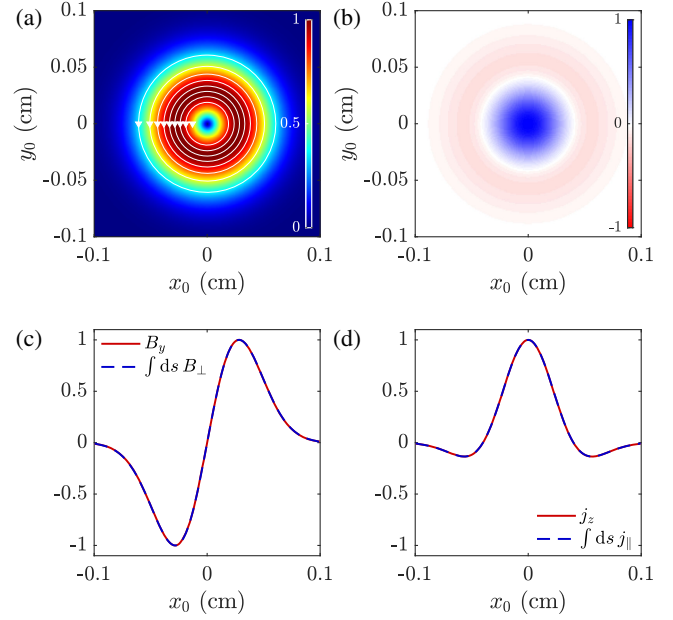


FIG. 14. An ellipsoidal blob magnetic field used to illustrate contrast regimes. (x_0, y_0) -slice plots of (a) magnetic-field strength $B = |\mathbf{B}|$ and (b) MHD current density j_z in the center of the ellipsoidal blob (at $z = z_0$), normalized by the maximum field strength B_{max} and maximum current density, respectively. The magnetic-field lines and the field’s orientation are shown in white in (a), where $\ell_{\text{M}\parallel} = \ell_{\text{M}\perp} = 0.04$ cm. (c), (d) Normalized lineouts of B_y and j_z in x_0 (at $y_0 = 0$) with the values of B_{\perp} and j_{\parallel} line integrated along the trajectories of protons that originate from a source at $(x, y, z) = (0, 0, -r_s)$ and pass through positions $(x, y, z) = (x_0, y_0, 0)$.

is visualized in Fig. 14(b). Note that for this choice both the path-integrated magnetic field and the MHD current density have approximately the same perpendicular spatial structure as the three-dimensional field itself; see Figs. 14(c) and 14(d). Corresponding proton images of this magnetic field in the linear, nonlinear injective, and caustic regimes are shown in Fig. 15.

In the linear regime, Figs. 15(a) and 15(b) demonstrate that the proton-fluence inhomogeneity $\delta\Psi$ is indeed small in magnitude compared to the mean fluence Ψ_0 , with that inhomogeneity being approximately proportional to the MHD current. In the nonlinear injective regime, the central part of the ellipsoidal blob (which has $j_z > 0$) is larger in the proton image than in actuality [Fig. 15(c)], and the fluence and MHD current profile no longer agree quantitatively [Fig. 15(d)]. Finally, in the caustic regime [see Figs. 15(e) and 15(f)] two high-amplitude caustic structures demarcate the edge of the ellipsoidal blob, whose structure does not resemble the true value of j_z .

4. Inverse analysis using electromagnetic-field-reconstruction algorithms

In addition to providing a framework for the general interpretation of proton-fluence inhomogeneities in terms of the path-integrated fields creating them, further consideration of Eq. (15) reveals the conditions under which direct inversion

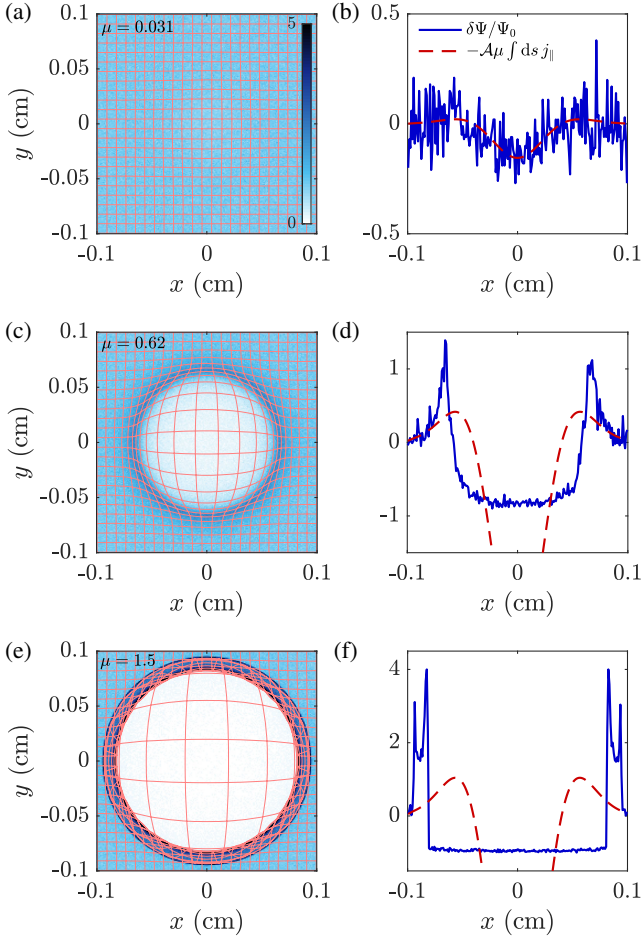


FIG. 15. Comparison of contrast-parameter (μ) regimes for proton images of the ellipsoidal blob magnetic field described in Fig. 14. Images in the (a) linear, (c) nonlinear injective, and (e) caustic regimes are shown, as are proton-fluence lineouts along x (at $y = 0$) in (b), (d), and (f), respectively. Superimposed onto the images is the mapping $\mathbf{d}_\perp = \mathbf{d}_\perp(\mathbf{x}_{\perp 0})$ for each case (the solid lines). To generate the images, protons were simulated with $v_0 = 5.31 \times 10^9$ cm/s (corresponding to 14.7 MeV protons), a setup with $r_s = 1$ and 30 cm, and a field $B_{\max} = 10, 200,$ and 500 kG for the linear, nonlinear injective, and caustic regime images, respectively. The resolution of the images is 200×200 pixels, with a mean proton density per pixel of 100. Following previous conventions for the ellipsoidal blob (Kugland, Ryutov *et al.*, 2012), one can define μ as $\mu = \sqrt{\pi} e r_s B_{\max} \ell_{M\parallel} / m_p c v_0 \mathcal{M} \ell_{M\perp}$, where \mathcal{A} is an order-unity constant of proportionality.

of path-integrated electromagnetic fields from proton images is possible: that is, determining $\Delta \mathbf{d}_\perp(\mathbf{x}_{\perp 0})$ directly from $\Psi(\mathbf{d}_\perp)$. The key result of previous studies (Bott *et al.*, 2017; Graziani *et al.*, 2017) is that a direct inversion of Eq. (15) from a single image is a well-posed mathematical problem provided that the mapping (13) is injective or, equivalently, that there are no caustics present in the images. In terms of contrast regimes, inversion can be performed in either the linear or the nonlinear injective regime. This finding follows from the observation that Eq. (15) can be written as a Monge-Ampère equation if the mapping (13) is injective,

$$\Psi[\nabla_{\perp 0} \psi(\mathbf{x}_{\perp 0})] = \frac{\tilde{\Psi}_0(\mathbf{x}_{\perp 0})}{\det \nabla_{\perp 0} \nabla_{\perp 0} \psi(\mathbf{x}_{\perp 0})}, \quad (23)$$

where $\psi(\mathbf{x}_{\perp 0})$ is the scalar function defined by Eq. (18) in Sec. III.C.2. In spite of their nonlinearity, Monge-Ampère equations have unique solutions for $\nabla_{\perp 0} \psi(\mathbf{x}_{\perp 0})$ [and thus $\mathbf{d}_\perp(\mathbf{x}_{\perp 0}) \approx \nabla_{\perp 0} \psi(\mathbf{x}_{\perp 0})$] given appropriate Neumann boundary conditions. In the case of general electromagnetic fields, more information is needed to distinguish between path-integrated electrostatic and magnetic fields, but in the case where one dominates over the other, the path-integrated electrostatic or magnetic field in a plasma can be reconstructed.

Various different “field-reconstruction” algorithms for recovering path-integrated electromagnetic fields directly from proton-fluence inhomogeneities have been proposed. In the linear regime, it can be shown that the inversion problem is simply equivalent to solving a Poisson equation for the scalar function $\varphi(\mathbf{x}_{\perp 0})$ (Romagnani *et al.*, 2005; Kugland, Ryutov *et al.*, 2012): $\nabla_{\perp 0}^2 \varphi(\mathbf{x}_{\perp 0}) = -\mathcal{M} \delta \Psi / \Psi_0$. However, a later study by Graziani *et al.* (2017) found that inversion quickly fails for anything but small values of μ ; they proposed overcoming this by including first-order terms in the $\mu \ll 1$ expansion, solving the resulting equations with the PRALINE code (Graziani *et al.*, 2017). In the $\mu \lesssim 1$ regime, descriptions of three different algorithms have been published: a Voronoi-diagram method to reconstruct path-integrated magnetic fields by Kasim *et al.* (2017); the PROBLEM code by Bott *et al.* (2017), which uses a nonlinear diffusion method proposed by Sulman, Williams, and Russell (2011) to solve the same problem; and finally a trained neural network by Chen *et al.* (2017) (who also trained their network to resolve the 3D structure of ellipsoid blobs, though it is unlikely this approach is applicable to more general electromagnetic fields). Other algorithms have been used to reconstruct electromagnetic fields, in particular, experiments (Schaeffer *et al.*, 2019; Campbell *et al.*, 2020; Levesque *et al.*, 2022), though full details of these codes have not yet been published. Comparisons of the outputs of these codes are currently an active research effort (Davies and Heuer, 2022).

By contrast, the possibility of performing direct inversion analysis from a single proton image if caustics are present has been shown not to be a well-posed mathematical problem: multiple path-integrated electromagnetic-field “solutions” exist for a single proton-fluence distribution Ψ . In this situation, it can be proven that the solution to the Monge-Ampère equation [Eq. (23)] minimizes the functional

$$\mathcal{C}\{\Delta \mathbf{d}_\perp\} = \int d^2 \mathbf{x}_{\perp 0} |\Delta \mathbf{d}_\perp(\mathbf{x}_{\perp 0})|^2 \tilde{\Psi}_0(\mathbf{x}_{\perp 0}). \quad (24)$$

In the case of a uniform initial proton-fluence distribution, the Monge-Ampère solution therefore minimizes the root mean square of proton displacements over the space of all possible solutions. In practice, if $|\mu - \mu_c| \ll 1$, the “family” of possible solutions associated with a particular distribution Ψ is typically constrained to be similar to the Monge-Ampère solution. Thus, outputs of reconstruction algorithms are usually close to the “true” result for a point source of protons (Kasim *et al.*, 2017), though this rule of thumb becomes much

less robust if realistic proton source sizes are taken into account (Bott *et al.*, 2017). If $|\mu - \mu_c| \gtrsim 1$, then previous studies (Bott *et al.*, 2017) have shown that the Monge-Ampère solution can return significant underestimates of characteristic path-integrated electromagnetic-field strengths compared to those of the true electromagnetic field. Systematically extracting information about path-integrated electromagnetic fields from proton images that contain caustics is therefore an outstanding research problem in proton-image analysis (although some recent progress has been made on this; see Sec. V.D).

Although field-reconstruction algorithms have been successfully applied to real experimental data (Tzeferacos *et al.*, 2018; Schaeffer *et al.*, 2019; Campbell *et al.*, 2020; Bott *et al.*, 2021a, 2021b; Levesque *et al.*, 2022), these efforts have shown that several technical issues can arise in the process of performing such analysis. First of these is the finding that field-reconstruction algorithms are sensitive to any large-scale variations in the initial proton-fluence profile $\tilde{\Psi}_0(\mathbf{x}_{\perp 0})$. For example, it has been shown that two qualitatively different path-integrated magnetic fields can give the same proton image with only subtly different initial profiles (Bott *et al.*, 2017). While both TNSA and D³He proton sources can produce beams whose transverse spatial inhomogeneities are small compared to the mean fluence on submillimeter plasma scales (Manuel, Zylstra *et al.*, 2012), it has proven challenging to avoid significant inhomogeneities on larger scales. Studies aimed at overcoming this problem are ongoing, but possible remedies include high-pass filtering of either images or reconstructed path-integrated fields in order to isolate only those outputs for which uncertainties are not too large (Bott *et al.*, 2017; Kasim *et al.*, 2017), applying constrained polynomial or Gaussian (as opposed to uniform) models for the initial profile (Palmer *et al.*, 2019; Fox *et al.*, 2020), and using Bayesian inference conditioned on the well-characterized properties of the initial proton-beam inhomogeneities (Kasim *et al.*, 2019). Another issue that is particularly important for fusion-capsule proton sources is the effect of a finite source size. It has been demonstrated (Bott *et al.*, 2017) that the source's finite size reduces the characteristic value of μ_c below which field-reconstruction algorithms return accurate results compared with the case of a genuine point source. Bott *et al.* (2017) proposed the Lucy-Richardson deconvolution algorithm as a way to mitigate this issue, but further study of more robust techniques is warranted. Finally, field-reconstruction algorithms neglect the “blurring” effect of scattering of beam protons due to Coulomb collisions on proton images. However, this blurring is usually significant in experiments involving dense plasmas and thus should not be ignored in future studies; see Sec. V.C.

D. Comparing particle-tracing and analytical modeling techniques

In Secs. III.B and III.C, we reviewed the use of particle-tracing simulations and analytical theory, respectively, for analyzing proton images; providing a comparative discussion

of the two methodologies with respect to each other is therefore apt. The main advantage that particle-tracing simulations have over analytical modeling is the possibility of avoiding the approximations that analytical modeling has to make in order to be tractable. These approximations involve the physics underpinning the interaction of the beam with the plasma (for instance, scattering), the precise properties of the proton beam's source, and the geometry of the imaging setup; see Sec. III.C.2. Avoiding some of these approximations is vital for certain categories of laser-plasma experiments, such as those investigating ultrafast laser-plasma dynamics; see Sec. IV.G. However, it is challenging for particle-tracing simulations to overcome one of the central challenges for all forward-modeling techniques (the possibility of multiple qualitatively distinct solutions that are all consistent with the input data) without recourse to analytically derived results (such as uniqueness). In addition, field-reconstruction algorithms based on analytical modeling allow for images of complicated electromagnetic-field structures to be analyzed in situations when HEDP simulations either are unavailable or are not able to reproduce the relevant physics correctly. All said, we emphasize that either technique can be highly effective, but also that the most robust analysis usually involves both.

IV. PROTON-IMAGING EXPERIMENTS

To demonstrate the variety of phenomena that can be investigated using proton imaging, we provide here a survey of the different types of experiments that have been performed using the diagnostic. Examples include applications with spontaneously generated magnetic fields (Sec. IV.A), magnetic reconnection (Sec. IV.B), Weibel instabilities (Sec. IV.C), shocks (Sec. IV.D), jets (Sec. IV.E), turbulence and dynamos (Sec. IV.F), ultrafast dynamics (Sec. IV.G), hydrodynamic instabilities (Sec. IV.H), and ICF (Sec. IV.I).

A. Magnetic-Field Generation

Magnetic fields can be spontaneously generated by several different mechanisms in initially unmagnetized plasmas, and proton imaging has been used to explore and characterize these processes in various laser-plasma experiments. Understanding these possible sources of magnetic fields is an important research area in HED plasma physics because basic processes such as heat transport can be profoundly altered if magnetic fields become strong enough to magnetize the plasma's constituent particles (that is, reduce their Larmor radii below their respective Coulomb mean free paths). A detailed discussion of the many sources of magnetic fields in hot laser-produced plasma was given by Haines (1986); here we focus on the most notable ones and their investigation using proton imaging.

One of the first mechanisms for generating magnetic fields in plasmas to be identified theoretically [and also one of the first to be observed in experiments (Stamper *et al.*, 1971)] is the Biermann battery, whereby magnetic fields are generated by misaligned electron density and pressure gradients (Biermann and Schluter, 1951). Within the framework of

extended MHD, the Biermann battery can be modeled as a source term in the induction equation,

$$\frac{\partial \mathbf{B}}{\partial t} = -\frac{c \nabla n_e \times \nabla p_e}{en_e^2} - c \nabla \times \left(\frac{\beta_{\parallel} \nabla T_e}{e} \right) + \nabla \times (\mathbf{v}_B \times \mathbf{B}) - \nabla \times (\eta \nabla \times \mathbf{B}). \quad (25)$$

In Eq. (25) the first source term on the right-hand side is the Biermann battery (the second source term, which is often neglected in modeling, is associated with ionization). It can be shown that the Biermann battery term generates a field δB in a time interval δt of magnitude $\delta B \sim \delta t c k_B \nabla T_e \times \nabla n_e / en_e$. Once generated, this Biermann field then evolves through advection at a characteristic bulk-flow velocity \mathbf{v}_B [the third term of Eq. (25)] and through diffusion by the resistivity η [the fourth term of Eq. (25)] (Haines, 1986). Since nonparallel plasma temperature and density gradients are common in plasmas, magnetic-field generation by the Biermann battery is ubiquitous in HED experiments and is a frequent subject of proton imaging. For a laser pulse interacting with a solid target, the electron density gradient is primarily in the target normal direction, whereas the electron temperature gradient is primarily radial, meaning that an azimuthal magnetic field is generated around the laser focal spot. The rate of field generation is therefore dependent on processes like the energy transfer from the laser to the plasma, and parameters such as the focal spot size and intensity profile.

With the advent of proton imaging, a number of experiments have studied the generation of magnetic fields near the surface of laser-driven targets by the Biermann battery (Li *et al.*, 2006b; Nilson *et al.*, 2006; Cecchetti *et al.*, 2009; Petrasso *et al.*, 2009; Willingale *et al.*, 2011a, 2013; Gao *et al.*, 2012, 2013, 2015; Lancia *et al.*, 2014; Campbell *et al.*, 2020). The first measurements used grid deflectometry to gauge the deflections of a known periodicity mesh to infer the path-integrated magnetic fields; see Sec. II.C.2. Proton-beam deflections are affected by the direction of the projection of the protons. For a “front”-projection geometry, where protons travel from the interaction side of the main target to the rear, the $\mathbf{v} \times \mathbf{B}$ Lorentz force primarily deflects the proton beam radially inward. A “rear”-projection geometry, where protons first pass through the target before observing the front-side magnetic fields, produces an outward deflection. This was illustrated by Cecchetti *et al.* (2009). Figure 16 presents experimental data using a TNSA source in front-projection [Fig. 16(a)] and rear-projection geometries [Fig. 16(c)]. Figures 16(b) and 16(d) are the particle-tracking calculations for an idealized magnetic torus in front- and rear-projection geometries, respectively. Similar data using a D³He source were presented by Petrasso *et al.* (2009). While the proton images naively make the extent and magnitude of the fields appear to be different for the two geometries, comparisons to analytical field maps show that the strength and scale of the fields are in fact similar.

Biermann-battery-generated fields can be up to a megagauss or more and evolve on nanosecond timescales. These measurements are to within an order of magnitude, but not necessarily in exact agreement with, simulation predictions (Li *et al.*, 2006b). Numerical modeling typically consists of

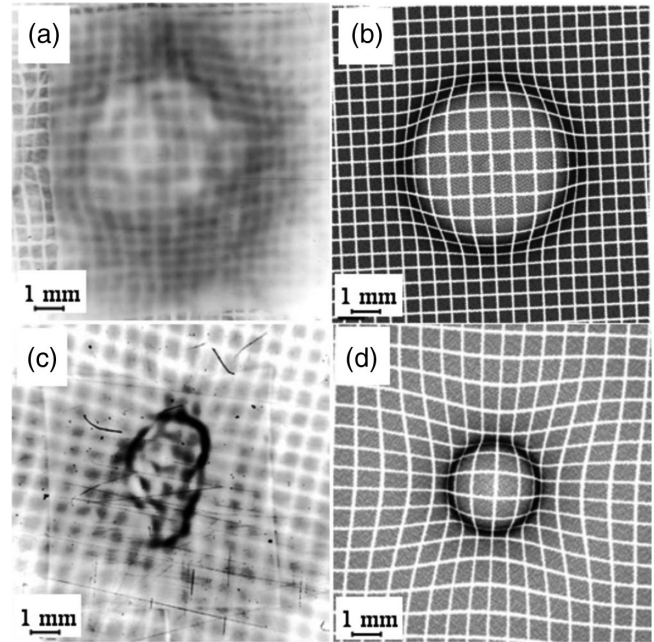


FIG. 16. Experimental images of TNSA proton deflectometry of a laser-generated plasma shown for geometries in which protons pass first through (a) the plasma (front projection) or (c) target (rear projection). Corresponding synthetic proton images were created with the particle-tracing code PTRACE using an idealized magnetic-field torus in (b) front and (d) rear geometries, respectively. Adapted from Cecchetti *et al.*, 2009.

MHD simulations that include a Biermann battery source term, resistive magnetic diffusion, and fluid advection [see Eq. (25)] and often Nernst advection, Righi-Leduc heat flow, and radiation. Measurements have confirmed that, once generated, magnetic fields can indeed be advected by the bulk plasma motion, i.e., at the ion fluid velocity, or the hot electron flux can transport the magnetic field at a faster speed through the Nernst effect (Nishiguchi *et al.*, 1984; Willingale *et al.*, 2010b) and other effects (Lancia *et al.*, 2014; Gao *et al.*, 2015). Proton-imaging experiments by Campbell *et al.* (2020) have shown that varying the target material alters the field generation (see Fig. 17) and even the development of a double ablation front for mid-Z materials. Careful analysis of the field measurements to quantify total magnetic flux show that kinetic effects can suppress Biermann battery field generation in laser-plasma interactions (Campbell *et al.*, 2022).

Wilks *et al.* (1992) proposed that magnetic fields much stronger than those generated by the Biermann battery can be created by relativistic laser interactions ($> 10^{18} \text{ W cm}^{-2}$) due to currents produced by suprathermal electrons accelerated in the evanescent region of the laser wave that propagate deep into the interior of the plasma. This magnetic field is in the azimuthal direction about the laser axis of propagation, and the peak field extends for about an anomalous skin depth into the plasma (i.e., $d = [(c/\omega_{pe})(v_{te}/\omega_0)]^{1/2}$, where v_{te} is the electron thermal velocity). Mason and Tabak (1998) predicted the generation of fields up to 250 MG in the overdense plasma for moderately relativistic interactions. Measurements of these short-pulse, relativistic-intensity-generated magnetic fields have been measured using

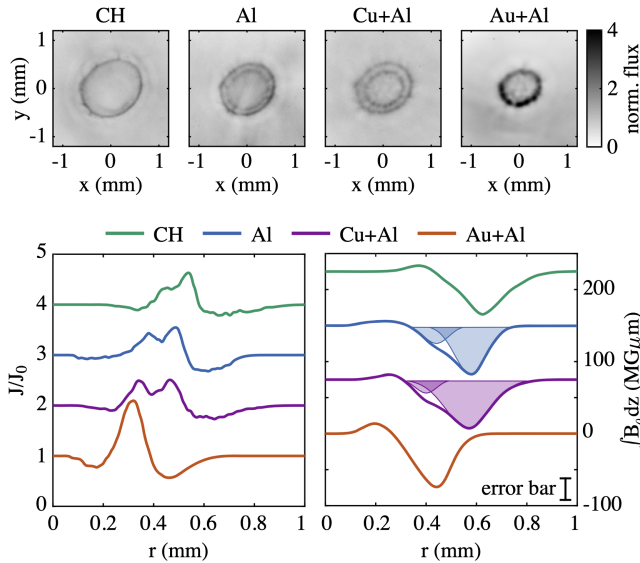


FIG. 17. Top row: proton images of the fields generated from laser ablation of different target materials at a time of 0.75 ns into a 1 ns, 1025 J interaction. The proton energy is 37.3 MeV for CH, Al, and Cu + Al, and 30.7 MeV for Au + Al. Bottom left panel: radial lineouts of the proton fluence (J) normalized by the mean inferred reference profile (J_0). Bottom right panel: the resulting reconstructed field profiles. For Al and Cu + Al, the results of double-Gaussian fitting are shown with shaded regions. Adapted from [Campbell *et al.*, 2020](#).

TNSA protons by [Sarri *et al.* \(2012\)](#). One significant difference compared to the lower-intensity measurements is that large fields are expected to be present on both the front and rear sides of the target. Hot electrons rapidly move through the target to expand into the vacuum at the front and rear, creating time-varying sheath fields that generate opposing magnetic fields on the front and rear target surfaces. This means that on one side of the target the proton beam is deflected radially inward while on the other side it is deflected outward from the interaction region, which significantly complicates the analysis and interpretation of the proton data.

A different method for creating magnetic fields with laser-plasma interactions is through laser-driven coils ([Gao *et al.*, 2016](#); [Peebles *et al.*, 2022](#)). In this approach, a laser is used to heat and eject electrons from a plate so that a current is drawn through a loop connected to the plate. The interaction region within the loop, a volume of the order of 1 mm³, contains a strong axial magnetic field that can be used as an externally applied field for other experiments. [Peebles *et al.* \(2020\)](#) measured axial fields of up to 65 ± 15 T.

B. Magnetic reconnection

Magnetic reconnection ([Yamada, Kulsrud, and Ji, 2010](#)) is a physical process whereby the magnetic-field topology is rearranged, dissipating magnetic energy in a plasma into kinetic energy. It is a prevalent phenomenon throughout the Universe that occurs under many different conditions: for example, within the solar corona, where it leads to solar flares and coronal mass ejections ([Parker, 1957](#)), between the solar

wind and Earth's magnetosphere, and during fusion plasma instabilities ([Taylor, 1986](#)). Breaking and reconnecting magnetic-field lines at observed rates require dissipation mechanisms to function at rates greater than allowed by classical resistivity ([Yamada, Kulsrud, and Ji, 2010](#)). Consequently there are many open questions to be investigated, including the temporal and spatial scales of the reconnection, the role of dynamical processes like plasmoid formation, and the final energy partition of the system. Furthermore, there are a wide range of reconnection regimes to explore due to how the magnetization, collisionality, and symmetry of the system affect the mediation of the reconnection process.

Laser-driven magnetic reconnection is a convenient way to study impulsive, strongly driven reconnection physics in the laboratory. Using proton imaging to diagnose the magnetic fields, the first experimental demonstration using lasers was performed by [Nilson *et al.* \(2006\)](#), with the basic experimental configuration shown in Fig. 18. These experiments used two neighboring high-energy, nanosecond duration laser pulses to produce self-generated azimuthal magnetic fields through the Biermann battery mechanism ([Nilson *et al.*, 2006, 2008](#); [Li *et al.*, 2007](#); [Willingale *et al.*, 2010a](#); [Zhong *et al.*, 2010](#); [Fox, Bhattacharjee, and Germaschewski, 2011, 2012](#); [Dong *et al.*, 2012](#); [Rosenberg *et al.*, 2012](#)); see Sec. IV.A. The magnetic fields were then advected out either by the frozen-in flow or by heat transport via the Nernst effect, leading the opposing magnetic fields to be driven together in the midplane between the two focal spots. A key feature of such experiments is that the so-called plasma β , defined as the ratio of thermal to magnetic pressure, is typically large.

Numerous high-quality proton-imaging measurements have been made of magnetic fields in reconnection laser-plasma experiments of this type. For example, [Li *et al.* \(2007\)](#) and [Willingale *et al.* \(2011b\)](#) observed the rearrangement of the magnetic field's topology using proton imaging (as well as elevated plasma temperatures in the midplane region using Thomson scattering and plasma jets emanating from the reconnection plane using optical probing). Experiments by [Rosenberg, Li, Fox, Zylstra *et al.* \(2015\)](#) used proton imaging

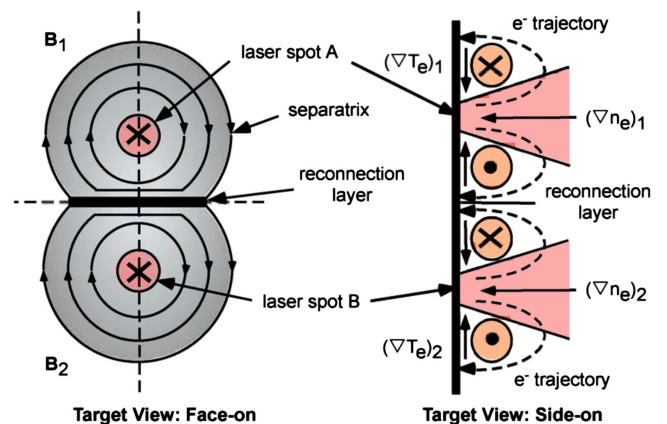


FIG. 18. Schematic of a laser-driven magnetic reconnection geometry. The opposing magnetic fields are driven together in the midplane between the laser focal spots. The fields can be probed at different times to observe the dynamics. Adapted from [Nilson *et al.*, 2006](#).

to observe the slowing of the reconnection rate as the plasma inflows weaken and investigated the effect of asymmetric field structures (Rosenberg, Li, Fox, Igumenshchev *et al.*, 2015). Experimental measurements using proton deflectometry by Tubman *et al.* (2021) showed anomalously fast reconnection in weakly collisional colliding laser plasmas.

These measurements (and also concurrent measurements from other complimentary diagnostics of the plasma conditions) have prompted new theoretical and numerical modeling studies of the high- β reconnection regime, in turn helping advance our understanding of reconnection processes more generally. For example, Fox, Bhattacharjee, and Germaschewski (2011, 2012) performed numerical modeling of laser-driven experiments using particle-in-cell simulations (both with and without a collision operator) and noted the importance of the flux pile up to the reconnection process. Joglekar *et al.* (2014) used a fully implicit 2D Vlasov-Fokker-Planck code to show that in high- β laser-generated plasmas heat flows rather than Alfvénic flows dictate the reconnection rate. Supporting modeling identified the role of anisotropic electron pressure in explaining the enhanced reconnection rate seen in the experiments reported by Tubman *et al.* (2021).

Proton imaging has also been used successfully to diagnose magnetic fields in other types of laser-driven reconnection experiments. For example, Palmer *et al.* (2019) explored reconnection of fields generated by higher ($\sim 10^{18}$ W cm $^{-2}$) laser intensities through proton deflectometry measurements. Figure 19 illustrates a time history of data taken along with the 2D magnetic-field maps reconstructed from proton images

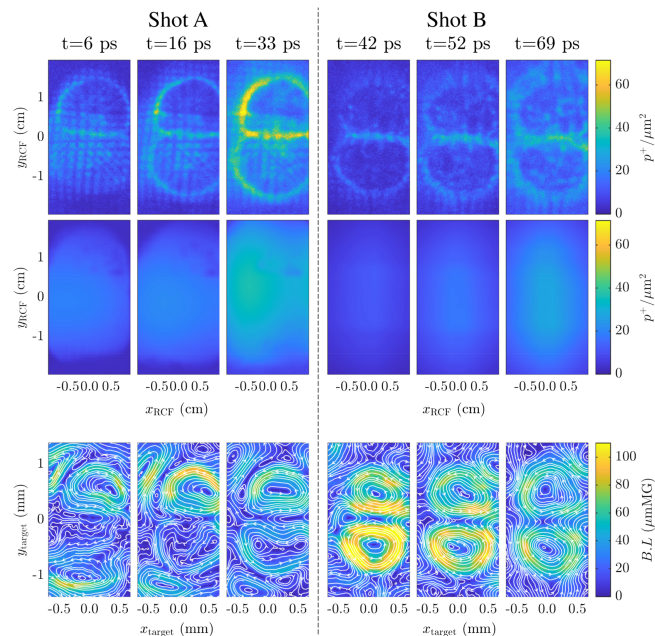


FIG. 19. Time series for two shots of a high-intensity laser-plasma-driven reconnection experiment in a geometry similar to Fig. 18. Top row: the measured proton fluence at the detector plane. Middle row: the calculated undisturbed beam fluence at the detector plane. Bottom row: the retrieved path-integrated magnetic fields at the interaction plane. The white contours with arrows show the topology of the calculated magnetic fields. Adapted from Palmer *et al.*, 2019.

using a field-reconstruction algorithm; see Sec. III.C. These maps showed faster dissipation of magnetic fields at the midplane compared to the outer plane, confirming that reconnection was taking place in the experiment on a time-scale of tens of picoseconds.³

Alternative laser-driven reconnection geometries have also been developed and studied using proton imaging. Fiksel *et al.* (2014) employed externally applied opposing magnetic fields driven together by expanding laser plumes, and Chien *et al.* (2019) used laser interactions to drive currents through U-shaped coils configured in a reconnection geometry.

C. Weibel instabilities

Weibel-type filamentation instabilities (Fried, 1959; Weibel, 1959; Davidson *et al.*, 1972) are ubiquitous in laboratory and astrophysical plasmas. They arise in plasmas whose particle distribution functions have significant velocity-space anisotropy. The velocity-space anisotropy includes cases where the temperature $T_j = \langle mv_j^2/2 \rangle$ differs among the three directions, where j is one of (x, y, z) , and can be driven by counterstreaming particle beams that produce an effective anisotropy. The counterstreaming between a hot forward particle population, balanced by a cold return current, which arises in situations of large heat flux, is another source of anisotropy important for electron-driven Weibel. The instability grows predominantly with wave number k aligned along the cold direction(s). The instability can play a broad role in plasmas, including magnetic-field generation in the early Universe and magnetic-field generation and amplification in high-Mach-number shocks.

The fundamental Weibel mechanism is that the large counterstreaming currents along the hot direction tend to pinch and coalesce into current-carrying filaments, and the forces driving coalescence are sufficient to overcome the transverse plasma pressure along the cold directions. Transverse magnetic fields associated with the current filaments then deflect the particle trajectories, reinforcing the filamentation and leading to a positive feedback. The non-linear regime includes rich physics such as the kinking and remerging of magnetized flux tubes.

Ion-driven Weibel instabilities are important in astrophysical plasmas, as the large bulk-flow energy density of ions $M_i n_i V_i^2/2$ can be greater than analogous energy densities of the electron population and can therefore be a larger reservoir of free energy for the Weibel process, producing stronger magnetic fields at larger scales. The ion-Weibel instability was identified in laboratory laser-driven experiments using proton imaging (Fox *et al.*, 2013; Huntington *et al.*, 2015; Park *et al.*, 2015). In the experiments, two plasma plumes were ablated from opposing targets and were then collided. The high

³We note that the large magnification used for this experiment meant that the interaction image extended close to the edge of the proton beam, necessitating detailed modeling of the assumed unperturbed proton fluence; by reducing the magnification so that the unperturbed region around the interaction is larger, it becomes easier to infer the unperturbed proton fluence and thus reduces the potential error of the reconstruction method.

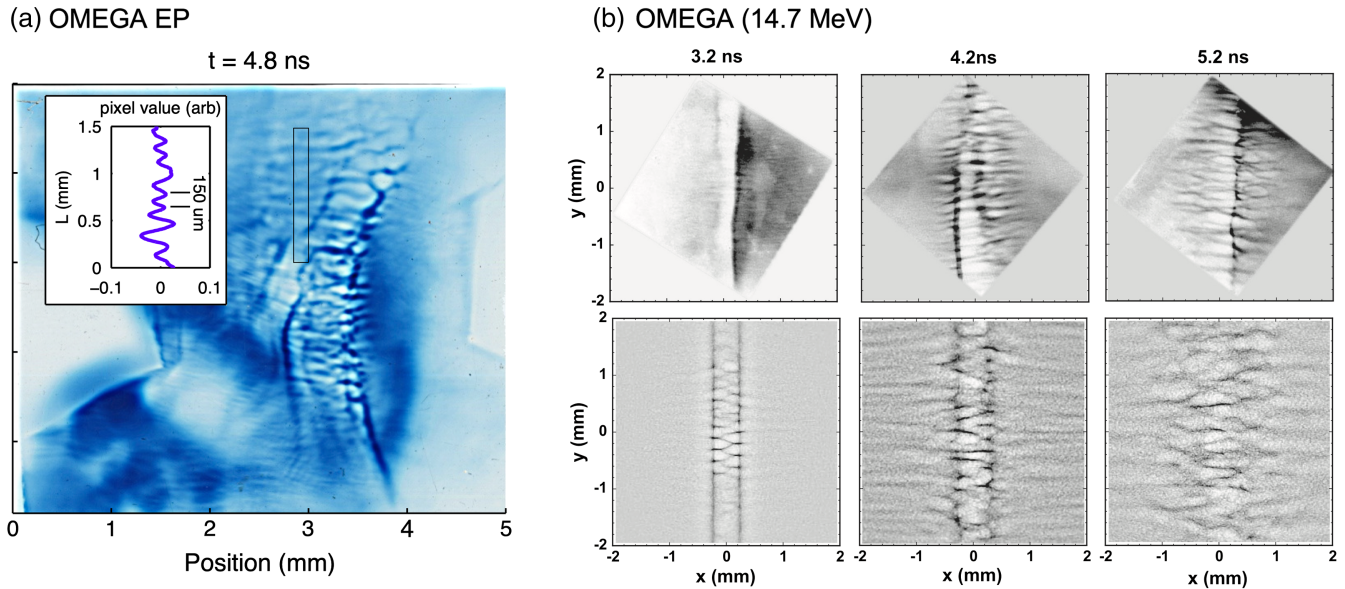


FIG. 20. Observations of filamentary magnetic-field generation by ion-Weibel instability in laser-generated counterstreaming plasmas. The filamentation scale is on the order of the ion-skin depth. (a) Observations at OMEGA EP using TNSA protons at approximately 5 MeV. Adapted from [Fox *et al.*, 2013](#). (b) Top row: observations at OMEGA using D^3He protons at 14.7 MeV. Bottom row: synthetic proton images from 3D PIC simulations modeling the experiments from the top row. Adapted from [Park *et al.*, 2015](#).

temperature and low density of the ablation flows sets up counterstreaming ion populations in the interaction region. Proton imaging directly imaged the magnetized filaments produced in this interaction region by the ion-Weibel instability. [Fox *et al.* \(2013\)](#) observed the time history of the development of the Weibel process and showed that the fast growth and typical filament wavelengths were consistent with the ion-Weibel dispersion relation [Fig. 20(a)]. [Huntington *et al.* \(2015\)](#) and [Park *et al.* \(2015\)](#) measured statistics of the observed filamentary structures, which compared favorably to nonlinear kinetic simulations [Fig. 20(b)].

The electron-Weibel instability is important in relativistic plasmas with strong beam currents and is an important energy-coupling process that can lead to anomalous stopping of relativistic electron beams driven by short-pulse laser-plasma interactions. This type of instability was observed in face-on and side-on proton probing experiments ([Borghesi *et al.*, 2002a](#); [Quinn *et al.*, 2012](#); [Ruyer *et al.*, 2020](#)). Filamentlike magnetic-field structures were observed to persist for an extended time period, a finding that could explain sustained, spatially elongated structures observed in various astrophysical environments.

D. Shocks

Proton imaging has been instrumental in studying the field structures of shocks in laboratory astrophysics experiments. These shocks act to dissipate kinetic ram pressure in systems with supersonic flows and are commonly found in heliospheric and astrophysical systems, including planetary bow shocks, jets, supernova remnants, and galaxy clusters, and are often associated with extremely energetic particles. A key component of shocks is their strong electromagnetic fields. In magnetized shocks, which propagate through a preexisting magnetic field, the global structure of the shock is defined by a

jump in the magnetic field on ion kinetic scales, while strong electric fields in the shock layer can help mediate dissipation by reflecting incoming ions. Similarly, in electrostatic shocks, the shock layer is defined by electric fields on electron kinetic scales. Meanwhile, in electromagnetic shocks, initially unmagnetized counterpropagating plasmas can spontaneously generate magnetic fields through streaming instabilities (such as Weibel ones), leading to shock formation.

[Romagnani *et al.* \(2008a\)](#) performed the first experiments with proton imaging to study shocks. They used a high-intensity laser to create a supersonic plasma plume that expanded into an unmagnetized low-density ambient plasma, driving a collisionless electrostatic shock. TNSA protons were then used to probe the interaction. Proton images, and electric fields reconstructed from the images, showed modulations of the shock front consistent with shock theory and electron kinetic scales; see Fig. 21. The shock speed was estimated by comparing features between different proton images within an RCF stack. A follow-up experiment by [Ahmed *et al.* \(2013\)](#) used TNSA proton imaging to provide further details about how the electrostatic potential in the shock layer evolves during electrostatic shock formation.

[Schaeffer *et al.* \(2017\)](#) first probed magnetized collisionless shocks, using a high-energy laser to drive a supermagnetosonic piston plasma through a magnetized ambient plasma, generating a collisionless shock in the ambient plasma. The shock was probed with TNSA protons, and the resulting proton images showed large proton-fluence variations followed by uniform fluence. Using a 1D reconstruction technique, the fluence variations were shown to correspond to strong magnetic-field compressions at the shock front and a diamagnetic cavity created by the piston behind the shock, which is consistent with features observed in PIC simulations. Further experiments ([Schaeffer *et al.*, 2019](#)) used D^3He protons to image the fields in a magnetized shock precursor;

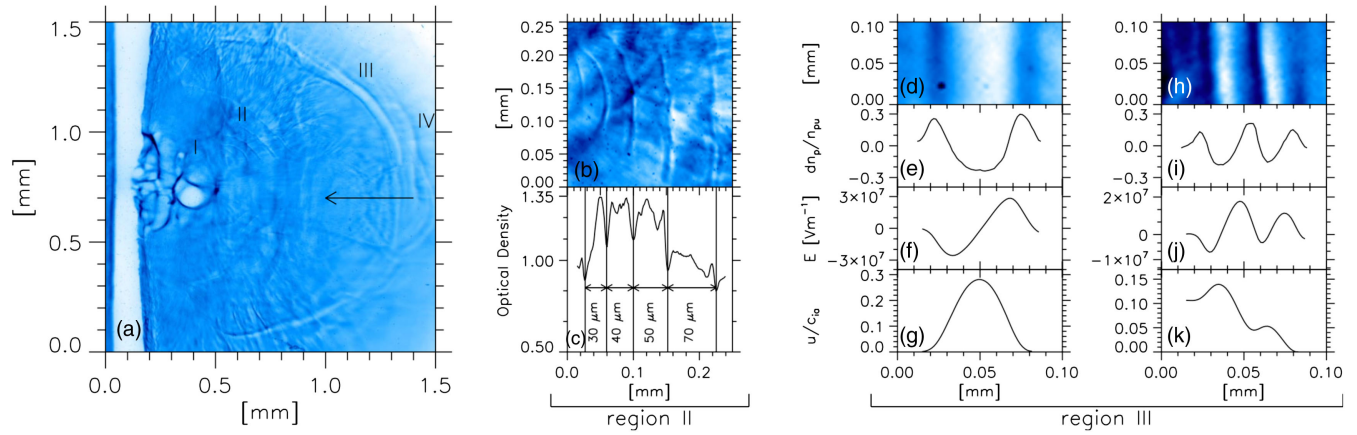


FIG. 21. Data from electrostatic shock experiments in which a dense laser-driven plasma expands into a low-density background plasma. (a) Proton-imaging data taken at the peak of the interaction pulse with 7 MeV TNSA protons. Note the strong modulation associated with the ablating plasma in region I and the modulated pattern ahead of the shock front possibly associated with a reflected ion bunch in region IV. The arrow indicates the laser beam direction. (b)–(c) Details and RCF optical density lineout corresponding to region II, showing modulations associated with a train of solitons. (d)–(k) Details about region III and corresponding lineouts of the probe proton density $\delta n_p/n_{pu}$, the reconstructed electric field E , and the reconstructed normalized ion velocity u/c_{ia} in the cases of (d)–(g) an ion acoustic soliton and (h)–(k) a collisionless shock wave [the collisionless shock detail corresponds to a different shot (not shown)]. Adapted from Romagnani *et al.*, 2008b.

see Fig. 22. These were compared to Thomson scattering data to show how the fields coupled energy from the supersonic piston to an ambient plasma. Piston-driven magnetized shocks were also studied with TNSA protons by Yao *et al.* (2022), who inferred the electric-field structure at the shock front by comparing proton data with a particle-tracing algorithm.

Experiments by Li *et al.* (2019) investigated electromagnetic shocks using a high-energy laser to ablate a target, which generated a jet plasma that expanded into a gasbag. The collision created a counterpropagating plasma that was imaged with D³He protons. The proton images showed the formation of a shock and Weibel filaments on timescales significantly faster than expected from theory, which was attributed to seed Biermann battery fields embedded in the ablated jet plasma. Other experiments by Hua *et al.* (2019) studied self-generated electromagnetic fields in shocks using a shock tube. High-energy lasers incident on one end of the tube created a strong collisional shock, which was probed from multiple angles with TNSA protons. By comparing the proton images from different directions, they showed that magnetic fields, self-generated through the Biermann battery effect, dominated the shock structure, and that electric fields were relatively insignificant.

Levesque and Beesley (2021) utilized proton imaging to study laser-driven bow shocks, which led to the development of a new technique for analyzing the proton data (Levesque *et al.*, 2022). The technique utilizes caustic features to help reconstruct the path-integrated magnetic fields, as well as two proton energies (times) to break the degeneracy of the solutions; see Sec. V.D for further discussion.

E. Jets

An important use for proton imaging has been in laboratory astrophysics experiments that have investigated the dynamical

effect of magnetic fields on supersonic plasma jets. Various astrophysical systems, including active galactic nuclei, pulsar wind nebulae, and young stellar objects, are associated with magnetized jets and outflows. The magnetic fields are thought to explain a number of observed phenomena in these jets, including collimation, clumping, and kinking. In certain conditions, laser-produced plasma jets can be treated as rescaled analogs for astrophysical jets, meaning that tailored laboratory experiments can shed light on these astrophysical phenomena (Blackman and Lebedev, 2022).

Loupas *et al.* (2009) carried out the first such experiment using proton imaging to compare the expansion of a front-side blowoff plasma jet into vacuum with that of a similar jet into an ambient gas and found tentative evidence for electromagnetic fields at the gas-jet boundary from their ~ 3 –5 MeV proton-imaging data. More recently the evolution of the MHD interchange and kink instabilities in a jet created by the irradiation of a cone-shaped target were observed by Li *et al.* (2016). The perturbed magnetic fields associated with both MHD instabilities manifested as quasiperiodic proton-fluence structures in the proton-imaging data. It was then demonstrated that this laboratory jet was a reasonable analog to the Crab Nebula jet under appropriate rescaling, supporting the idea that MHD instabilities provide a plausible explanation for the periodic oscillations in the Crab Nebula jet’s direction that were previously detected by the Chandra X-ray Observatory.

By contrast, another experiment by Gao *et al.* (2019) successfully realized magnetically collimated, stable supersonic jets using laser beams focused onto a hollow ring configuration. The combined use of an electromagnetic-field-reconstruction algorithm applied directly to the proton-imaging data and particle-tracing with FLASH simulations showed that the experiment realized megagauss magnetic fields; see Fig. 23. Given other plasma jet parameters, fields of this strength were sufficient to efficiently collimate the jet, as

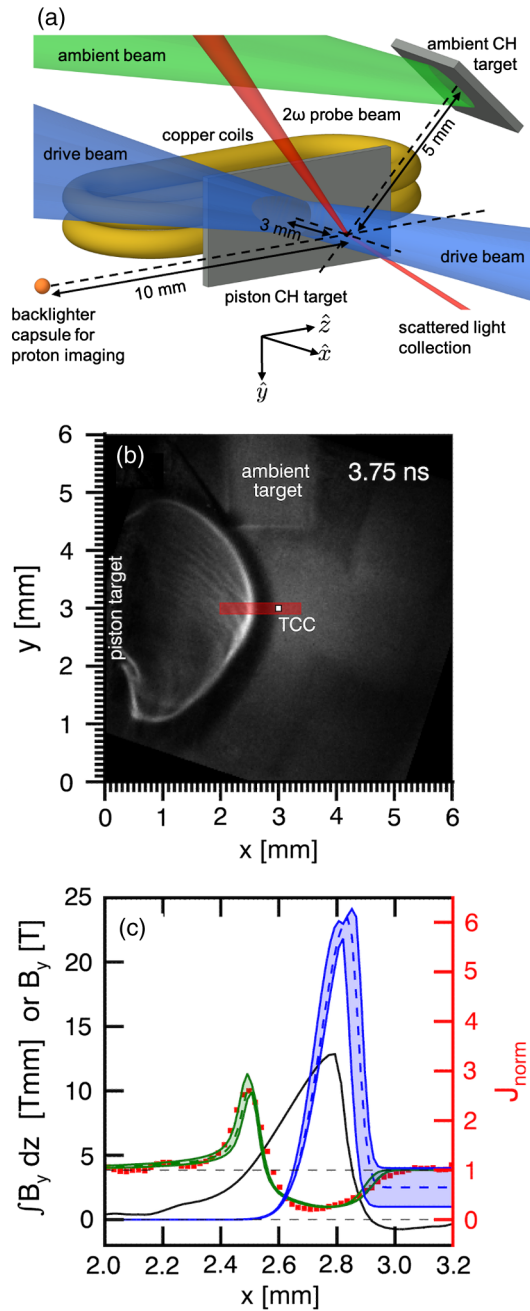


FIG. 22. (a) Data from a magnetized shock experiment shown schematically. (b) Proton image taken at 3.75 ns using 14.7 MeV D^3He protons. The laser is incident from the right and the plasma expands to the right. (c) Proton intensity (red squares) taken from the shaded red region in (b), normalized to the mean intensity, and the associated reconstructed path-integrated magnetic field $\int B_y dz$ (black solid line). Also shown is the normalized proton intensity (green dashed line) forward modeled from a 2D synthetic magnetic field $B_y(x, z)$, which has the dashed blue profile at $z = 0$. The model uncertainties are shown as shaded regions. Adapted from Schaeffer *et al.*, 2019.

well as to realize magnetization parameters (such as the plasma beta and the Hall parameter) of direct relevance to astrophysical systems. Previously Manuel *et al.* (2015) first used proton imaging to look at a magnetized jet with inconclusive results.

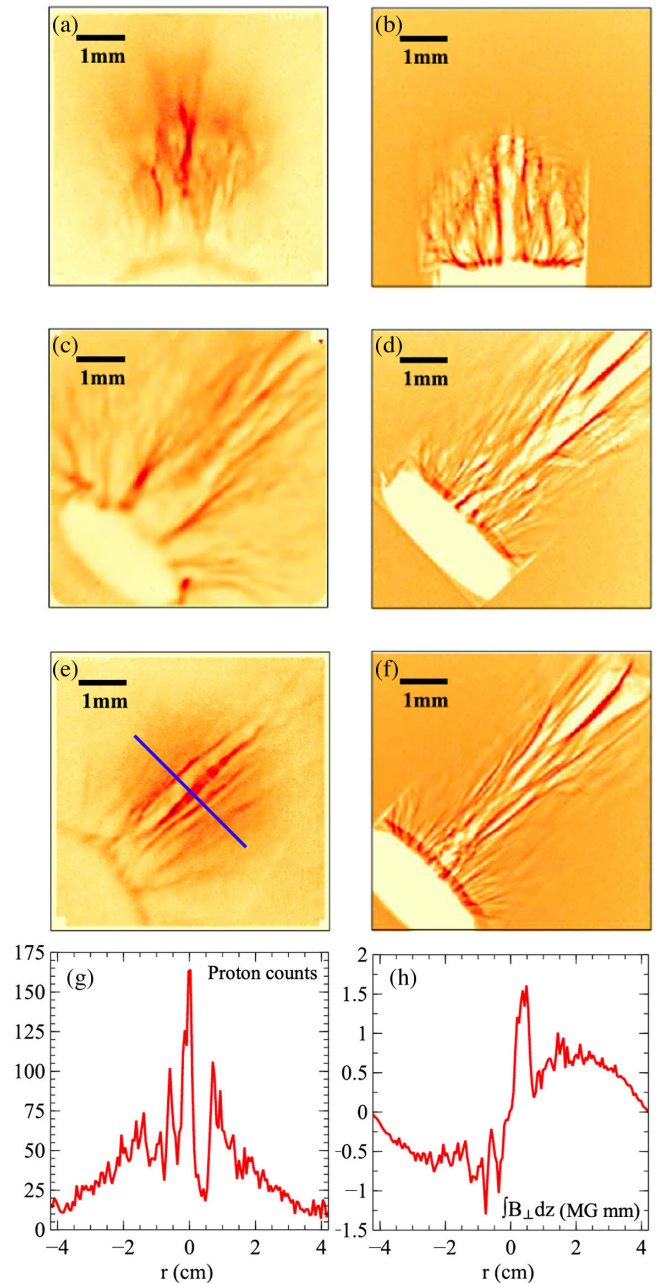


FIG. 23. Proton images of laser-driven magnetized, supersonic jets. For this experiment, 10 kJ of laser energy (20 beams, each with 500 J of energy) was focused over 1 ns into a hollow ring (radius of 800 μm) to produce the jet. D^3He 14.7 MeV proton-imaging data were then collected at different times: (a) 1.6, (c) 2.8, and (e) 3.6 ns after the initiation of the drive beams. 3D FLASH simulations of the experiment were also performed, and (b),(d),(f) synthetic proton images were then generated at these times. In addition, 1D direct inversion analysis was performed on a lineout of the experimental data. The position of the lineout is indicated by the blue line in (e), the lineout itself is shown in (g), and the path-integrated magnetic field is recovered by the inversion shown in (h). Adapted from Gao *et al.*, 2019.

In addition to understanding the dynamics of individual jets, Li *et al.* (2013) studied the evolution of magnetic fields in colliding plasma jets at both collinear and noncollinear angles with the aid of proton imaging. These measurements have

been used to show that the underlying physics of collisions between sufficiently supersonic jets cannot be adequately described by single-fluid hydrodynamics due to the low interjet collisionality between constituent particles, instead requiring two-fluid or kinetic models.

F. Turbulence and dynamos

In recent years, proton imaging has come to play an important role in diagnosing magnetic fields in experiments investigating the evolution of turbulent laser plasmas. Of particular note are a series of experiments that have investigated magnetic-field amplification by turbulent plasma motions on various high-energy laser facilities. It is a long-standing theoretical prediction that turbulent, weakly magnetized plasmas with sufficiently large magnetic Reynolds numbers $Re \equiv u_{\text{rms}}L/\eta$ [where u_{rms} is the root-mean-square (rms) turbulent velocity, L is the driving scale of the turbulence, and η is the plasma's resistivity] can support sustained magnetic-field amplification until dynamical magnetic-field strengths are attained, a mechanism known as the fluctuation or small-scale turbulent dynamo. This mechanism, which provides a plausible explanation for the magnetic fields ubiquitously observed in various astrophysical environments, has been seen in numerous MHD and more recently kinetic simulations [see Rincon (2019) for a review], but had not been observed in any laboratory experiments.

Tzeferacos *et al.* (2018) first realized a small-scale turbulent laser-plasma dynamo on the OMEGA laser. Proton imaging with a $D^3\text{He}$ source helped confirm the formation of a dynamo via measurements of magnetic fields both at the formation of the turbulent plasma and several nanoseconds later. More specifically the application of magnetic-field-reconstruction algorithms to 15 MeV proton radiographs yielded two-dimensional maps of path-integrated stochastic magnetic fields at both times. Further analysis of these maps under various assumed statistical symmetries allowed for values of

the rms strength of the magnetic field, the magnetic-energy spectrum, and a bound on the maximum magnetic-field strength to be inferred. This analysis showed that magnetic energy was amplified ~ 600 times during the course of the experiment, with the characteristic magnetic energies post amplification being a finite fraction of the turbulent kinetic energy. Particle-tracing simulations applied to the magnetic field outputted by MHD simulations of the experiment using the code FLASH corroborated these findings (Tzeferacos *et al.*, 2017).

Bott *et al.* (2021b) also used proton imaging in a related manner for several subsequent experiments on this topic. Time-resolved measurements in a turbulent plasma with order-unity magnetic Prandtl number showed the evolution of stochastic magnetic fields being amplified by the fluctuation dynamo. The proton data were characterized by applying direct inversion analysis to a time sequence of proton images, and path-integrated magnetic-field maps were obtained; see Fig. 24.

Other related experiments include observations of inefficient magnetic-field amplification by supersonic plasma turbulence (Bott *et al.*, 2021a), measurements of the transport of high-energy charged particles through intermittent magnetic fields (Chen *et al.*, 2020), and a demonstration that the key properties of a particular laser-plasma dynamo were insensitive to the plasma's initial conditions (Bott *et al.*, 2022). Proton imaging was also fielded as part of a recent experiment at the NIF by Meinecke *et al.* (2022) that investigated the suppression of heat conduction in magnetized turbulent plasmas. However, the megagauss fields realized in that experiment were sufficiently strong, and the characteristic deflection angle of 14.7 MeV protons was sufficiently large, that electromagnetic-field-reconstruction algorithms used in previous experiments could not reasonably be applied. To overcome this, alternative diagnostic approaches including proton-beam truncation using slits and pinholes were employed to recover the rms and maximum magnetic-field strengths realized in the experiment.

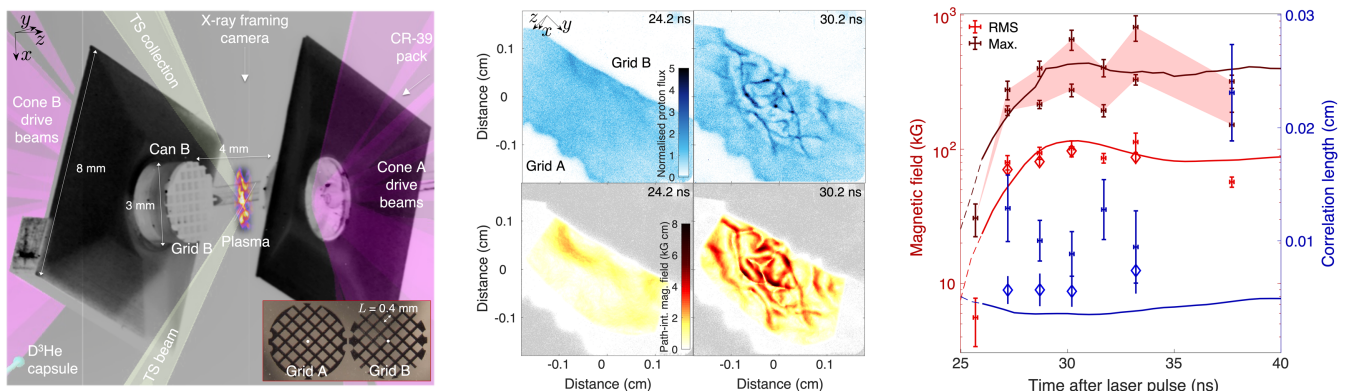


FIG. 24. Proton images of stochastic magnetic fields amplified by a turbulent laser-plasma dynamo. Left panel: Annotated photograph of the experimental platform used to create the dynamo. The $D^3\text{He}$ 14.7 MeV proton images collected during the experiment are shown in the top middle panels, with corresponding path-integrated magnetic-field maps recovered from these images shown in the bottom middle panels. Estimates of the rms and maximum magnetic-field strengths, as well as the correlation lengths, were then recovered from these maps using statistical methods; see the right panel). The results were compared with similar quantities inferred from 3D FLASH simulations of the experiment (see the triangle markers in the right panel), as well as the same quantities computed directly (the solid lines). Adapted from Bott *et al.*, 2021b.

Andy Sha Liao *et al.* (2019) proposed a different dynamo experiment using turbulent ablated blowoff plasmas and conducted experiments showing that a magnetic dynamo was created (Liao *et al.*, 2022). This and other new experiments might open up more potential platforms to study HED dynamos with astrophysical relevance in the laboratory.

G. Ultrafast dynamics

The picosecond-scale temporal resolution obtainable when using a TNSA probe has been exploited in several experiments to investigate the ultrafast dynamics following high-intensity, short-pulse laser interaction with a target or a plasma. Large and transient electromagnetic fields are generated in these interactions, in connection with the large flows of relativistic electrons generated in the irradiated portion of the target. The most energetic electrons typically escape from the target, charging it positively on picosecond timescales. The process of target charge-up and subsequent discharge was observed in some of the earliest proton-imaging experiments investigating 50 TW interactions with wire targets (Borghesi *et al.*, 2003); see Fig. 25.

Quasi-instantaneous target charge-up was observed via strong deflection of protons away from the target surface, causing the appearance of caustics, which were associated with a transverse electric field with an amplitude at the surface of the order of 10^{10} V/m. In these measurements, the shadow

of the unperturbed wire, imprinted by collisional scattering of the protons crossing the wire before it is charged [Fig. 25(a)], acts as a useful fiducial feature for the interpretation of the data: the shadow also appears in the layers in the pack corresponding to later times, as a dose is deposited in these layers by the protons forming the image in Fig. 25(a); see Sec. II.C.4. The charge-discharge cycle was characterized more extensively in follow-up experiments by Quinn *et al.* (2009c), which employed a high-energy proton probe (up to 40 MeV) generated by the Vulcan petawatt laser. This probed a portion of the wire away from the interaction region, which allowed the characteristic time (~ 20 ps) over which target neutralization occurs to be reconstructed. The target charging measured in these studies was found to be consistent with the number of escaping electrons evaluated from self-consistent models. A modified proton-imaging setup (Quinn *et al.*, 2009b), in which the wire was tilted away from the vertical position within the plane containing the proton beam's axis, allowed the early phases of these dynamics, in which an electric field is seen to spread from the interaction region along the target at a velocity close to the speed of light, to be resolved (Quinn *et al.*, 2009a). The field was interpreted, with the help of PIC simulations, as a surface electromagnetic mode generated by the ultrafast motion of the electrons escaping from the target (similar to the emission from a transient antenna).

Kar *et al.* (2016) further investigated the dynamics of this surface mode by characterizing the propagation along millimeter-length wires connected to the laser-irradiated target. These studies, mostly carried out employing a self-imaging scheme, where the proton probe is provided by the same laser-irradiated target that produces the electromagnetic mode (Ahmed *et al.*, 2016), have highlighted its nature as a unipolar electromagnetic pulse of temporal duration comparable to the target discharge time characterized in the earlier experiments (Quinn *et al.*, 2009c). This characterization, carried out with bespoke targets where the length of wire within the probe field of view is maximized, has been at the basis of methods for TNSA proton-beam conditioning in suitably designed helical coil targets, as presented by Kar *et al.* (2016).

Electron energization at the irradiated target surface is also at the basis of the TNSA mechanism for proton acceleration, which was discussed in Sec. II.A.1. Experiments by Romagnani *et al.* (2005) employed proton backlighting (using a TNSA probe from a separate foil) to detect the electric fields associated with TNSA acceleration from the rear surface of a laser-irradiated target at $I \sim 10^{19}$ W cm⁻². Careful temporal synchronization, as well as exploitation of the multiframe capability of RCF stack detectors, led to the detection of the highly transient, Gaussian-shaped TNSA sheath field. The data were used to benchmark TNSA expansion models, which were in substantial agreement with the experimental results.

Romagnani *et al.* (2019) also reported the characterization of the field associated with the propagation of relativistic electrons in the interior of a target. This experiment, which employed a petawatt-driven high-energy proton probe, exploited the capability of high-energy protons to penetrate through dense matter, while at the same time using a target design aimed to minimize collisional scattering and the

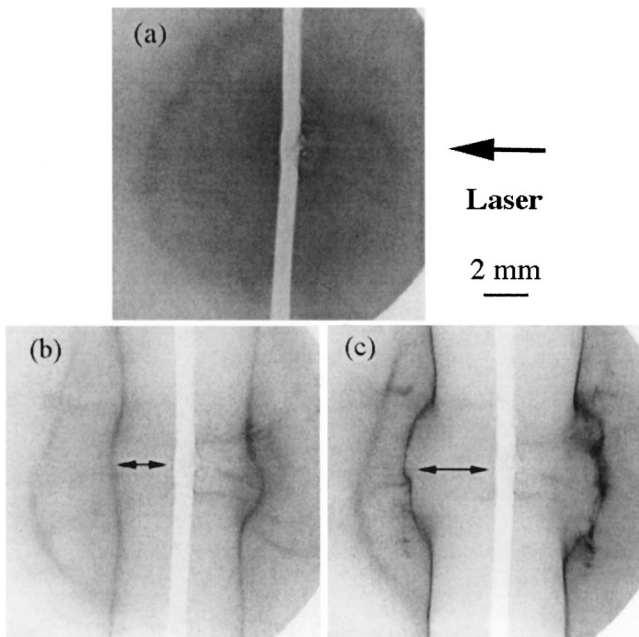


FIG. 25. TNSA proton images taken during laser irradiation of a 50 μm Ta wire (vertical stripe at the center of the images). The frames are three RCF layers from the same shot and refer to different probing times ahead of the peak of the interaction pulse: (a) early time where the proton beam is largely undisturbed ($E_p \sim 8$ MeV, $t \sim -12$ ps); (b),(c) time close to the peak interaction, where the proton beam is modified significantly due to charging of the Ta wire that deflects the protons away from the wire. (b) $E_p \sim 7$ MeV, $t \sim -8$ ps. (c) $E_p \sim 6$ MeV, $t \sim -3$ ps. Adapted from Borghesi *et al.*, 2003.

corresponding spatial resolution degradation. The data provided evidence of magnetized filamentation of the electron current within the target, which, via a comparison with hybrid simulations, was attributed to resistive processes. The angular opening of the electron beam injected in the target is another quantity that could be directly inferred from the data.

Complex plasma dynamics are also initiated when an intense laser pulse propagates through an underdense plasma. Several experiments were carried out to investigate this scenario, with the aim of measuring the electric and magnetic field generated as a plasma channel is formed and, additionally, of obtaining information on the propagation and channel features in near-critical plasma where optical probing may be difficult. Experiments by Kar *et al.* (2007) investigated the formation of a charge-displacement channel in near-critical plasma following the propagation of an intense 100 TW, picosecond pulse through a gas jet. A moving evacuated region was observed in the proton images, in coincidence with the position of the laser pulse, which was consistent with a radial space-charge field within the channel setup by electron displacement by the pulse's ponderomotive force. The walls of a channel expanding from the interaction regions are seen to develop after the pulse has passed, together with the appearance of a region of proton accumulation along the propagation axis, which was later interpreted (Romagnani *et al.*, 2010) as the signature of a long-lived azimuthal magnetic field within the channel.

More complex channel structures were observed in experiments by Willingale *et al.* (2011a, 2013) performed on the OMEGA EP laser, investigating the propagation of 1–8 ps, kilojoule-class laser through an underdense, millimeter-scale preformed plasma plume. The time-resolved formation of an evacuated channel was also observed in this experiment, which highlighted a number of additional features, such as filamentation at the channel's end, channel wall modulations (tentatively associated to the formation of surface waves), as well as the copious appearance of bubblelike structures within the interaction region. This is a recurring circumstance in these types of experiments (Borghesi *et al.*, 2002a; Romagnani *et al.*, 2010; Sarri *et al.*, 2010b). Through comparison with PIC simulations, these structures have been identified as late-time remnants (electromagnetic postsolitons) of solitary structures (solitons) originating from local trapping of frequency down-shifted laser radiation in cavitating plasma regions (Bulanov *et al.*, 1992; Naumova *et al.*, 2001).

H. HED hydrodynamic instabilities

Creating and studying hydrodynamic instabilities in HED environments [including Rayleigh-Taylor (RT) (Rayleigh, 1882; Taylor, 1931), Richtmyer-Meshkov (RM) (Richtmyer, 1960; Meshkov, 1969), and Kelvin-Helmholtz (KH) instabilities (Thomson, 1880)] is of particular interest in the study of HED phenomena such as core-collapse supernovae (Swisher *et al.*, 2015), accretion disks (Balbus and Hawley, 1991), ICF implosions (Lindl *et al.*, 2004; Sadler, Li, and Haines, 2020), or pulsed power pinches (Harris, 1962). These instabilities are present in many strongly driven plasma systems and can lead to turbulence (Flippo *et al.*, 2016) and mixing of materials that can significantly change the behavior and understanding of

experiments and phenomena. The addition of self-generated electromagnetic fields makes these systems especially complicated and not well studied experimentally, as access is often limited to highly penetrating x rays.

Proton imaging, as opposed to x-ray imaging, is uniquely suited to observe the electromagnetic fields in these HED experiments and has been employed with some success to date. These self-generated fields, as well as applied fields, can change the plasma properties and can be crucial to understanding the evolution of instabilities like RT (Srinivasan, Dimonte, and Tang, 2012; Modica, Plewa, and Zhiglo, 2013; Song and Srinivasan, 2020), ablative RT (García-Rubio *et al.*, 2021), RM (Samtaney, 2003; Shen *et al.*, 2019, 2020), and KH (Ryu, Jones, and Frank, 2000; Modestov *et al.*, 2014; Sadler *et al.*, 2022), along with a newly discovered composition instability (Sadler, Li, and Flippo, 2020). This includes the possibility of stabilizing these instabilities or curtailing their growth with external fields (Rosensweig, 1979; Sano, Inoue, and Nishihara, 2013; Srinivasan and Tang, 2013; Praturi and Girimaji, 2019). Some of the first HED experiments to use proton imaging to study hydrodynamic instabilities were done by Manuel *et al.* (2012) using a laser-driven ablative RT platform and a D^3He proton source. The results showed that the RT instability can lead to self-generated fields, as predicted. A summary is shown in Fig. 26, where a CH target with sinusoidal perturbations was driven by lasers [Fig. 26(a)] and the observed RT growth caused Biermann-generated magnetic fields [Fig. 26(b)] to grow from 3 to 10 T [Figs. 26(d) and 26(e)]. However, these fields were 10^4 times too small to affect the hydrodynamics directly. Other experiments showed RT bubble growth using a laser-driven foil [see Figs. 26(f) and 27(g)] with either transverse (Gao *et al.*, 2012) or longitudinal (Gao *et al.*, 2013) proton imaging of CH targets. More recent experiments have attempted to look at the self-generated magnetic fields inside denser HED shock-tube targets, where Coulomb scattering is an issue (Lu *et al.*, 2020) and where the fields can change the heat flow in these targets, thereby changing the instability growth (Sadler *et al.*, 2022).

I. Inertial-Confinement Fusion

The ultimate goal of ICF is ignition and high gain, which requires that a cryogenic deuterium-tritium (DT) spherical capsule be symmetrically imploded to reach sufficiently high temperature and density. Such an implosion results in a small mass of low-density, hot fuel at the center, surrounded by a larger mass of high-density, low temperature fuel (Nuckolls *et al.*, 1972; McCrory *et al.*, 1988; Lindl, 1995; Atzeni and Meyer-ter-Vehn, 2004; Hurricane *et al.*, 2014; Betti and Hurricane, 2016). Shock coalescence ignites the hot spot, and a self-sustaining burn wave subsequently propagates into the main fuel region. The symmetry requirements impose strict constraints for achieving fusion ignition (Nuckolls *et al.*, 1972; McCrory *et al.*, 1988; Lindl, 1995; Atzeni and Meyer-ter-Vehn, 2004; Glenzer *et al.*, 2010; Li *et al.*, 2010; Hurricane *et al.*, 2014; Betti and Hurricane, 2016). The tolerable drive asymmetry of an implosion, in a time-integrated sense, is less than 1% to 2%, depending on the ignition margin (Lindl, 1995; Atzeni and Meyer-ter-Vehn, 2004; Glenzer *et al.*, 2010; Li *et al.*, 2010; Hurricane *et al.*, 2014; Betti

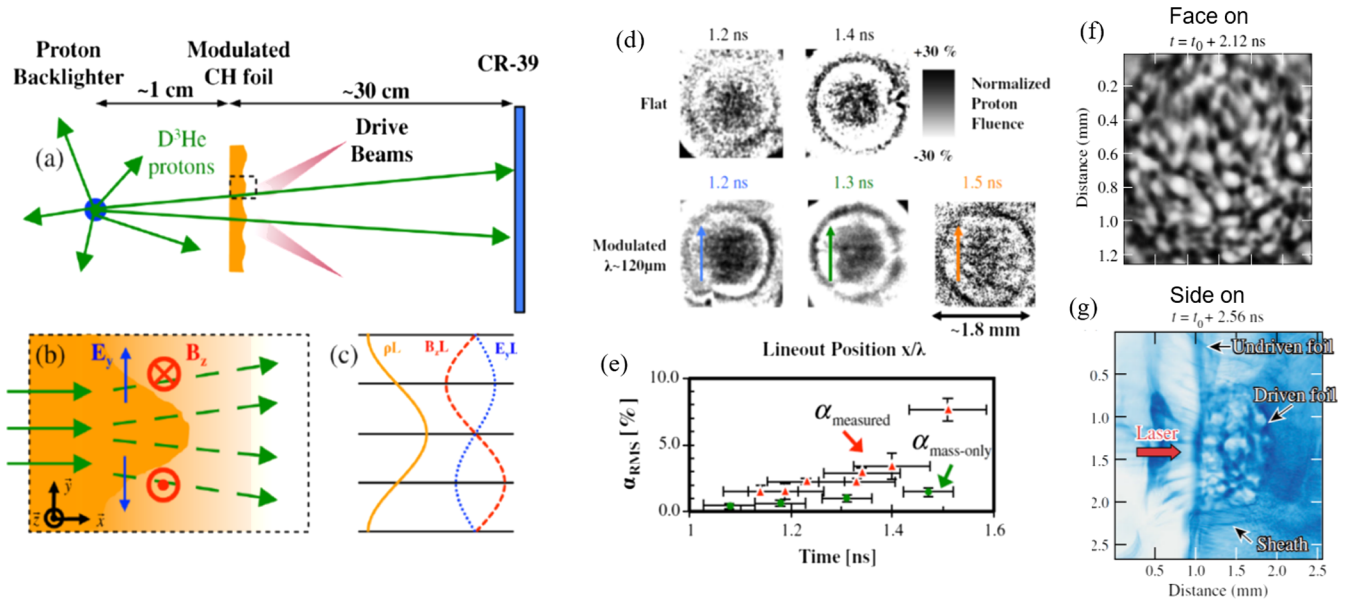


FIG. 26. (a) Schematic of the experimental setup used to image CH foils with 2D seed perturbations using D^3He proton sources. (b) Expanded view of proton deflections (green arrows) due to RT-induced density, as well as electric-field (blue arrows) and magnetic-field (red symbols) modulations in the target. (c) Path-integrated quantities (arbitrary units) are shown during the linear growth phase. (d) Sample proton-fluence images for flat and modulated foils; scale size is given in the target plane and lineout direction is indicated. Proton fluence is normalized for comparison across different shots. (e) Measured rms fluence variations (red triangles) in proton images. Expected rms variation due to the mass only (green circles) was calculated using density distributions from x-ray data. Adapted from Manuel *et al.*, 2012. (f) Face-on proton image of a 15- μ m-thick CH foil taken with 25 MeV TNSA protons at 2.12 ns after irradiation. Adapted from Gao *et al.*, 2013. (g) Side-on image using 13 MeV TNSA protons at 2.56 ns after irradiation. Adapted from Gao *et al.*, 2012.

and Hurricane, 2016). Consequently, understanding and controlling implosion dynamics is essential for ensuring success. Proton radiography has been developed as an important method for diagnosing ICF implosions because it is sensitive both to plasma density and to electromagnetic fields. Additionally, there are promising indications that externally applied magnetic fields can improve hydrodynamic conditions in ICF implosions and thereby increase capsule performance (Perkins *et al.*, 2013; Srinivasan and Tang, 2013; Mostert *et al.*, 2014; Strozzi *et al.*, 2015; Walsh *et al.*, 2019; Walsh, Crilly, and Chittenden, 2020; Moody *et al.*, 2022), and proton imaging provides a vital tool for assessing how such imposed fields evolve as the implosion proceeds (Gotchev *et al.*, 2009; Heuer *et al.*, 2022).

Direct-drive implosions. In direct-drive ICF, a fuel capsule needs to be compressed through illumination by laser light in order to bring the fuel to high temperature and density conducive to fusion and ignition. Earlier work by Mackinnon *et al.* (2006) successfully demonstrated the feasibility of imaging implosions with TNSA protons, backlighting plastic CH capsules that were imploded by six 1- μ m-wavelength laser beams. These were followed by nuclear observations of implosion dynamics for direct-drive spherical capsules on the OMEGA laser using monoenergetic proton imaging (Li *et al.*, 2006a, 2006b). These experiments aimed to probe distributions of self-generated electric and magnetic fields (Igumenshchev *et al.*, 2014), determine areal density ρR by measuring the energy loss of backlighting protons, and sample all the implosion phases from acceleration, through coasting

and deceleration, to final stagnation in order to provide a more comprehensive picture of ICF spherical implosions.

Further proton-imaging experiments by Li *et al.* (2008) revealed the existence of a radial electric field inside the imploding capsules. As shown in Fig. 27, proton images showed both inward and outward directed radial electric fields, suggesting that the radial electric field has reversed direction during an ICF implosion. The magnitude of these electric fields compared well with the field calculated from the pressure gradients predicted by the 1D hydrodynamic code LILAC (Delettrez *et al.*, 1987), indicating that the fields are a consequence of the evolution of the electron pressure gradient. The proton images were also utilized to extract quantitative information about capsule sizes and ρR values at different times, which indicated that the implosions had an approximately 1D performance, with little impact from hydrodynamic instabilities before deceleration.

Additional experiments by Li *et al.* indicated that the apparent degradation of capsule performance at later times relative to the 1D simulation could largely be a consequence of fuel-shell mixing (Li *et al.*, 2002) and implosion asymmetry (Li *et al.*, 2004). Proton images from experiments by Séguin *et al.* (2012) also revealed that electromagnetic fields induced filaments inside the capsule shell. These field structures were further discussed by Manuel *et al.* (2013), who interpreted them as heat-flux-type instabilities driven by the heat conduction from the corona down to the solid ablation layer.

Proton imaging was used by Chang *et al.* (2011) on the first ICF direct-drive experiment to employ an external applied

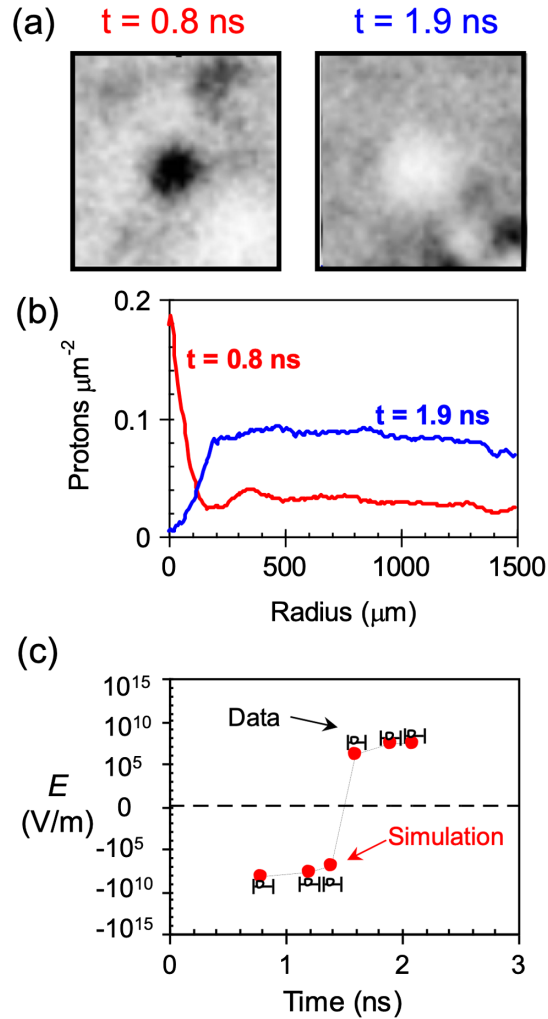


FIG. 27. (a) 15.1 MeV proton images of imploding capsules at two times: $t = 0.8$ and 1.9 ns. In the fluence images, darker shades indicate higher fluence. Comparatively, a fluence peak occurs in the image centers during the early stages of implosion, indicating a “focusing” of imaging protons there, while at later times the fluence is extremely low, or defocused, at the image centers. (b) Radial profiles of the proton-fluence images from (a). (c) Radial electric fields estimated from experimental measurements (open circles) and from LILAC simulations (solid circles) vs implosions times. Horizontal error bars represent uncertainties in backlighter burn time. The differences between simulation and data can largely be accounted for by the effects of proton scattering. Adapted from *Li et al.*, 2008.

magnetic field. The experiments aimed to increase the peak ion temperature of an ICF capsule by strongly magnetizing the plasma’s constituent electrons, reducing thermal conduction across magnetic-field lines and thereby reducing heat loss from the imploded capsule’s hot spot. An $\sim 30\%$ increase to the neutron yield was indeed observed when the external magnetic field was applied. While the proton-imaging data collected were not of sufficient quality for an unambiguous magnetic-field measurement to be made, the characteristic proton-flux inhomogeneity that was observed was consistent with fields that were both trapped and amplified in the imploding capsule.

Laser-driven hohlraums. In the indirect-drive approach to ICF, the capsule implodes in response to a quasiuniform, nearly Planckian x-ray radiation field (hundreds of eV), which is generated by multiple high-power laser pulses irradiating a high-Z enclosure called a hohlraum (*Lindl, 1995*). The x-ray radiation drives the implosion of a cryogenic DT capsule contained within a low-Z ablator, leading to the achievement of high temperature, high-density, and tremendous plasma pressure in the compressed core, and potentially resulting in hot-spot ignition and a self-sustaining fusion burn wave that subsequently propagates into the main fuel region for high-energy gain. In addition, hohlraum-generated x-ray drives can create extreme plasma conditions and have served as an important platform for studying a wide range of basic and applied high-energy-density physics (*Lindl, 1995; Atzeni and Meyer-ter-Vehn, 2004*), including laboratory astrophysics, space physics, nuclear physics, and material sciences.

In diagnosing plasma conditions and field structures generated in a laser-irradiated hohlraum, proton imaging plays an important role in providing physics insight into the hohlraum dynamics and x-ray-driven implosions, impacting the ongoing ignition experiments at the NIF. For example, experiments by *Li et al.* (2009, 2010, 2012) utilizing proton imaging to measure the spatial structure and temporal evolution of plasma blowing off from the hohlraum wall revealed how the fill gas compresses the wall blowoff, inhibits plasma jet formation, and impedes plasma stagnation in the hohlraum interior. These experiments also showed that the magnetic field is rapidly convected by the heat flux via the Nernst effect, which was ~ 10 times faster than the convection by the plasma fluid from expanded wall blowoff. This results in the inhibition of heat transfer from the gas region in the laser beam paths to the surrounding cold gas and in a subsequent increase in local plasma temperature. The experiments further showed that interpenetration of the two materials (gas and wall) occurs due to the classical Rayleigh-Taylor instability as the lighter, decelerating ionized fill gas pushes against the heavier, expanding gold wall blowoff.

Further experiments by *Li et al.* (2012) deployed proton imaging to address plasma flow dynamics in hohlraums by providing the first physics picture of the process of hohlraum plasma stagnation. Using a Au hohlraum filled with neopentane gas (C_5H_{12}), the resulting proton-fluence patterns indicated that no high-density plasma jets were formed, that the fill gas along the laser beam path is fully ionized, and that the interfaces between the gas plasma and the Au wall blowoff are constrained near the wall surface. The proton images also revealed a unique five-prong, asterisklike pattern that is a consequence of the OMEGA laser beam distribution. Spherical CH targets driven in both gas-filled Au hohlraums and CH-lined vacuum Au hohlraums were used to explore this mechanism further, as shown in Fig. 28. The results show that protons were focused onto the gaps (high-fluence spokes) for the gas-filled hohlraum [Fig. 28(a)] but were deflected away from the spokes in the CH-lined vacuum hohlraum [Fig. 28(b)]. By symmetry these deflections were not due to spontaneously generated magnetic fields; instead, lateral electric fields associated with azimuthally oriented electron pressure gradients (∇P_e) in the plasma plumes and in the radial plasma jets ($E = -\nabla P_e / en_e$) may have been the source

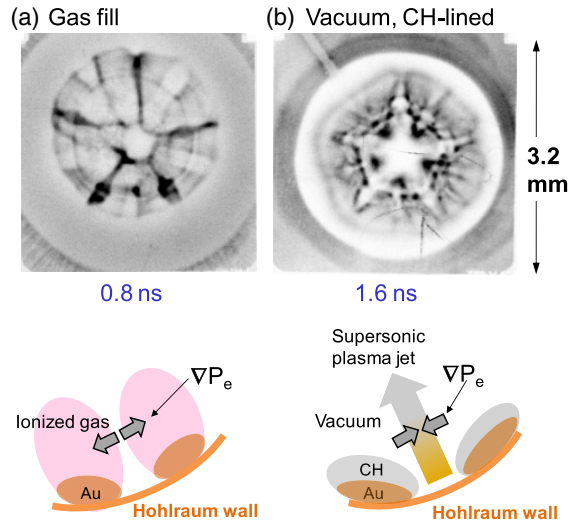


FIG. 28. End-on $D^3\text{He}$ proton images show surpluses in the regions between the pairs of expanding plasma plumes in (a) a gas-filled Au hohlraum but show deficits in (b) a CH-lined, vacuum Au hohlraum. They indicate opposing directions of the self-generated electric fields, as illustrated schematically by the corresponding sketches. Adapted from Li *et al.*, 2012.

of these deflections. Alternatively, the electric field associated with a supersonic heat front generated by the laser-heated gas channels that are in proximity to the capsule might have caused the deflections.

V. FRONTIERS

While the past two decades have seen the invention and widespread adoption of proton imaging as a diagnostic tool for HED plasma experiments, there remain several key challenges that need to be overcome to extend proton imaging into new experimental frontiers. One challenge is how to probe and analyze more complicated electromagnetic fields, including how to measure fields that strongly deflect protons or create caustics and how to disentangle electric and magnetic fields. A related challenge involves how to combine proton images to extract more information, including in three dimensions. Another challenge is how to probe higher-density plasmas, where scattering is a significant issue. A final grand challenge is how to operate a proton-imaging diagnostic in a high-repetition-rate regime. These challenges can be addressed by advancing the field in four key areas: sources (Sec. V.A), detectors (Sec. V.B), algorithms (Sec. V.C), and schemes (Sec. V.D).

A. Advanced sources

Extending the proton-imaging capabilities demonstrated thus far to plasmas with stronger fields or higher densities will require an enhancement of the energy of the protons beyond what is currently available. As discussed, existing TNSA proton sources extend up to 85 MeV with picosecond pulses (Wagner *et al.*, 2016) and to about 60 MeV with tens of picosecond pulses (Ziegler *et al.*, 2021), although the energies that can be used as an efficient probe for imaging will typically

be lower than these cutoffs (as the beam component at the higher energy will have a small divergence and a low number of particles). An obvious route to increasing the proton energies is to use higher power and energy laser drivers. There are a number of multipetawatt systems currently being developed or commissioned, with some aiming to deliver up to 10 PW of power (Danson *et al.*, 2015). Most of these systems will be based on ultrashort pulse technology (tens of femtosecond pulses), but there are also developments with hundreds of femtosecond duration [such as the 10 PW ATON laser at ELI Beamlines (Jourdain *et al.*, 2021)].

The progress achievable in terms of proton energies will depend on the applicability of scaling laws, as well as secondary factors such as how well the beams can be focused and the extent of pulse contrast that can be obtained on these systems. Various attempts have been made to develop reliable scaling laws for proton energies (Fuchs *et al.*, 2006; Passoni, Bertagna, and Zani, 2010), which typically indicate dependencies on laser intensity or laser energy; see Fig. 3. For example, faster scalings than the ponderomotive scaling predicted by earlier TNSA theories (Wilks *et al.*, 2001) have been reported, within given intensity ranges, with ultrashort (tens of femtoseconds) (Zeil *et al.*, 2010), multipicosecond (Simpson *et al.*, 2021), or multikilojoule laser pulses (Flippo *et al.*, 2007; Mariscal *et al.*, 2019). There is an expectation that experimental results in the multipetawatt regime, providing validation to these scaling predictions, will become available soon as some of the new facilities ramp up their operations.

Additionally, there are a variety of approaches that aim to increase TNSA proton energies by enhancing the energy coupled into relativistic electrons, and by increasing their number density and/or energy; see Macchi, Borghesi, and Passoni (2013) for a review. These approaches are based mostly on target engineering and can involve, for example, reducing the mass (Buffechoux *et al.*, 2010) or density of the target, structuring the target surfaces (Margarone *et al.*, 2012), or adding controlled preplasmas (McKenna *et al.*, 2008). The electrons can also be enhanced through additional mechanisms such as direct laser light pressure acceleration (Kluge *et al.*, 2010) or acceleration by surface waves (Ceccotti *et al.*, 2013; Shen, Pukhov, and Qiao, 2021). Many of these approaches have provided evidence of some proton energy increase from flat foil comparators on a proof-of-principle basis and under specific experimental conditions. Although some of these schemes may have a role to play in the development and optimization of future proton-imaging sources, complications and constraints associated with their implementation may limit their applicability and usefulness.

Beyond TNSA, there are a number of alternate mechanisms under investigation that aim to increase the acceleration efficiency and the accelerated ion energy, or at accelerating ion species other than protons. These include radiation pressure acceleration (RPA) (Esirkepov *et al.*, 2004; Robinson *et al.*, 2008) [in the hole boring (Robinson *et al.*, 2012) and light sail (Macchi, Veghini, and Pegoraro, 2009) implementations], shock acceleration (Fiuza *et al.*, 2012), and schemes taking place in relativistic induced transparency (RIT) regimes (Henig *et al.*, 2009; Poole *et al.*, 2018) such as the break-out afterburner approach (Yin *et al.*, 2007). Hybrid regimes involving a combination of these processes

have been highlighted in experiments and have recently led to record proton energies approaching 100 MeV through a combination of RPA, TNSA, and RIT acceleration (Higginson *et al.*, 2021).

Although these processes are promising in terms of energy enhancement, for instance, in view of potential medical use, they typically generate beams that do not possess the laminarity and homogeneity of TNSA beams, and their potential usefulness for proton imaging is therefore unclear at present, at least in the backlighting implementation discussed in this review. Nevertheless, if very-high-energy beams will be produced through any of these processes, there may be prospects for different imaging and deflectometry approaches in which a small portion of a beam is spatially or angularly selected (such as with an aperture) and used to sample a finite region within a target or plasma; see also Sec. II.C.2.

Spatial structuring of the beam may also have a role to play in future proton-imaging sources. For example, methods have been put forward for generating multiple separate sources from a single TNSA beam (Zhai *et al.*, 2019), which may lead to additional backlighting capabilities. Similarly, techniques for producing collimated, quasimonoenergetic beamlets (Kar *et al.*, 2016) may lead to opportunities for “spot scanning” of an extended field distribution, i.e., sampling portions of the field region in separate, consecutive shots and tracking the beamlet’s deflection for each shot.

Increasingly, state-of-the-art ultrashort high-power laser systems provide the opportunity to operate at high repetition rates (1–10 Hz) (Danson *et al.*, 2015). This could enable the generation of secondary particle sources at a commensurately high repetition (rep) rate, provided suitable targets can be used, which offer a refreshed surface for irradiation by consecutive pulses. This may be exploited in future proton-imaging experiments, where a repeated proton pulse is coupled to a high repetition interaction pulse, leading to increased data throughput, higher statistics, and/or shorter experiments. A number of targetry solutions suitable for high-rep-rate operations are currently being developed and tested. These include tape targets, where a continuously moving foil tape allows mechanical refreshment of the laser-impacted surface between shots (Noaman-ul Haq *et al.*, 2017; Dover *et al.*, 2020), free-flowing water sheets (Puyuelo Valdes *et al.*, 2022), and cryogenic hydrogen targets (Obst *et al.*, 2017; Chagovets *et al.*, 2022). The aforementioned approaches can provide planar targets with thicknesses in the micron to tens of micron range, leading to beams with the expected TNSA properties, with beam production demonstrated thus far at repetition rates of up to 1 Hz employing petawatt-class laser pulses. Water targets have also been shown to be capable of sustained kilohertz operation at much lower laser energies (Morrison *et al.*, 2018). Another approach explored is the *in situ* formation of liquid crystal foils (Poole *et al.*, 2016, 2018), which can operate at a more moderate repetition of 0.1 Hz and which provides the capability of varying thickness on demand (from 10 nm to 50 μm). An issue with any high-rep-rate target is the production of debris in the interaction chamber, potentially leading to optics degradation, which may make solutions based on low-density or thinner targets more attractive.

In addition to protons and other heavier ions, electrons are another possible source for imaging. Imaging and deflectometry applications have been reported with electron beams from laser-driven photocathodes (Centurion *et al.*, 2008) and linear accelerators (Zhang *et al.*, 2020), as well as from laser-driven wakefield accelerators. Compared to proton sources, electron sources have a number of attractive features: it is generally easier to generate high-energy ($\sim\text{GeV}$) electrons that can probe larger field strengths; they can reach shorter temporal durations (for instance, femtosecond scale for wakefield accelerators), they are generally easier to operate at high repetition rates, and they are easier to incorporate into the broad range of existing detector designs that are sensitive to electrons. As an example, recent experiments by Zhang *et al.* (2020) studied the electron-Weibel instability generated in a low-density gas-jet plasma using a circularly polarized laser via electron imaging with bunches of 45 MeV electrons from a linear accelerator. Efforts to image relativistic plasmas with wakefield-accelerated electron bunches were reported by Schumaker *et al.* (2013), Zhang *et al.* (2016), and Wan *et al.* (2022, 2023). Schumaker *et al.* (2013) were the first to demonstrate plasma probing applications employing wakefield-accelerated electrons, which enabled the detection of highly transient magnetic fields generated by an ultrashort, intense laser pulse on a solid target. More recently Wan *et al.* (2022, 2023) used very-high-energy (500 MeV) electrons to demonstrate the capability of directly imaging the fields associated with laser-driven plasma wakefields. The experiments highlight a femtosecond temporal resolution, which is well beyond what can currently be achieved with proton beams. It is also straightforward to apply the theory of proton imaging to electrons, including particle-tracing algorithms, although the theory would need to account for relativistic effects given the larger electron speeds involved. A potential disadvantage is that at a given energy electrons also scatter more easily than protons.

B. Advanced detectors

Currently in HED proton imaging, CR-39 (see Sec. II.B.2) and RCF (see Sec. II.B.1) detectors are the most commonly used and are highly efficient. However, they require extensive chemical processing (in the case of CR-39) or a high proton fluence (in the case of RCF), and both require manually labor-intensive digitization efforts. In contrast, besides HED various other proton detectors have been utilized (Bolton *et al.*, 2014; Poludniowski, Allinson, and Evans, 2015). Consequently, more advanced detector systems are currently being developed, especially those that can be used with high-rep-rate laser systems (of the order of 10 shots/h or higher). Here we consider a few systems for the electronic imaging of protons.

Many position sensitive electronic and solid-state detectors have been developed over the years, mainly to support hadron therapy (Poludniowski, Allinson, and Evans, 2015; Johnson, 2018). These include diodes (Wang *et al.*, 2016; Briz *et al.*, 2022), multiwire gas-proportional counters (Sauli, 2014), and cadmium zinc telluride detectors (Simos *et al.*, 2009). However, these detectors suffer from lower spatial resolution and lower sensitivity than CR-39 and RCF, and conversely

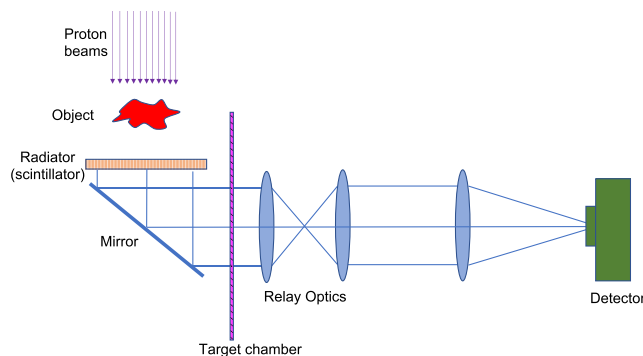


FIG. 29. Sketch of an advanced proton-imaging detector.

more sensitivity to noise from EMP due to short-pulse lasers. Consequently, they have not yet been used for proton imaging.

However, one of the simplest methods for a reusable, repaired electronic proton detector is to convert the proton flux into UV or optical light with a luminescent material, i.e., a scintillator. Scintillators include inorganic or organic phosphorescent compounds, gases, solids, or liquids, the choice of which depends on the needed attributes.⁴ Common solid inorganic examples include CsI(Na), bismuth germanate, lutetium oxyorthosilicate(Ce), lutetium–yttrium oxyorthosilicate, and phosphor screens like rare-earth doped gadolinium oxysulphide with brand names like Lanex, Luminex, and Rapidex. In addition, yttrium aluminum garnet(Ce), gadolinium aluminium gallium garnet(Ce), and lutetium aluminium garnet(Ce) thin screen crystals are made specifically for proton-beam applications (Shalom EO). Examples of organic compounds are doped plastics such as BC Plastics (Bicron) and EJ Plastics (Eljen). Scintillators can have decay times ranging from 1500 μs down to tens of nanoseconds and as short as 2 ns for ZnO:Ga (PhosTech).

The concept of an electronic scintillator-based proton detector system is sketched in Fig. 29. The proton beam goes through the imaged plasma and is recorded by a radiator. The role of the radiator is to convert the proton flux into an optical signal. A careful shield or collimator design is needed so that the radiator does not produce an unwanted signal from the spurious interactions with the background particles. Converted light can be relayed via the optics or the fiber bundle outside the vacuum chamber, where advanced electronics are often situated. The light is then coupled to a CCD camera or CMOS detector, and MCPs can be added to provide gating functionality to further eliminate background signal.

To date, scintillators have been utilized mainly to understand proton-beam profiles in terms of their spatial and energy characteristics. Numerous scintillators have been tested for their optical emission spectrum using monoenergetic proton beams, as well as their response to proton energies. Experimental measurements indicate that scintillators have a nonlinear scaling with proton energy but a linear response to incident flux (Green *et al.*, 2011). These scintillators were also utilized to characterize the TNSA proton-beam profile of different energy bands generated by different stopping

material thicknesses (Green *et al.*, 2011; Bolton *et al.*, 2014; Metzkes *et al.*, 2016; Dover *et al.*, 2017; Huault *et al.*, 2019).

Spatial resolution of scintillators has been characterized for TNSA proton beams using Eljen Technology organic scintillators (Manuel *et al.*, 2020; Tang *et al.*, 2020). A few different scintillator thicknesses were tested with an effective proton source size of 10 μm . The spatial resolution measurement was performed by measuring the point spread function and the contrast of a grid pattern that was placed between the proton source and the detector. The scintillator performance was simultaneously compared with imaging using an RCF detector. The effective resolution limit for the scintillator was measured at ~ 22 μm , compared to ~ 12 μm for the RCF (Tang *et al.*, 2020). The spatial resolution was only weakly dependent on scintillator thicknesses between 50 and 500 μm for > 2 MeV protons, while thicker scintillators showed improved imaging contrasts. To further improve the spatial resolution, a pixelated scintillator can be used. Pixelation is achieved by laser cutting a grid pattern into the scintillator to optically isolate regions. Experiments with TNSA protons measured the performance of different grid patterns and demonstrated a 20% improvement in spatial resolution (Manuel *et al.*, 2020). The current spatial resolution of the scintillators may be sufficient for imaging, but further improvement is required for the spectrum measurements.

When using scintillator-based detectors, the main limitation in terms of temporal resolution is determined by the decay time of the scintillator, or by any temporal gating applied to the detector used to read out the scintillator output [similar considerations apply to MCP detectors (Sokollik *et al.*, 2009)]. If δt_G is the detector's temporal gating, the temporal resolution at the interaction plane will be given by $\delta t = \delta t_G / \mathcal{M}$. With a suitable choice of parameters, matching the ~ 100 ps intrinsic resolution of a D³He source is possible. For example, Sokollik *et al.* (2009), with an unusually large magnification of $\mathcal{M} = 70$ (which would not be suitable for most experiments) and a time gating of $\delta t_G = 4.5$ ns, obtained a temporal resolution of $\delta t \sim 65$ ps. However, even with $\delta t_G \sim 1$ ns [possible in principle if using state-of-the-art scintillators and/or gating (Hu *et al.*, 2018; Zhang *et al.*, 2018; Shevelev *et al.*, 2022)] and a relatively large but more typical magnification $\mathcal{M} \sim 20$, it is challenging to reach temporal resolutions comparable to the picosecond capabilities of RCF and TNSA sources; see Sec. II.C.4.

A volumetric prototype imaging system using a liquid scintillator was developed for hadron therapy dose applications (Darne *et al.*, 2019) but could be adapted and modified for proton imaging. Imaging from several directions would give a tomographic view of the volume and would have information to reconstruct a detailed and possibly 3D proton image with more information than is available with current 2D detectors. Such a system has the possible advantage of capturing all the beam energies efficiently and reconstructing the object in a single shot. It could also be time resolved with high-frame-rate CMOS chips, framing cameras, or streak cameras (depending on the length of emission), and the liquid scintillator has the advantage of being able to be continually replaced in a high-rep-rate system.

⁴See <http://scintillator.lbl.gov/> for an extensive list.

C. Advanced algorithms and analysis

While there have been various developments in the approaches used to analyze proton-imaging data in recent years (for example, using analytically derived field-reconstruction algorithms to perform inverse analysis; see Sec. III.C.4), there remains room for further advances in several different areas. We do not provide an exhaustive list of them here, but instead highlight a few particularly notable areas.

One of these areas is successful differentiation between proton-imaging measurements of electric and magnetic fields. It is not possible to identify whether electric or magnetic fields are responsible for proton-fluence inhomogeneities seen in a single proton image without further assumptions based on either considerations of geometry or the physics of the imaged plasmas. These assumptions are often well founded (Li *et al.*, 2010; Kugland, Ryutov *et al.*, 2012; Huntington *et al.*, 2015; Schaeffer *et al.*, 2019), but in situations where they are not appropriate, establishing alternative approaches would be of great value. One promising possibility involves the simultaneous analysis of two or more images using protons with different initial energies. In situations where the imaged electromagnetic fields evolve over much longer timescales than the transit delays between protons of all energies, it is reasonable to consider that all proton images collected are of approximately the same electromagnetic field. The distinct energy scalings of deflection angles due to magnetic and electric fields then allows for the degeneracy between the two fields that is characteristic of a single proton image to be overcome. Du *et al.* (2021) recently presented an algorithm that implements this schema and also proposed a method for minimizing inaccuracies introduced by the temporal evolution of electromagnetic fields. Because both the TNSA and D³He proton sources characteristically produce protons with differentiated energies (see Sec. II.A), which can be detected independently (see Sec. II.B), this approach should be straightforward to include in future analyses (although more work needs to be done to quantify inherent uncertainties).

A simultaneous analysis of multiple proton images with different initial energies also provides a route toward making progress on another outstanding issue: analyzing images in which there are caustics. As discussed in Sec. III.C.4, it is not possible to uniquely reconstruct path-integrated electromagnetic fields from a single proton image if there are caustics present. However, for slowly evolving electromagnetic fields (in the sense just described), multiple-energy proton images can be used to provide more restrictive constraints on the possible solution space of path-integrated fields. Levesque and Beesley (2021) recently proposed a differential evolution algorithm that realized this idea for proton images (two different energies) of simple magnetic fields that either were quasi one dimensional or possessed spherical symmetry. The algorithm was then successfully used to reconstruct the magnetic fields associated with a bow shock in a laser-produced plasma on its collision with a magnetized obstacle (Levesque *et al.*, 2022). At present it is too computationally expensive to apply this differential evolution algorithm to more general (electro)magnetic fields, although it seems likely that other algorithms may be able to address this limitation.

That being said, the number of proton energies required to reduce the possible solution space to a “unique” solution for more complicated path-integrated electromagnetic fields remains uncertain.

The successful use of a differential evolution algorithm to overcome the issues posed by caustics is emblematic of the promise of the application of machine-learning algorithms for enhanced analyses of proton images. Chen *et al.* (2017) provided a proof of concept in this regard by training an artificial neural network to successfully reconstruct the three-dimensional structure of a simple magnetic field from proton images. It is unclear how well this particular approach would generalize to more complicated electromagnetic fields, but convincing arguments have been made claiming that, once they have been trained, similar neural networks are more computationally efficient than classical analysis algorithms. Similar neural networks could be used to provide improved path-integrated field-reconstruction algorithms by more easily accounting for known limitations in current analysis procedures (for example, uncertainties in the initial beam profiles), as well as quantifying uncertainties. They could also significantly reduce the time taken to perform field reconstructions. The current generation of algorithms typically run for a few hours on a standard laptop computer (Bott *et al.*, 2017), which is long enough to make repeated reconstruction analyzes impractical. Finally, image-recognition-focused machine-learning algorithms could enable more systematic comparisons between synthetic images and measured ones, in turn driving improved standards in the accuracy of field reconstructions.

One final area in which the analysis of proton images could be further developed is the systematic inclusion of scattering models into electromagnetic-field-reconstruction algorithms. As discussed in Sec. II.C.3, such scattering cannot be neglected in many HED experiments when current-generation proton sources are used. While the effect of Coulomb scattering could be minimized using next-generation beams with higher energies (see Sec. V.A), such beams also experience smaller deflections due to electromagnetic fields, which could reduce the feasibility of a successful measurement of the latter. High-quality models of scattering are now commonly incorporated into particle-tracing codes in order to help interpret proton images of electromagnetic fields in high-density laser plasmas; see Sec. III.B.2. They have also previously been used to extract information about plasma densities in ICF experiments directly from proton-imaging data (Mackinnon *et al.*, 2004), but simultaneous inverse analysis of electromagnetic fields has not typically been done. Some recent research suggests that this could have been an oversight. Lu *et al.* (2020) provided a proof of concept for measuring magnetic fields in high-density ($>1 \text{ g/cm}^3$) plasmas by utilizing small aperture proton beams in higher-density objects like a laser-driven shock tube, while Bott *et al.* (2021a) used the broadening of caustic features by scattering in multiple proton images to simultaneously measure magnetic fields and areal densities. If such approaches were to be refined and extended, proton imaging could become a powerful diagnostic on a wider set of experiments than is currently the case.

D. Advanced schemes

In addition to advanced sources and detectors, we discuss here possible new schemes for setting up proton-imaging experiments. These schemes may allow for some of the most significant current limitations of proton-imaging setups to be overcome: specifically, providing characterization of the undisturbed proton fluence, fiducial images for proton deflectometry registration, novel imaging setups utilizing proton optics, and tomographic imaging to obtain 3D measurements.

Characterizing the undistributed proton fluence is critical for implementing numerical reconstruction techniques, but this is often hampered by shot-to-shot variations and nonuniform initial proton distributions. A straightforward way to address this by extending existing setups is to place one detector (for example, a piece of RCF or a thin scintillator) directly in front of an imaged object and another detector behind it. This would allow one to record an image of both the undisturbed proton fluence and the proton deflections on each shot. Similar work has been pursued in hadron therapy (Johnson, 2018).

Another key opportunity is to combine information from both x-ray and proton images (Orimo *et al.*, 2007; Johnson *et al.*, 2022). In this technique, the last piece in an RCF or CR-39 detector stack is an image plate (see Fig. 9), which can record high-energy x rays from the D^3He implosion or TNSA target. This can be used as an alignment or registration fiducial for proton deflectometry (Johnson *et al.*, 2022). Using lower-intensity lasers (Orimo *et al.*, 2007), one can image smaller or less dense objects, and a variant of this scheme uses a thin needle to produce protons and x rays (Ostermayr *et al.*, 2020) along the same line of sight. This dual imaging has been shown with electrons as well (Nishiuchi *et al.*, 2015; Faenov, Pikuz, and Kodama, 2016), which could be used to break the degeneracy between electric and magnetic fields. In this vein, the use of an x-ray free electron laser or coherent source colocated at a laser facility could provide significant advantages when proton and high resolution x-ray images are combined along the same line of sight.

The development of alternative imaging schemes based on scattering and/or diffraction could be useful for enhanced data acquisition. Possibilities include x-ray and electron analogs for Fourier plane imaging (Smalyuk *et al.*, 2001), coded apertures (Ignatyev *et al.*, 2011), and scattering using a proton microscope for dark field imaging [as done with electrons (Martin *et al.*, 2012; Klein *et al.*, 2015)]. Many of these applications would require the development of compact permanent magnet proton optics (Schollmeier *et al.*, 2014) or dynamic laser-driven optics (Toncian *et al.*, 2006). These would also be useful for generally improving imaging capabilities using charged-particle optics [i.e., a proton microscope much smaller than, but similar to, those at FAIR (Mottershead *et al.*, 2003), LANL (Merrill *et al.*, 2009; Prall *et al.*, 2016; Zellner *et al.*, 2021), and PRIOR (Varentsov *et al.*, 2016)] to image the object, in contrast to the simple point-projection imaging currently employed. Small permanent optics have already been used for energy selection (Schollmeier *et al.*, 2014) as well as pulse solenoid optics (Brack *et al.*, 2020), where a particular energy can be selected,

but we are not aware of their use for the implementation of a proton microscope.

Another advanced imaging scheme that, if realized successfully, would lead to much more detailed measurements of electromagnetic fields is tomographic imaging. At present the main limiting factor on tomography is the simultaneous production (and then detection) of multiple high-energy proton beams. The number of high-energy laser facilities equipped with multiple high-intensity laser beams suitable for proton acceleration is currently small (Danson *et al.*, 2015), while fielding more than two D^3He capsules at once is not feasible even at the largest facilities, due to the number of beams required per capsule. Novel targets have been proposed for overcoming this issue (Spiers *et al.*, 2021), which in principle would allow a single short-pulse beam to produce multiple proton beams. Future experiments will be needed to confirm whether such a scheme would work in practice. Even if a few images of the same electromagnetic structure were obtained successfully, such a sparse number of lines of sight falls well short of a standard tomographic imaging setup. This suggests that specific work on sparse-angle tomography algorithms would be warranted. Two possible approaches that have been demonstrated to address this problem have improved the performance of more conventional filtered back-projection schemes (Spiers *et al.*, 2021). Further improvements could be derived by considering studies in related areas, such as the holographic reconstruction via scattering that is done with electrons (Mankos, Scheinfein, and Cowley, 1996).

VI. SUMMARY AND OUTLOOK

In this review, we examined the use of proton imaging as a diagnostic for electric and magnetic fields in HED laser plasmas. In Sec. II, we described the experimental techniques that underpin proton imaging, including the two primary sources of multi-MeV protons (high-intensity laser-driven sources and D^3He -fusion-capsule sources) and the two primary approaches for detecting them (radiochromic film and CR-39 nuclear-track detectors). The characteristic geometry of proton-imaging setups and other important considerations for successful imaging in laser-plasma experiments were also outlined. The theory of how proton images are analyzed in order to extract information about the electric or magnetic fields present in such experiments was reviewed in Sec. III. We explained how a basic physical description of the interaction between charged particles and arbitrary electromagnetic fields allows for both numerical simulations of synthetic proton images of prespecified fields and inverse-analysis techniques (using numerical and/or analytical modeling) that allow for the unique characterization of electromagnetic fields in some (though not all) situations. Section IV presented a broad overview of experiments that have successfully used proton imaging to elucidate many different physical processes of interest in HED plasmas.

While the efficacy of proton imaging as a diagnostic of electromagnetic fields in some HED plasmas is already beyond doubt, there are various different avenues for extending the capabilities of the diagnostic further, which we outlined in Sec. V. One of the primary drivers of these improvements is an ongoing technological progression in

high-power laser technology, as well as an improved understanding of the interaction of these lasers with matter. Taken together these advances have led to a number of promising new proton sources, including some with higher characteristic energies (which can be used to characterize stronger electromagnetic fields than conventional sources) and others with better controlled beam qualities, and the paradigm-shifting prospect of high-repetition-rate sources. This prospect, in particular, has generated much interest in researching new detector technologies that (unlike existing ones) can reliably output sufficiently resolved proton images at equivalent rates to the repetition rate of the laser driving the source. Concurrently there has been renewed effort in the last five years toward developing new techniques for extracting information from proton-imaging data systematically and automatically. Given the recent rate of progress in this area and broader scientific advances in data analysis derived from machine learning, it is not unreasonable to anticipate that there will exist within ten years a plethora of new, sophisticated algorithms that go beyond anything we have described here. Finally, although moving to imaging schemes that are more advanced than the current standard (such as tomographic schemes and schemes attempting “proton optics”) presents several serious practical challenges, the latest research suggests that progress toward realizing such schemes is not an impossible dream.

In short, during the just over two decades since it became practically realizable, proton imaging has proven to be a powerful approach for measuring two of the key physical fields that characterize HED plasmas. Among its many successful applications, it has been used to show magnetic-field generation in both direct-drive and indirect-drive ICF experiments, with significant ramifications for heat transport; it has helped probe the mechanism for kinetic processes in collisionless or weakly collisional plasmas; and it has played a key role in numerous laboratory astrophysics experiments. Looking forward, the ongoing development of high-intensity-laser and fusion-capsule-backlighter proton sources on the highest-energy lasers in the world suggests that proton imaging will continue to be used to probe electric and magnetic fields in the most intriguing new HED plasma experiments for the next decade and beyond.

ACKNOWLEDGMENTS

D. B. S. acknowledges support from the U.S. Department of Energy (DOE) National Nuclear Security Administration (NNSA) under Award No. DE-NA0004033. A. F. A. B. acknowledges support from the UKRI (Grant No. MR/W006723/1). M. B. acknowledges support from the Engineering and Physical Sciences Research Council (Grant No. EP/P010059/1). K. A. F. acknowledges support from the Los Alamos National Laboratory (LANL) Directed Research and Development program under Project No. 20180040DR. LANL is operated by Triad National Security, LLC for the NNSA under Contract No. 89233218CNA000001. W. F. acknowledges support from the NNSA under Award No. DE-NA0004034. J. F. acknowledges the support of the European Research Council (ERC) under the European Union’s Horizon 2020 research and innovation program (Grant Agreement No. 787539). C. L. and F. H. S. acknowledge

support from the U.S. DOE under Contract No. DE-NA0003868 to the NNSA Center of Excellence at the Massachusetts Institute of Technology. H.-S.P.’s work was performed under the auspices of the U.S. DOE by Lawrence Livermore National Laboratory (LLNL) under Contract No. DE-AC52-07NA27344. P. T. acknowledges support for the FLASH Center by the NNSA under Awards No. DE-NA0002724, No. DE-NA0003605, No. DE-NA0003842, No. DE-NA0003934, and No. DE-NA0003856, Subcontracts No. 536203 and No. 630138 with LANL, and Subcontract No. B632670 with LLNL; the NSF under Grant No. PHY-2033925; and the U.S. DOE Office of Science Fusion Energy Sciences under Award No. DE-SC0021990. L. W. acknowledges support from the U.S. National Science Foundation under Grant No. 1751462 and from the U.S. DOE NNSA under Award No. DE-NA0004030.

REFERENCES

- Ahmed, H., *et al.*, 2013, “Time-Resolved Characterization of the Formation of a Collisionless Shock,” *Phys. Rev. Lett.* **110**, 205001.
- Ahmed, H., *et al.*, 2016, “Investigations of ultrafast charge dynamics in laser-irradiated targets by a self probing technique employing laser driven protons,” *Nucl. Instrum. Methods Phys. Res., Sect. A* **829**, 172–175.
- Allen, Matthew, Pravesh K. Patel, Andrew Mackinnon, Dwight Price, Scott Wilks, and Edward Morse, 2004, “Direct Experimental Evidence of Back-Surface Ion Acceleration from Laser-Irradiated Gold Foils,” *Phys. Rev. Lett.* **93**, 265004.
- Arber, T. D., *et al.*, 2015, “Contemporary particle-in-cell approach to laser-plasma modelling,” *Plasma Phys. Controlled Fusion* **57**, 113001.
- Arran, C., C. P. Ridgers, and N. C. Woolsey, 2021, “Proton radiography in background magnetic fields,” *Matter Radiat. Extremes* **6**, 046904.
- Atzeni, S., and J. Meyer-ter-Vehn, 2004, *The Physics of Inertial Fusion* (Oxford University Press, New York).
- Balbus, Steven A., and John F. Hawley, 1991, “A powerful local shear instability in weakly magnetized disks. I. Linear analysis,” *Astrophys. J.* **376**, 214.
- Betti, R., and O. A. Hurricane, 2016, “Inertial-confinement fusion with lasers,” *Nat. Phys.* **12**, 435–448.
- Biermann, L., and A. Schluter, 1951, “Cosmic radiation and cosmic magnetic fields. II. Origin of cosmic magnetic fields,” *Phys. Rev.* **82**, 863–868.
- Bin, J. H., Q. Ji, P. A. Seidl, D. Raftrey, S. Steinke, A. Persaud, K. Nakamura, A. Gonsalves, W. P. Leemans, and T. Schenkel, 2019, “Absolute calibration of GafChromic film for very high flux laser driven ion beams,” *Rev. Sci. Instrum.* **90**, 053301.
- Bird, R., N. Tan, S. V. Luedtke, S. Harrell, M. Taufer, and B. Albright, 2022, “vPIC 2.0: Next generation particle-in-cell simulations,” *IEEE Trans. Parallel Distrib. Syst.* **33**, 952–963.
- Birdsall, C. K., and A. B. Langdon, 1985, *Plasma Physics via Computer Simulation* (McGraw-Hill, New York).
- Blackman, Eric G., and Sergey V. Lebedev, 2022, “Persistent mysteries of jet engines, formation, propagation, and particle acceleration: Have they been addressed experimentally?,” *New Astron. Rev.* **95**, 101661.
- Boehly, T. R., *et al.*, 1995, “The upgrade to the OMEGA laser system,” *Rev. Sci. Instrum.* **66**, 508–510.

- Bolton, P. R., *et al.*, 2014, “Instrumentation for diagnostics and control of laser-accelerated proton (ion) beams,” *Phys. Med.* **30**, 255.
- Borghesi, M., A. J. Mackinnon, D. H. Campbell, D. G. Hicks, S. Kar, P. K. Patel, D. Price, L. Romagnani, A. Schiavi, and O. Willi, 2004, “Multi-MeV Proton Source Investigations in Ultraintense Laser-Foil Interactions,” *Phys. Rev. Lett.* **92**, 055003.
- Borghesi, M., A. Schiavi, D. H. Campbell, M. G. Haines, O. Willi, A. J. MacKinnon, L. A. Gizzi, M. Galimberti, R. J. Clarke, and H. Ruhl, 2001, “Proton imaging: A diagnostic for inertial confinement fusion/fast ignitor studies,” *Plasma Phys. Controlled Fusion* **43**, A267–A276.
- Borghesi, M., *et al.*, 2002a, “Macroscopic Evidence of Soliton Formation in Multiterawatt Laser-Plasma Interaction,” *Phys. Rev. Lett.* **88**, 135002.
- Borghesi, M., *et al.*, 2002b, “Electric-field detection in laser-plasma interaction experiments via the proton imaging technique,” *Phys. Plasmas* **9**, 2214–2220.
- Borghesi, M., *et al.*, 2003, “Measurement of highly transient electrical charging following high-intensity laser-solid interaction,” *Appl. Phys. Lett.* **82**, 1529–1531.
- Bott, A. F. A., C. Graziani, P. Tzeferacos, T. G. White, D. Q. Lamb, G. Gregori, and A. A. Schekochihin, 2017, “Proton imaging of stochastic magnetic fields,” *J. Plasma Phys.* **83**, 905830614.
- Bott, A. F. A., *et al.*, 2021a, “Inefficient Magnetic-Field Amplification in Supersonic Laser-Plasma Turbulence,” *Phys. Rev. Lett.* **127**, 175002.
- Bott, A. F. A., *et al.*, 2021b, “Time-resolved turbulent dynamo in a laser plasma,” *Proc. Natl. Acad. Sci. U.S.A.* **118**, e2015729118.
- Bott, A. F. A., *et al.*, 2022, “Insensitivity of a turbulent laser-plasma dynamo to initial conditions,” *Matter Radiat. Extremes* **7**, 046901.
- Brack, Florian-Emanuel, *et al.*, 2020, “Spectral and spatial shaping of laser-driven proton beams using a pulsed high-field magnet beam-line,” *Sci. Rep.* **10**, 9118.
- Bradford, P., *et al.*, 2018, “EMP control and characterization on high-power laser systems,” *High Power Laser Sci. Eng.* **6**, e21.
- Breschi, E., M. Borghesi, M. Galimberti, D. Giulietti, L. A. Gizzi, and L. Romagnani, 2004, “A new algorithm for spectral and spatial reconstruction of proton beams from dosimetric measurements,” *Nucl. Instrum. Methods Phys. Res., Sect. A* **522**, 190–195.
- Briz, J. A., *et al.*, 2022, “Proton radiographs using position-sensitive silicon detectors and high-resolution scintillators,” *IEEE Trans. Nucl. Sci.* **69**, 696–702.
- Buffechoux, S., *et al.*, 2010, “Hot Electrons Transverse Refluxing in Ultraintense Laser-Solid Interactions,” *Phys. Rev. Lett.* **105**, 015005.
- Bulanov, S. V., I. N. Inovenkov, V. I. Kirsanov, N. M. Naumova, and A. S. Sakharov, 1992, “Nonlinear depletion of ultrashort and relativistically strong laser pulses in an underdense plasma,” *Phys. Fluids B* **4**, 1935–1942.
- Campbell, P. T., C. A. Walsh, B. K. Russell, J. P. Chittenden, A. Crilly, G. Fiksel, P. M. Nilson, A. G. R. Thomas, K. Krushelnick, and L. Willingale, 2020, “Magnetic Signatures of Radiation-Driven Double Ablation Fronts,” *Phys. Rev. Lett.* **125**, 145001.
- Campbell, P. T., *et al.*, 2022, “Measuring magnetic flux suppression in high-power laser-plasma interactions,” *Phys. Plasmas* **29**, 012701.
- Campbell, Paul T., D. Canning, A. E. Hussein, K. D. W. Ratnayaka, A. G. R. Thomas, K. Krushelnick, and L. Willingale, 2019, “Proton beam emittance growth in multipicosecond laser-solid interactions,” *New J. Phys.* **21**, 103021.
- Cecchetti, C. A., *et al.*, 2009, “Magnetic field measurements in laser-produced plasmas via proton deflectometry,” *Phys. Plasmas* **16**, 043102.
- Ceccotti, T., *et al.*, 2013, “Evidence of Resonant Surface-Wave Excitation in the Relativistic Regime through Measurements of Proton Acceleration from Grating Targets,” *Phys. Rev. Lett.* **111**, 185001.
- Centurion, Martin, Peter Reckenthaeler, Sergei A. Trushin, Ferenc Krausz, and Ernst E. Fill, 2008, “Picosecond electron deflectometry of optical-field ionized plasmas,” *Nat. Photonics* **2**, 315–318.
- Chagovets, T., *et al.*, 2022, “A cryogenic hydrogen ribbon for laser driven proton acceleration at Hz-level repetition rate,” *Front. Phys.* **9**, 754423.
- Chang, P. Y., G. Fiksel, M. Hohenberger, J. P. Knauer, R. Betti, F. J. Marshall, D. D. Meyerhofer, F. H. Séguin, and R. D. Petrasso, 2011, “Fusion Yield Enhancement in Magnetized Laser-Driven Implosions,” *Phys. Rev. Lett.* **107**, 035006.
- Chen, L. E., *et al.*, 2020, “Transport of high-energy charged particles through spatially intermittent turbulent magnetic fields,” *Astrophys. J.* **892**, 114.
- Chen, Nicholas F. Y., Muhammad Firmansyah Kasim, Luke Ceurvorst, Naren Ratan, James Sadler, Matthew C. Levy, Raoul Trines, Robert Bingham, and Peter Norreys, 2017, “Machine learning applied to proton radiography of high-energy-density plasmas,” *Phys. Rev. E* **95**, 043305.
- Chen, S. N., *et al.*, 2016, “Absolute dosimetric characterization of gafchromic EBT3 and HDv2 films using commercial flat-bed scanners and evaluation of the scanner response function variability,” *Rev. Sci. Instrum.* **87**, 073301.
- Chien, Abraham, *et al.*, 2019, “Study of a magnetically driven reconnection platform using ultrafast proton radiography,” *Phys. Plasmas* **26**, 062113.
- Chittenden, J. P., S. V. Lebedev, C. A. Jennings, S. N. Bland, and A. Ciardi, 2004, “X-ray generation mechanisms in three-dimensional simulations of wire array Z-pinch,” *Plasma Phys. Controlled Fusion* **46**, B457–B476.
- Clark, E. L., K. Krushelnick, M. Zepf, M. Tatarakis, F. N. Beg, P. A. Norreys, and A. E. Dangor, 2006, “Clark *et al.* Reply,” *Phys. Rev. Lett.* **96**, 249202.
- Clark, E. L., *et al.*, 2000, “Measurements of Energetic Proton Transport through Magnetized Plasma from Intense Laser Interactions with Solids,” *Phys. Rev. Lett.* **84**, 670.
- Colvin, J., and J. Larson, 2014, *Extreme Physics: Properties and Behavior of Matter at Extreme Conditions* (Cambridge University Press, New York).
- Cowan, T. E., *et al.*, 2004, “Ultralow Emittance, Multi-MeV Proton Beams from a Laser Virtual-Cathode Plasma Accelerator,” *Phys. Rev. Lett.* **92**, 204801.
- Craxton, R. S., *et al.*, 2015, “Direct-drive inertial confinement fusion: A review,” *Phys. Plasmas* **22**, 110501.
- Danson, C. N., *et al.*, 2015, “Petawatt and exawatt class lasers worldwide,” *High Power Laser Sci. Eng.* **3**, E3.
- Darne, C. D., F. Alsaena, D. G. Robertson, F. Guan, T. Pan, D. Grosshans, and S. Beddar, 2019, “A proton imaging system using a volumetric liquid scintillator: A preliminary study,” *Biomed. Phys. Eng. Express* **5**, 045032.
- Davidson, Ronald C., David A. Hammer, Irving Haber, and Carl E. Wagner, 1972, “Nonlinear development of electromagnetic instabilities in anisotropic plasmas,” *Phys. Fluids* **15**, 317–333.
- Davies, J. R., and P. V. Heuer, 2022, “Evaluation of direct inversion of proton radiographs in the context of cylindrical implosions,” arXiv:2203.00495.

- Delettrez, J., R. Epstein, M. C. Richardson, P. A. Jaanimagi, and B. L. Henke, 1987, "Effect of laser illumination nonuniformity on the analysis of time-resolved x-ray measurements in UV spherical transport experiments," *Phys. Rev. A* **36**, 3926–3934.
- Derouillat, J., *et al.*, 2018, "SMILEI: A collaborative, open-source, multi-purpose particle-in-cell code for plasma simulation," *Comput. Phys. Commun.* **222**, 351–373.
- Dong, Quan-Li, *et al.*, 2012, "Plasmoid Ejection and Secondary Current Sheet Generation from Magnetic Reconnection in Laser-Plasma Interaction," *Phys. Rev. Lett.* **108**, 215001.
- Dover, N. P., *et al.*, 2017, "Scintillator-based transverse proton beam profiler for laser-plasma ion sources," *Rev. Sci. Instrum.* **88**, 073304.
- Dover, N. P., *et al.*, 2020, "Demonstration of repetitive energetic proton generation by ultra-intense laser interaction with a tape target," *High Energy Density Phys.* **37**, 100847.
- Drake, R. P., 2018, *High Energy Density Physics: Fundamentals, Inertial Fusion and Experimental Astrophysics*, 2nd ed. (Springer, Berlin).
- Dromey, B., *et al.*, 2016, "Picosecond metrology of laser-driven proton bursts," *Nat. Commun.* **7**, 10642.
- Du, Bao, *et al.*, 2021, "Separating the contributions of electric and magnetic fields in deflecting the probes in proton radiography with multiple proton energies," *Matter Radiat. Extremes* **6**, 035903.
- Esirkepov, T., M. Borghesi, S. V. Bulanov, G. Mourou, and T. Tajima, 2004, "Highly Efficient Relativistic-Ion Generation in the Laser-Piston Regime," *Phys. Rev. Lett.* **92**, 175003.
- Everson, E. T., P. Pribyl, C. G. Constantin, A. Zylstra, D. Schaeffer, N. L. Kugland, and C. Niemann, 2009, "Design, construction, and calibration of a three-axis, high-frequency magnetic probe (*B*-dot probe) as a diagnostic for exploding plasmas," *Rev. Sci. Instrum.* **80**, 113505.
- Faenov, Anatoly, Tatiana Pikuz, and Ryosuke Kodama, 2016, "High resolution ion and electron beam radiography with laser-driven clustered sources," in *Laser-Driven Particle Acceleration Towards Radiobiology and Medicine*, edited by Antonio Giulietti (Springer International Publishing, Cham, Switzerland), pp. 271–294.
- Ferguson, S., *et al.*, 2023, "Dual stage approach to laser-driven helical coil proton acceleration," *New J. Phys.* **25**, 013006.
- Fews, A. Peter, and Denis L. Henshaw, 1982, "High resolution alpha particle spectroscopy using CR-39 plastic track detector," *Nucl. Instrum. Methods Phys. Res.* **197**, 517–529.
- Fiksel, G., W. Fox, A. Bhattacharjee, D. H. Barnak, P. Y. Chang, K. Germaschewski, S. X. Hu, and P. M. Nilson, 2014, "Magnetic Reconnection between Colliding Magnetized Laser-Produced Plasma Plumes," *Phys. Rev. Lett.* **113**, 105003.
- Fiuzza, F., A. Stockem, E. Boella, R. A. Fonseca, L. O. Silva, D. Haberberger, S. Tochitsky, C. Gong, W. B. Mori, and C. Joshi, 2012, "Laser-Driven Shock Acceleration of Monoenergetic Ion Beams," *Phys. Rev. Lett.* **109**, 215001.
- Fleisher, R. L., P. B. Price, and R. M. Walker, 1965, "Ion explosion spike mechanism for formation of charged-particle tracks in solids," *J. Appl. Phys.* **36**, 3645.
- Fippo, K., B. M. Hegelich, B. J. Albright, L. Yin, D. C. Gautier, S. Letzring, M. Schollmeier, J. Schreiber, R. Schulze, and J. C. Fernandez, 2007, "Laser-driven ion accelerators: Spectral control, monoenergetic ions and new acceleration mechanisms," *Laser Part. Beams* **25**, 3–8.
- Fippo, K. A., *et al.*, 2016, "Late-Time Mixing Sensitivity to Initial Broadband Surface Roughness in High-Energy-Density Shear Layers," *Phys. Rev. Lett.* **117**, 225001.
- Fonseca, R. A., *et al.*, 2002, "OSIRIS: A three-dimensional, fully relativistic particle in cell code for modeling plasma based accelerators," in *Computational Science—ICCS 2002*, edited by Peter M. A. Sloot, Alfons G. Hoekstra, C. J. Kenneth Tan, and Jack J. Dongarra (Springer, Berlin), pp. 342–351.
- Fox, W., A. Bhattacharjee, and K. Germaschewski, 2011, "Fast Magnetic Reconnection in Laser-Produced Plasma Bubbles," *Phys. Rev. Lett.* **106**, 215003.
- Fox, W., A. Bhattacharjee, and K. Germaschewski, 2012, "Magnetic reconnection in high-energy-density laser-produced plasmas," *Phys. Plasmas* **19**, 056309.
- Fox, W., G. Fiksel, A. Bhattacharjee, P. Y. Chang, K. Germaschewski, S. X. Hu, and P. M. Nilson, 2013, "Filamentation Instability of Counterstreaming Laser-Driven Plasmas," *Phys. Rev. Lett.* **111**, 225002.
- Fox, W., *et al.*, 2020, "Fast magnetic reconnection in highly-extended current sheets at the National Ignition Facility," [arXiv:2003.06351](https://arxiv.org/abs/2003.06351).
- Fried, Burton D., 1959, "Mechanism for instability of transverse plasma waves," *Phys. Fluids* **2**, 337.
- Froula, D., S. H. Glenzer, N. C. Luhmann, and J. Sheffield, 2011, *Plasma Scattering of Electromagnetic Radiation*, 2nd ed. (Academic Press, New York).
- Fryxell, B., K. Olson, P. Ricker, F. X. Timmes, M. Zingale, D. Q. Lamb, P. MacNeice, R. Rosner, J. W. Truran, and H. Tufo, 2000, "FLASH: An adaptive mesh hydrodynamics code for modeling astrophysical thermonuclear flashes," *Astrophys. J. Suppl. Ser.* **131**, 273–334.
- Fuchs, J., *et al.*, 2003, "Spatial Uniformity of Laser-Accelerated Ultrahigh-Current MeV Electron Propagation in Metals and Insulators," *Phys. Rev. Lett.* **91**, 255002.
- Fuchs, J., *et al.*, 2006, "Laser-driven proton scaling laws and new paths towards energy increase," *Nat. Phys.* **2**, 48–54.
- Fuchs, J., *et al.*, 2007, "Laser-Foil Acceleration of High-Energy Protons in Small-Scale Plasma Gradients," *Phys. Rev. Lett.* **99**, 015002.
- Gaillard, S., J. Fuchs, N. Renard-Le Galloudec, and T. E. Cowan, 2006, "Comment on 'Measurements of Energetic Proton Transport through Magnetized Plasma from Intense Laser Interactions with Solids,'" *Phys. Rev. Lett.* **96**, 249201.
- Gaillard, S., J. Fuchs, N. Renard-Le Galloudec, and T. E. Cowan, 2007, "Study of saturation of CR39 nuclear track detectors at high ion fluence and of associated artifact patterns," *Rev. Sci. Instrum.* **78**, 013304.
- Gao, L., P. M. Nilson, I. V. Igumenshev, S. X. Hu, J. R. Davies, C. Stoeckl, M. G. Haines, D. H. Froula, R. Betti, and D. D. Meyerhofer, 2012, "Magnetic Field Generation by the Rayleigh-Taylor Instability in Laser-Driven Planar Plastic Targets," *Phys. Rev. Lett.* **109**, 115001.
- Gao, L., P. M. Nilson, I. V. Igumenshev, M. G. Haines, D. H. Froula, R. Betti, and D. D. Meyerhofer, 2015, "Precision Mapping of Laser-Driven Magnetic Fields and Their Evolution in High-Energy-Density Plasmas," *Phys. Rev. Lett.* **114**, 215003.
- Gao, L., *et al.*, 2013, "Observation of Self-Similarity in the Magnetic Fields Generated by the Ablative Nonlinear Rayleigh-Taylor Instability," *Phys. Rev. Lett.* **110**, 185003.
- Gao, L., *et al.*, 2019, "Mega-gauss plasma jet creation using a ring of laser beams," *Astrophys. J.* **873**, L11.
- Gao, Lan, Hantao Ji, Gennady Fiksel, William Fox, Michelle Evans, and Noel Alfonso, 2016, "Ultrafast proton radiography of the magnetic fields generated by a laser-driven coil current," *Phys. Plasmas* **23**, 043106.
- García-Rubio, F., R. Betti, J. Sanz, and H. Aluie, 2021, "Magnetic-field generation and its effect on ablative Rayleigh-Taylor instability in diffusive ablation fronts," *Phys. Plasmas* **28**, 012103.

- Gargaté, L., R. Bingham, R. A. Fonseca, and L. O. Silva, 2007, “dHybrid: A massively parallel code for hybrid simulations of space plasmas,” *Comput. Phys. Commun.* **176**, 419–425.
- Germaschewski, Kai, William Fox, Stephen Abbott, Narges Ahmadi, Kristofor Maynard, Liang Wang, Hartmut Ruhl, and Amitava Bhattacharjee, 2016, “The plasma simulation code: A modern particle-in-cell code with patch-based load-balancing,” *J. Comput. Phys.* **318**, 305–326.
- Gittings, Michael, *et al.*, 2008, “The RAGE radiation-hydrodynamic code,” *Comput. Sci. Discovery* **1**, 015005.
- Glenzer, S. H., *et al.*, 2010, “Symmetric inertial confinement fusion implosions at ultra-high laser energies,” *Science* **327**, 1228–1231.
- Gotchev, O. V., *et al.*, 2009, “Laser-Driven Magnetic-Flux Compression in High-Energy-Density Plasmas,” *Phys. Rev. Lett.* **103**, 215004.
- Graziani, Carlo, Petros Tzeferacos, Donald Q. Lamb, and Chikang Li, 2017, “Inferring morphology and strength of magnetic fields from proton radiographs,” *Rev. Sci. Instrum.* **88**, 123507.
- Green, J. S., *et al.*, 2011, “Scintillator-based ion beam profiler for diagnosing laser-accelerated ion beams,” in *Laser Acceleration of Electrons, Protons, and Ions and Medical Applications of Laser-Generated Secondary Sources of Radiation and Particles*, edited by W. P. Leemans, E. Esarey, S. M. Hooker, K. W. D. Ledingham, K. Spohr, and P. McKenna, SPIE Proceedings Vol. 8079 (SPIE—International Society for Optical Engineering, Bellingham, WA), p. 807919.
- Gregori, G., B. Reville, and F. Miniati, 2015, “The generation and amplification of intergalactic magnetic fields in analogue laboratory experiments with high power lasers,” *Phys. Rep.* **601**, 1–34.
- Haines, M. G., 1986, “Magnetic-field generation in laser fusion and hot-electron transport,” *Can. J. Phys.* **64**, 912–919.
- Harres, K., *et al.*, 2008, “Development and calibration of a Thomson parabola with microchannel plate for the detection of laser-accelerated MeV ions,” *Rev. Sci. Instrum.* **79**, 093306.
- Harris, E. G., 1962, “Evolution of the magnetic field generated by the Kelvin-Helmholtz instability,” *Phys. Fluids* **5**, 1057.
- Hatchett, Stephen P., *et al.*, 2000, “Electron, photon, and ion beams from the relativistic interaction of petawatt laser pulses with solid targets,” *Phys. Plasmas* **7**, 2076–2082.
- He, X. T., 2016, “The updated advancements of inertial confinement fusion program in china,” *J. Phys. Conf. Ser.* **688**, 012029.
- Henig, A., *et al.*, 2009, “Enhanced Laser-Driven Ion Acceleration in the Relativistic Transparency Regime,” *Phys. Rev. Lett.* **103**, 045002.
- Heuer, P. V., *et al.*, 2022, “Diagnosing magnetic fields in cylindrical implosions with oblique proton radiography,” *Phys. Plasmas* **29**, 072708.
- Hicks, D. G., *et al.*, 2000, “Charged-particle acceleration and energy loss in laser-produced plasmas,” *Phys. Plasmas* **7**, 5106–5117.
- Higginson, A., *et al.*, 2021, “Influence of target-rear-side short scale length density gradients on laser-driven proton acceleration,” *Plasma Phys. Controlled Fusion* **63**, 114001.
- Highland, Virgil L., 1975, “Some practical remarks on multiple scattering,” *Nucl. Instrum. Methods* **129**, 497–499.
- Hu, Chen, *et al.*, 2018, “Temporal response of fast and ultrafast inorganic scintillators,” in *Proceedings of the IEEE Nuclear Science Symposium and Medical Imaging Conference Proceedings (NSS/MIC), Sydney, 2018* (IEEE, New York), pp. 1–2.
- Hua, R., *et al.*, 2019, “Self-Generated Magnetic and Electric Fields at a Mach-6 Shock Front in a Low Density Helium Gas by Dual-Angle Proton Radiography,” *Phys. Rev. Lett.* **123**, 215001.
- Huault, M., *et al.*, 2019, “A 2D scintillator-based proton detector for high repetition rate experiments,” *High Power Laser Sci. Eng.* **7**, e60.
- Huntington, C. M., *et al.*, 2015, “Observation of magnetic field generation via the Weibel instability in interpenetrating plasma flows,” *Nat. Phys.* **11**, 173–176.
- Hurricane, O. A., *et al.*, 2014, “Fuel gain exceeding unity in an inertially confined fusion implosion,” *Nature (London)* **506**, 343–348.
- Ignatyev, K., P. R. T. Munro, D. Chana, R. D. Speller, and A. Olivo, 2011, “Coded apertures allow high-energy x-ray phase contrast imaging with laboratory sources,” *J. Appl. Phys.* **110**, 014906.
- Igmenshchev, I. V., A. B. Zylstra, C. K. Li, P. M. Nilson, V. N. Goncharov, and R. D. Petrasso, 2014, “Self-generated magnetic fields in direct-drive implosion experiments,” *Phys. Plasmas* **21**, 062707.
- Joglekar, A. S., A. G. R. Thomas, W. Fox, and A. Bhattacharjee, 2014, “Magnetic Reconnection in Plasma UNDER Inertial Confinement Fusion Conditions Driven by Heat Flux Effects in Ohm’s Law,” *Phys. Rev. Lett.* **112**, 105004.
- Johnson, C. L., S. Malko, W. Fox, D. B. Schaeffer, G. Fiksel, P. J. Adrian, G. D. Sutcliffe, and A. Birkel, 2022, “Proton deflectometry with *in situ* x-ray reference for absolute measurement of electromagnetic fields in high-energy-density plasmas,” *Rev. Sci. Instrum.* **93**, 023502.
- Johnson, Robert P., 2018, “Review of medical radiography and tomography with proton beams,” *Rep. Prog. Phys.* **81**, 016701.
- Johnson, T. M., *et al.*, 2021, “Yield degradation due to laser drive asymmetry in $D^3\text{He}$ backlit proton radiography experiments at OMEGA,” *Rev. Sci. Instrum.* **92**, 043551.
- Jourdain, N., U. Chaulagain, M. Havlík, D. Kramer, D. Kumar, I. Majerová, V. T. Tikhonchuk, G. Korn, and S. Weber, 2021, “The L4n laser beamline of the P3-installation: Towards high-repetition rate high-energy density physics at ELI-Beamlines,” *Matter Radiat. Extremes* **6**, 015401.
- Kaluza, M., J. Schreiber, M. I. K. Santala, G. D. Tsakiris, K. Eidmann, J. Meyer-ter-Vehn, and K. J. Witte, 2004, “Influence of the Laser Prepulse on Proton Acceleration in Thin-Foil Experiments,” *Phys. Rev. Lett.* **93**, 045003.
- Kanematsu, Nobuyuki, 2008, “Alternative scattering power for gaussian beam model of heavy charged particles,” *Nucl. Instrum. Methods Phys. Res., Sect. B* **266**, 5056–5062.
- Kar, S., A. P. L. Robinson, D. C. Carroll, O. Lundh, K. Markey, P. McKenna, P. Norreys, and M. Zepf, 2009, “Guiding of Relativistic Electron Beams in Solid Targets by Resistively Controlled Magnetic Fields,” *Phys. Rev. Lett.* **102**, 055001.
- Kar, S., *et al.*, 2007, “Dynamics of charge-displacement channeling in intense laser-plasma interactions,” *New J. Phys.* **9**, 402.
- Kar, S., *et al.*, 2016, “Guided post-acceleration of laser-driven ions by a miniature modular structure,” *Nat. Commun.* **7**, 10792.
- Kasim, M. F., A. F. A. Bott, P. Tzeferacos, D. Q. Lamb, G. Gregori, and S. M. Vinko, 2019, “Retrieving fields from proton radiography without source profiles,” *Phys. Rev. E* **100**, 033208.
- Kasim, Muhammad Firmansyah, *et al.*, 2017, “Quantitative shadowgraphy and proton radiography for large intensity modulations,” *Phys. Rev. E* **95**, 023306.
- Kirby, D., S. Green, F. Fiorini, D. Parker, L. Romagnani, D. Doria, S. Kar, C. Lewis, M. Borghesi, and H. Palmans, 2011, “Radiochromic film spectroscopy of laser-accelerated proton beams using the FLUKA code and dosimetry traceable to primary standards,” *Laser Part. Beams* **29**, 231–239.
- Klein, Nathan D., Katie R. Hurley, Z. Vivian Feng, and Christy L. Haynes, 2015, “Dark field transmission electron microscopy as a

- tool for identifying inorganic nanoparticles in biological matrices,” *Anal. Chem.* **87**, 4356–4362.
- Kluge, T., W. Enghardt, S. D. Kraft, U. Schramm, K. Zeil, T. E. Cowan, and M. Bussmann, 2010, “Enhanced laser ion acceleration from mass-limited foils,” *Phys. Plasmas* **17**, 123103.
- Kruer, W. L., and K. Estabrook, 1985, “ $J \times B$ heating by very intense laser light,” *Phys. Fluids* **28**, 430–432.
- Kugland, N. L., D. D. Ryutov, C. Plechaty, J. S. Ross, and H.-S. Park, 2012, “Invited article: Relation between electric and magnetic field structures and their proton-beam images,” *Rev. Sci. Instrum.* **83**, 101301.
- Kugland, N. L., *et al.*, 2012, “Self-organized electromagnetic field structures in laser-produced counter-streaming plasmas,” *Nat. Phys.* **8**, 809–812.
- Kugland, N. L., *et al.*, 2013, “Visualizing electromagnetic fields in laser-produced counter-streaming plasma experiments for collisionless shock laboratory astrophysics,” *Phys. Plasmas* **20**, 056313.
- Lahmann, B., M. Gatu Johnson, J. A. Frenje, Y. Yu. Glebov, H. G. Rinderknecht, F. H. Séguin, G. Sutcliffe, and R. D. Petrasso, 2020, “CR-39 nuclear track detector response to inertial confinement fusion relevant ions,” *Rev. Sci. Instrum.* **91**, 053502.
- Lancia, L., *et al.*, 2014, “Topology of Megagauss Magnetic Fields and of Heat-Carrying Electrons Produced in a High-Power Laser-Solid Interaction,” *Phys. Rev. Lett.* **113**, 235001.
- Langer, Steven H., Ian Karlin, and Michael M. Marinak, 2015, “Performance characteristics of HYDRA—A multi-physics simulation code from LLNL,” in *High Performance Computing for Computational Science—VECPAR 2014*, edited by Michel Daydé, Osni Marques, and Kengo Nakajima (Springer International Publishing, Cham, Switzerland), pp. 173–181.
- Lebedev, S. V., A. Frank, and D. D. Ryutov, 2019, “Exploring astrophysics-relevant magnetohydrodynamics with pulsed-power laboratory facilities,” *Rev. Mod. Phys.* **91**, 025002.
- Levesque, Joseph M., and Lauren J. Beesley, 2021, “Reconstructing magnetic deflections from sets of proton images using differential evolution,” *Rev. Sci. Instrum.* **92**, 093505.
- Levesque, Joseph M., *et al.*, 2022, “Experimental observations of detached bow shock formation in the interaction of a laser-produced plasma with a magnetized obstacle,” *Phys. Plasmas* **29**, 012106.
- Li, C. K., F. H. Séguin, J. A. Frenje, J. R. Rygg, R. D. Petrasso, R. P. J. Town, O. L. Landen, J. P. Knauer, and V. A. Smalyuk, 2007, “Observation of Megagauss-Field Topology Changes due to Magnetic Reconnection in Laser-Produced Plasmas,” *Phys. Rev. Lett.* **99**, 055001.
- Li, C. K., *et al.*, 2002, “Effects of Fuel-Shell Mix upon Direct-Drive, Spherical Implosions on OMEGA,” *Phys. Rev. Lett.* **89**, 165002.
- Li, C. K., *et al.*, 2004, “Effects of Nonuniform Illumination on Implosion Asymmetry in Direct-Drive Inertial Confinement Fusion,” *Phys. Rev. Lett.* **92**, 205001.
- Li, C. K., *et al.*, 2006a, “Monoenergetic proton backlighter for measuring E and B fields and for radiographing implosions and high-energy density plasmas (invited),” *Rev. Sci. Instrum.* **77**, 10E725.
- Li, C. K., *et al.*, 2006b, “Measuring e and b Fields in Laser-Produced Plasmas with Monoenergetic Proton Radiography,” *Phys. Rev. Lett.* **97**, 135003.
- Li, C. K., *et al.*, 2008, “Monoenergetic-Proton-Radiography Measurements of Implosion Dynamics in Direct-Drive Inertial-Confinement Fusion,” *Phys. Rev. Lett.* **100**, 225001.
- Li, C. K., *et al.*, 2009, “Observations of Electromagnetic Fields and Plasma Flow in Hohlraums with Proton Radiography,” *Phys. Rev. Lett.* **102**, 205001.
- Li, C. K., *et al.*, 2010, “Charged-particle probing of x-ray-driven inertial-fusion implosions,” *Science* **327**, 1231–1235.
- Li, C. K., *et al.*, 2012, “Impeding Hohlraum Plasma Stagnation in Inertial-Confinement Fusion,” *Phys. Rev. Lett.* **108**, 025001.
- Li, C. K., *et al.*, 2013, “Structure and Dynamics of Colliding Plasma Jets,” *Phys. Rev. Lett.* **111**, 235003.
- Li, C. K., *et al.*, 2016, “Scaled laboratory experiments explain the kink behaviour of the Crab Nebula jet,” *Nat. Commun.* **7**, 13081.
- Li, C. K., *et al.*, 2019, “Collisionless Shocks Driven by Supersonic Plasma Flows with Self-Generated Magnetic Fields,” *Phys. Rev. Lett.* **123**, 055002.
- Li, D. Y., *et al.*, 2021, “Influence factors of resolution in laser accelerated proton radiography and image deblurring,” *AIP Adv.* **11**, 085316.
- Liao, A., H. Li, K. A. Flippo, Y. Lu, S. Li, A. M. Rasmus, D. Barnak, S. Klein, and C. Kuranz, 2022, “Small-scale turbulent dynamo in laser-driven cone experiments on OMEGA-EP” (to be published).
- Liao, Andy Sha, *et al.*, 2019, “Design of a new turbulent dynamo experiment on the OMEGA-EP,” *Phys. Plasmas* **26**, 032306.
- Lindl, John, 1995, “Development of the indirect-drive approach to inertial confinement fusion and the target physics basis for ignition and gain,” *Phys. Plasmas* **2**, 3933–4024.
- Lindl, John D., Peter Amendt, Richard L. Berger, S. Gail Glendinning, Siegfried H. Glenzer, Steven W. Haan, Robert L. Kauffman, Otto L. Landen, and Laurence J. Suter, 2004, “The physics basis for ignition using indirect-drive targets on the National Ignition Facility,” *Phys. Plasmas* **11**, 339–491.
- Link, A., R. R. Freeman, D. W. Schumacher, and L. D. Van Woerkom, 2011, “Effects of target charging and ion emission on the energy spectrum of emitted electrons,” *Phys. Plasmas* **18**, 053107.
- Lion, Charles, 2010, “The LMJ program: An overview,” *J. Phys. Conf. Ser.* **244**, 012003.
- Loupias, B., *et al.*, 2009, “Propagation of laser-generated plasma jet in an ambient medium,” *Plasma Phys. Controlled Fusion* **51**, 124027.
- Lu, Yingchao, *et al.*, 2020, “Modeling hydrodynamics, magnetic fields, and synthetic radiographs for high-energy-density plasma flows in shock-shear targets,” *Phys. Plasmas* **27**, 012303.
- Macchi, A., M. Borghesi, and M. Passoni, 2013, “Ion acceleration by superintense laser-plasma interaction,” *Rev. Mod. Phys.* **85**, 751–793.
- Macchi, Andrea, Silvia Veghini, and Francesco Pegoraro, 2009, “‘Light Sail’ Acceleration Reexamined,” *Phys. Rev. Lett.* **103**, 085003.
- Mackinnon, A. J., *et al.*, 2004, “Proton radiography as an electromagnetic field and density perturbation diagnostic (invited),” *Rev. Sci. Instrum.* **75**, 3531–3536.
- Mackinnon, A. J., *et al.*, 2006, “Proton Radiography of a Laser-Driven Implosion,” *Phys. Rev. Lett.* **97**, 045001.
- Maksimchuk, A., S. Gu, K. Flippo, D. Umstadter, and A. Y. Bychenkov, 2000, “Forward Ion Acceleration in Thin Films Driven by a High-Intensity Laser,” *Phys. Rev. Lett.* **84**, 4108–4111.
- Malko, Sophia, Courtney Johnson, Derek B. Schaeffer, William Fox, and Gennady Fiksel, 2022, “Design of proton deflectometry with *in situ* x-ray fiducial for magnetized high-energy-density systems,” *Appl. Opt.* **61**, C133–C142.
- Mančić, A., J. Fuchs, P. Antici, S. A. Gaillard, and P. Audebert, 2008, “Absolute calibration of photostimulable image plate detectors used as (0.5–20 MeV) high-energy proton detectors,” *Rev. Sci. Instrum.* **79**, 073301.
- Mankos, M., M. R. Scheinfein, and J. M. Cowley, 1996, “Quantitative micromagnetics: Electron holography of magnetic thin films and multilayers,” *IEEE Trans. Magn.* **32**, 4150–4155.

- Manuel, M. J.-E., A. B. Zylstra, H. G. Rinderknecht, D. T. Casey, M. J. Rosenberg, N. Sinenian, C. K. Li, J. A. Frenje, F. H. Séguin, and R. D. Petrasso, 2012, “Source characterization and modeling development for monoenergetic-proton radiography experiments on OMEGA,” *Rev. Sci. Instrum.* **83**, 063506.
- Manuel, M. J.-E., *et al.*, 2012, “First Measurements of Rayleigh-Taylor-Induced Magnetic Fields in Laser-Produced Plasmas,” *Phys. Rev. Lett.* **108**, 255006.
- Manuel, M. J.-E., *et al.*, 2013, “Instability-driven electromagnetic fields in coronal plasmas,” *Phys. Plasmas* **20**, 056301.
- Manuel, M. J.-E., *et al.*, 2015, “Collisional effects on Rayleigh-Taylor-induced magnetic fields,” *Phys. Plasmas* **22**, 056305.
- Manuel, M. J.-E., *et al.*, 2020, “Enhanced spatial resolution of Eljen-204 plastic scintillators for use in rep-rated proton diagnostics,” *Rev. Sci. Instrum.* **91**, 103301.
- Margarone, D., *et al.*, 2012, “Laser-Driven Proton Acceleration Enhancement by Nanostructured Foils,” *Phys. Rev. Lett.* **109**, 234801.
- Mariscal, D., *et al.*, 2019, “First demonstration of ARC-accelerated proton beams at the National Ignition Facility,” *Phys. Plasmas* **26**, 043110.
- Martin, A. V., *et al.*, 2012, “Femtosecond dark-field imaging with an x-ray free electron laser,” *Opt. Express* **20**, 13501–13512.
- Mason, R. J., and M. Tabak, 1998, “Magnetic Field Generation in High-Intensity-Laser-Matter Interactions,” *Phys. Rev. Lett.* **80**, 524–527.
- McCrory, R. Land, *et al.*, 1988, “Laser-driven implosion of thermonuclear fuel to 20 to 40 g cm³,” *Nature (London)* **335**, 225–229.
- McKenna, P., *et al.*, 2008, “Effects of front surface plasma expansion on proton acceleration in ultraintense laser irradiation of foil targets,” *Laser Part. Beams* **26**, 591–596.
- McKenna, Paul, Filip Lindau, Olle Lundh, David Neely, Anders Persson, and Claes-Göran Wahlström, 2006, “High-intensity laser-driven proton acceleration: Influence of pulse contrast,” *Proc. R. Soc. A* **364**, 711–723.
- Meinecke, J., *et al.*, 2022, “Strong suppression of heat conduction in a laboratory replica of galaxy-cluster turbulent plasmas,” *Sci. Adv.* **8**, eabj6799.
- Mendel, C. W., and J. N. Olsen, 1975, “Charge-Separation Electric Fields in Laser Plasmas,” *Phys. Rev. Lett.* **34**, 859–862.
- Merrill, F. E., A. A. Golubev, F. G. Mariam, V. I. Turtikov, and D. Varentsov, 2009, “Proton microscopy at FAIR,” *AIP Conf. Proc.* **1195**, 667–670.
- Meshkov, E. E., 1969, “Instability of the interface of two gases accelerated by a shock wave,” *Fluid Dyn.* **4**, 101–104.
- Metzkes, J., K. Zeil, S. D. Kraft, L. Karsch, M. Sobiella, M. Rehwald, L. Obst, H. P. Schlenvoigt, and U. Schramm, 2016, “An online, energy-resolving beam profile detector for laser-driven proton beams,” *Rev. Sci. Instrum.* **87**, 083310.
- Modestov, M., V. Bychkov, G. Brodin, M. Marklund, and A. Brandenburg, 2014, “Evolution of the magnetic field generated by the Kelvin-Helmholtz instability,” *Phys. Plasmas* **21**, 072126.
- Modica, Frank, Tomasz Plewa, and Andrey Zhiglo, 2013, “The Braginskii model of the Rayleigh-Taylor instability. I. Effects of self-generated magnetic fields and thermal conduction in two dimensions,” *High Energy Density Phys.* **9**, 767–780.
- Moody, J. D., *et al.*, 2022, “Increased Ion Temperature and Neutron Yield Observed in Magnetized Indirectly Driven d₂-Filled Capsule Implosions on the National Ignition Facility,” *Phys. Rev. Lett.* **129**, 195002.
- Mora, P., 2003, “Plasma Expansion into a Vacuum,” *Phys. Rev. Lett.* **90**, 185002.
- Morita, T., *et al.*, 2016, “Proton imaging of an electrostatic field structure formed in laser-produced counter-streaming plasmas,” *J. Phys. Conf. Ser.* **688**, 012071.
- Morrison, J. T., S. Feister, K. D. Frische, D. R. Austin, G. K. Ngirmang, N. R. Murphy, C. Orban, E. A. Chowdhury, and W. M. Roquemore, 2018, “MeV proton acceleration at kHz repetition rate from ultra-intense laser liquid interaction,” *New J. Phys.* **20**, 022001.
- Moses, E. I., R. N. Boyd, B. A. Remington, C. J. Keane, and R. Al-Ayat, 2009, “The National Ignition Facility: Ushering in a new age for high energy density science,” *Phys. Plasmas* **16**, 041006.
- Mostert, W., V. Wheatley, R. Samtaney, and D. I. Pullin, 2014, “Effects of seed magnetic fields on magnetohydrodynamic implosion structure and dynamics,” *Phys. Fluids* **26**, 126102.
- Mottershead, T., D. Barlow, B. Blind, Gary E. Hogan, A. Jason, F. Merrill, K. Morley, C. Morris, A. Saunders, and R. Valdiviez, 2003, “Design and operation of a proton microscope for radiography at 800 MeV,” *Conf. Proc. C* **030512**, 702.
- Nakatsutsumi, M., *et al.*, 2018, “Self-generated surface magnetic fields inhibit laser-driven sheath acceleration of high-energy protons,” *Nat. Commun.* **9**, 280.
- Naumova, N. M., S. V. Bulanov, T. Zh. Esirkepov, D. Farina, K. Nishihara, F. Pegoraro, H. Ruhl, and A. S. Sakharov, 2001, “Formation of Electromagnetic Postsolitons in Plasmas,” *Phys. Rev. Lett.* **87**, 185004.
- Nilson, P. M., *et al.*, 2006, “Magnetic Reconnection and Plasma Dynamics in Two-Beam Laser-Solid Interactions,” *Phys. Rev. Lett.* **97**, 255001.
- Nilson, P. M., *et al.*, 2008, “Bidirectional jet formation during driven magnetic reconnection in two-beam laser-plasma interactions,” *Phys. Plasmas* **15**, 092701.
- Niroomand-Rad, A., C. R. Blackwell, B. M. Coursey, K. P. Gall, J. M. Galvin, W. L. McLaughlin, A. S. Meigooni, R. Nath, J. E. Rodgers, and C. G. Soares, 1998, “Radiochromic film dosimetry: Recommendations of AAPM Radiation Therapy Committee Task Group 55,” *Med. Phys.* **25**, 2093–2115.
- Nishiguchi, A., T. Yabe, M. G. Haines, M. Psimopoulos, and H. Takewaki, 1984, “Convective Amplification of Magnetic Fields in Laser-Produced Plasmas by the Nernst Effect,” *Phys. Rev. Lett.* **53**, 262–265.
- Nishiuchi, M., *et al.*, 2015, “Projection imaging with directional electron and proton beams emitted from an ultrashort intense laser-driven thin foil target,” *Plasma Phys. Controlled Fusion* **57**, 025001.
- Noaman-ul Haq, Muhammad, *et al.*, 2017, “Statistical analysis of laser driven protons using a high-repetition-rate tape drive target system,” *Phys. Rev. Accel. Beams* **20**, 041301.
- Nuckolls, J., L. Wood, A. Thiessen, and G. Zimmerman, 1972, “Laser compression of matter to super-high densities: Thermonuclear (CTR) applications,” *Nature (London)* **239**, 139–142.
- Nürnberg, F., *et al.*, 2009, “Radiochromic film imaging spectroscopy of laser-accelerated proton beams,” *Rev. Sci. Instrum.* **80**, 033301.
- Obst, L., *et al.*, 2017, “Efficient laser-driven proton acceleration from cylindrical and planar cryogenic hydrogen jets,” *Sci. Rep.* **7**, 10248.
- Obst-Huebl, Lieselotte, *et al.*, 2018, “All-optical structuring of laser-driven proton beam profiles,” *Nat. Commun.* **9**, 5292.
- Orimo, Satoshi, *et al.*, 2007, “Simultaneous proton and x-ray imaging with femtosecond intense laser driven plasma source,” *Jpn. J. Appl. Phys.* **46**, 5853–5858.
- Ostermayr, T. M., *et al.*, 2020, “Laser-driven x-ray and proton micro-source and application to simultaneous single-shot bi-modal radiographic imaging,” *Nat. Commun.* **11**, 6174.

- Palmer, C. A. J., *et al.*, 2019, “Field reconstruction from proton radiography of intense laser driven magnetic reconnection,” *Phys. Plasmas* **26**, 083109.
- Park, H.-S., *et al.*, 2015, “Collisionless shock experiments with lasers and observation of Weibel instabilities,” *Phys. Plasmas* **22**, 056311.
- Parker, E. N., 1957, “Sweet’s mechanism for merging magnetic fields in conducting fluids,” *J. Geophys. Res.* **62**, 509–520.
- Passoni, M., L. Bertagna, and A. Zani, 2010, “Target normal sheath acceleration: Theory, comparison with experiments and future perspectives,” *New J. Phys.* **12**, 045012.
- Paudel, Y., *et al.*, 2012, “Self-proton/ion radiography of laser-produced proton/ion beam from thin foil targets,” *Phys. Plasmas* **19**, 123101.
- Peebles, J. L., J. R. Davies, D. H. Barnak, T. Cracium, M. J. Bonino, and R. Betti, 2020, “Axial proton probing of magnetic and electric fields inside laser-driven coils,” *Phys. Plasmas* **27**, 063109.
- Peebles, J. L., J. R. Davies, D. H. Barnak, F. Garcia-Rubio, P. V. Heuer, G. Brent, R. Spielman, and R. Betti, 2022, “An assessment of generating quasi-static magnetic fields using laser-driven ‘capacitor’ coils,” *Phys. Plasmas* **29**, 080501.
- Perkins, L. J., B. G. Logan, G. B. Zimmerman, and C. J. Werner, 2013, “Two-dimensional simulations of thermonuclear burn in ignition-scale inertial confinement fusion targets under compressed axial magnetic fields,” *Phys. Plasmas* **20**, 072708.
- Petrasso, R. D., *et al.*, 2009, “Lorentz Mapping of Magnetic Fields in Hot Dense Plasmas,” *Phys. Rev. Lett.* **103**, 085001.
- PlasmaPy Community, 2023, computer code `PlasmaPy`.
- Poludniowski, G., N. M. Allinson, and P. M. Evans, 2015, “Proton radiography and tomography with application to proton therapy,” *Br. J. Radiol.* **88**, 125002.
- Poole, P. L., C. Willis, G. E. Cochran, R. T. Hanna, C. D. Andereck, and D. W. Schumacher, 2016, “Moderate repetition rate ultra-intense laser targets and optics using variable thickness liquid crystal films,” *Appl. Phys. Lett.* **109**, 151109.
- Poole, P. L., *et al.*, 2018, “Laser-driven ion acceleration via target normal sheath acceleration in the relativistic transparency regime,” *New J. Phys.* **20**, 013019.
- Prall, Matthias, *et al.*, 2016, “High-energy proton imaging for biomedical applications,” *Sci. Rep.* **6**, 27651.
- Praturi, Divya Sri, and Sharath S. Girimaji, 2019, “Mechanisms of canonical Kelvin-Helmholtz instability suppression in magneto-hydrodynamic flows,” *Phys. Fluids* **31**, 024108.
- Puyuelo Valdes, Pilar, *et al.*, 2022, “Implementation of a thin, flat water target capable of high-repetition-rate MeV-range proton acceleration in a high-power laser at the CLPU,” *Plasma Phys. Controlled Fusion* **64**, 054003.
- Quinn, K., 2010, “Plasma dynamics following ultraintense laser-solid interactions,” Ph.D. thesis (Queen’s University Belfast).
- Quinn, K., *et al.*, 2009a, “Laser-Driven Ultrafast Field Propagation on Solid Surfaces,” *Phys. Rev. Lett.* **102**, 194801.
- Quinn, K., *et al.*, 2009b, “Modified proton radiography arrangement for the detection of ultrafast field fronts,” *Rev. Sci. Instrum.* **80**, 113506.
- Quinn, K., *et al.*, 2009c, “Observation of the transient charging of a laser-irradiated solid,” *Eur. Phys. J. D* **55**, 293–297.
- Quinn, K., *et al.*, 2012, “Weibel-Induced Filamentation during an Ultrafast Laser-Driven Plasma Expansion,” *Phys. Rev. Lett.* **108**, 135001.
- Quinn, M. N., *et al.*, 2011, “On the investigation of fast electron beam filamentation in laser-irradiated solid targets using multi-MeV proton emission,” *Plasma Phys. Controlled Fusion* **53**, 124012.
- Ramakrishna, B., S. Kar, M. Borghesi, and A. Schiavi, 2008, “Modeling proton probing of femtosecond laser propagation through underdense plasma,” Technical Report No. RAL-TR-2008-025.
- Ramakrishna, B., *et al.*, 2010, “Laser-Driven Fast Electron Collision in Targets with Resistivity Boundary,” *Phys. Rev. Lett.* **105**, 135001.
- Rayleigh, Lord, 1882, “Investigation of the character of the equilibrium of an incompressible heavy fluid of variable density,” *Proc. London Math. Soc.* **s1-14**, 170–177.
- Richtmyer, R. D., 1960, “Taylor instability in a shock acceleration of compressible fluids,” *Commun. Pure Appl. Math.* **13**, 297.
- Rincon, François, 2019, “Dynamo theories,” *J. Plasma Phys.* **85**, 205850401.
- Robinson, A. P. L., R. M. G. M. Trines, N. P. Dover, and Z. Najmudin, 2012, “Hole-boring radiation pressure acceleration as a basis for producing high-energy proton bunches,” *Plasma Phys. Controlled Fusion* **54**, 115001.
- Robinson, A. P. L., M. Zepf, S. Kar, R. G. Evans, and C. Bellei, 2008, “Radiation pressure acceleration of thin foils with circularly polarized laser pulses,” *New J. Phys.* **10**, 013021.
- Romagnani, L., *et al.*, 2005, “Dynamics of Electric Fields Driving the Laser Acceleration of Multi-MeV Protons,” *Phys. Rev. Lett.* **95**, 195001.
- Romagnani, L., *et al.*, 2008a, “Proton probing measurement of electric and magnetic fields generated by ns and ps laser-matter interactions,” *Laser Part. Beams* **26**, 241–248.
- Romagnani, L., *et al.*, 2008b, “Observation of Collisionless Shocks in Laser-Plasma Experiments,” *Phys. Rev. Lett.* **101**, 025004.
- Romagnani, L., *et al.*, 2010, “Observation of Magnetized Soliton Remnants in the Wake of Intense Laser Pulse Propagation through Plasmas,” *Phys. Rev. Lett.* **105**, 175002.
- Romagnani, L., *et al.*, 2019, “Dynamics of the Electromagnetic Fields Induced by Fast Electron Propagation in Near-Solid-Density Media,” *Phys. Rev. Lett.* **122**, 025001.
- Romagnani, Lorenzo, 2005, “Laser-plasma investigations employing laser-driven proton probes,” Ph.D. thesis (Queen’s University Belfast).
- Rosenberg, M. J., C. K. Li, W. Fox, I. Igumenshchev, F. H. Séguin, R. P. J. Town, J. A. Frenje, C. Stoeckl, V. Glebov, and R. D. Petrasso, 2015, “A laboratory study of asymmetric magnetic reconnection in strongly driven plasmas,” *Nat. Commun.* **6**, 6190.
- Rosenberg, M. J., C. K. Li, W. Fox, A. B. Zylstra, C. Stoeckl, F. H. Séguin, J. A. Frenje, and R. D. Petrasso, 2015, “Slowing of Magnetic Reconnection Concurrent with Weakening Plasma Inflows and Increasing Collisionality in Strongly Driven Laser-Plasma Experiments,” *Phys. Rev. Lett.* **114**, 205004.
- Rosenberg, M. J., J. S. Ross, C. K. Li, R. P. J. Town, F. H. Séguin, J. A. Frenje, D. H. Froula, and R. D. Petrasso, 2012, “Characterization of single and colliding laser-produced plasma bubbles using Thomson scattering and proton radiography,” *Phys. Rev. E* **86**, 056407.
- Rosensweig, Ronald E., 1979, “Fluidization: Hydrodynamic stabilization with a magnetic field,” *Science* **204**, 57–60.
- Rosenzweig, G., E. Kroupp, T. Queller, A. Starobinets, Y. Maron, V. Tangri, J. L. Giuliani, and A. Fruchtman, 2020, “Local measurements of the spatial magnetic field distribution in a Z-pinch plasma during and near stagnation using polarization spectroscopy,” *Phys. Plasmas* **27**, 022705.
- Ruyer, C., *et al.*, 2020, “Growth of concomitant laser-driven collisionless and resistive electron filamentation instabilities over large spatiotemporal scales,” *Nat. Phys.* **16**, 983–988.
- Rygg, J. R., *et al.*, 2008, “Proton radiography of inertial fusion implosions,” *Science* **319**, 1223–1225.

- Ryu, Dongsu, T. W. Jones, and Adam Frank, 2000, “The magneto-hydrodynamic Kelvin-Helmholtz instability: A three-dimensional study of nonlinear evolution,” *Astrophys. J.* **545**, 475–493.
- Sadler, James, Hui Li, and Kirk Flippo, 2020, “Magnetic field generation from composition gradients in inertial confinement fusion fuel,” *Phil. Trans. R. Soc. A* **378**, 20200045.
- Sadler, James D., Samuel Green, Shengtai Li, K. A. Flippo, and Hui Li, 2022, “Faster ablative Kelvin-Helmholtz growth in a magnetic field,” *Phys. Plasmas* **29**, 052708.
- Sadler, James D., Hui Li, and Brian M. Haines, 2020, “Magnetization around mix jets entering inertial confinement fusion fuel,” *Phys. Plasmas* **27**, 072707.
- Samtaney, Ravi, 2003, “Suppression of the Richtmyer-Meshkov instability in the presence of a magnetic field,” *Phys. Fluids* **15**, L53.
- Sano, Takayoshi, Tsuyoshi Inoue, and Katsunobu Nishihara, 2013, “Critical Magnetic Field Strength for Suppression of the Richtmyer-Meshkov Instability in Plasmas,” *Phys. Rev. Lett.* **111**, 205001.
- Sarri, G., *et al.*, 2010a, “The application of laser-driven proton beams to the radiography of intense laser-Hohlraum interactions,” *New J. Phys.* **12**, 045006.
- Sarri, G., *et al.*, 2010b, “Observation of Postsoliton Expansion Following Laser Propagation through an Underdense Plasma,” *Phys. Rev. Lett.* **105**, 175007.
- Sarri, G., *et al.*, 2012, “Dynamics of Self-Generated, Large Amplitude Magnetic Fields Following High-Intensity Laser Matter Interaction,” *Phys. Rev. Lett.* **109**, 205002.
- Sauli, Fabio, 2014, “Multi-wire proportional chambers,” in *Gaseous Radiation Detectors: Fundamentals and Applications*, Cambridge Monographs on Particle Physics, Nuclear Physics and Cosmology Vol. 36 (Cambridge University Press, Cambridge, England), pp. 211–263.
- Schaeffer, D. B., W. Fox, R. K. Follett, G. Fiksel, C. K. Li, J. Matteucci, A. Bhattacharjee, and K. Germaschewski, 2019, “Direct Observations of Particle Dynamics in Magnetized Collisionless Shock Precursors in Laser-Produced Plasmas,” *Phys. Rev. Lett.* **122**, 245001.
- Schaeffer, D. B., W. Fox, D. Haberberger, G. Fiksel, A. Bhattacharjee, D. H. Barnak, S. X. Hu, and K. Germaschewski, 2017, “Generation and Evolution of High-Mach-Number Laser-Driven Magnetized Collisionless Shocks in the Laboratory,” *Phys. Rev. Lett.* **119**, 025001.
- Schiavi, A., 2008, “Interpretation of laser-produced ion beam diagnostics using the PTRACE code,” in *Proceedings of the 35th EPS Conference on Plasma Physics, Hersonissos, Greece, 2008*, Europhysics Conference Abstracts Vol. 32D, edited by P. Lalouis (Curran Associates, Red Hook, NY), p. 126.
- Schollmeier, M., M. Geissel, A. B. Sefkova, and K. Flippo, 2014, “Improved spectral data unfolding for radiochromic film imaging spectroscopy of laser-accelerated proton beams,” *Rev. Sci. Instrum.* **85**, 043305.
- Schollmeier, M., *et al.*, 2015, “Laser-to-hot-electron conversion limitations in relativistic laser matter interactions due to multi-picosecond dynamics,” *Phys. Plasmas* **22**, 043116.
- Schreiber, J., *et al.*, 2006, “Analytical Model for Ion Acceleration by High-Intensity Laser Pulses,” *Phys. Rev. Lett.* **97**, 045005.
- Schumaker, W., *et al.*, 2013, “Ultrafast Electron Radiography of Magnetic Fields in High-Intensity Laser-Solid Interactions,” *Phys. Rev. Lett.* **110**, 015003.
- Segre, Sergio E., 1999, “A review of plasma polarimetry—Theory and methods,” *Plasma Phys. Controlled Fusion* **41**, R57.
- Séguin, F. H., *et al.*, 2003, “Spectrometry of charged particles from inertial-confinement-fusion plasmas,” *Rev. Sci. Instrum.* **74**, 975–995.
- Séguin, F. H., *et al.*, 2012, “Time evolution of filamentation and self-generated fields in the coronae of directly driven inertial-confinement fusion capsules,” *Phys. Plasmas* **19**, 012701.
- Séguin, F. H., *et al.*, 2016, “Effects of fuel-capsule shimming and drive asymmetry on inertial-confinement-fusion symmetry and yield,” *Phys. Plasmas* **23**, 032705.
- Shen, Naijian, D. I. Pullin, Vincent Wheatley, and Ravi Samtaney, 2019, “Impulse-driven Richtmyer-Meshkov instability in Hall-magneto-hydrodynamics,” *Phys. Rev. Fluids* **4**, 103902.
- Shen, Naijian, Vincent Wheatley, D. I. Pullin, and Ravi Samtaney, 2020, “Magneto-hydrodynamic Richtmyer-Meshkov instability under an arbitrarily oriented magnetic field,” *Phys. Plasmas* **27**, 062101.
- Shen, X. F., A. Pukhov, and B. Qiao, 2021, “Monoenergetic High-Energy Ion Source via Femtosecond Laser Interacting with a Microtape,” *Phys. Rev. X* **11**, 041002.
- Shevelev, V. S., A. V. Ishchenko, A. S. Vanetsev, V. Nagirnyi, and S. I. Omelkov, 2022, “Ultrafast hybrid nanocomposite scintillators: A review,” *J. Lumin.* **242**, 118534.
- Simos, N., H. Ludewig, A. Bolotnikov, R. James, G. Camarda, C. Copeland, and A. Aronson, 2009, “Effects of high proton fluences on CZT detectors,” in *Proceedings of the 23rd Particle Accelerator Conference (PAC '09), Vancouver, British Columbia, Canada, 2009*, edited by M. Comyn, S. Koscielniak, V. R. W. Schaa, and P. W. Schmor (JACoW, Geneva).
- Simpson, R. A., *et al.*, 2021, “Scaling of laser-driven electron and proton acceleration as a function of laser pulse duration, energy, and intensity in the multi-picosecond regime,” *Phys. Plasmas* **28**, 013108.
- Sinenian, N., *et al.*, 2011, “The response of CR-39 nuclear track detector to 1–9 MeV protons,” *Rev. Sci. Instrum.* **82**, 103303.
- Slutz, S. A., M. C. Herrmann, R. A. Vesey, A. B. Sefkow, D. B. Sinar, D. C. Rovang, K. J. Peterson, and M. E. Cuneo, 2010, “Pulsed-power-driven cylindrical liner implosions of laser preheated fuel magnetized with an axial field,” *Phys. Plasmas* **17**, 056303.
- Smalyuk, V. A., T. R. Boehly, L. S. Iwan, T. J. Kessler, J. P. Knauer, F. J. Marshall, D. D. Meyerhofer, C. Stoeckl, B. Yaakobi, and D. K. Bradley, 2001, “Fourier-space image processing for spherical experiments on OMEGA (invited),” *Rev. Sci. Instrum.* **72**, 635–642.
- Smalyuk, V. A., *et al.*, 2003, “Time-Resolved Areal-Density Measurements with Proton Spectroscopy in Spherical Implosions,” *Phys. Rev. Lett.* **90**, 135002.
- Snively, R. A., *et al.*, 2000, “Intense High-Energy Proton Beams from Petawatt-Laser Irradiation of Solids,” *Phys. Rev. Lett.* **85**, 2945–2948.
- Sokollik, T., M. Schnürer, S. Steinke, P. V. Nickles, W. Sandner, M. Amin, T. Toncian, O. Willi, and A. A. Andreev, 2009, “Directional Laser-Driven Ion Acceleration from Microspheres,” *Phys. Rev. Lett.* **103**, 135003.
- Sokollik, T., *et al.*, 2008, “Transient electric fields in laser plasmas observed by proton streak deflectometry,” *Appl. Phys. Lett.* **92**, 091503.
- Song, Yang, and Bhuvana Srinivasan, 2020, “A survey of the effects of magnetic fields, resistivity, viscosity and thermal conduction on the Rayleigh-Taylor instability,” *Radiat. Eff. Defects Solids* **175**, 1009–1014.
- Spiers, B. T., R. Aboushelbaya, Q. Feng, M. W. Mayr, I. Ouatu, R. W. Paddock, R. Timmis, R. H.-W. Wang, and P. A. Norreys, 2021, “Methods for extremely sparse-angle proton tomography,” *Phys. Rev. E* **104**, 045201.
- Srinivasan, Bhuvana, Guy Dimonte, and Xian-Zhu Tang, 2012, “Magnetic Field Generation in Rayleigh-Taylor Unstable Inertial Confinement Fusion Plasmas,” *Phys. Rev. Lett.* **108**, 165002.

- Srinivasan, Bhuvana, and Xian-Zhu Tang, 2013, “The mitigating effect of magnetic fields on Rayleigh-Taylor unstable inertial confinement fusion plasmas,” *Phys. Plasmas* **20**, 056307.
- Stamper, J. A., 1991, “Review on spontaneous magnetic fields in laser-produced plasmas: Phenomena and measurements,” *Laser Part. Beams* **9**, 841–862.
- Stamper, J. A., K. Papadopoulos, R. N. Sudan, S. O. Dean, E. A. McLean, and J. M. Dawson, 1971, “Spontaneous Magnetic Fields in Laser-Produced Plasmas,” *Phys. Rev. Lett.* **26**, 1012.
- Strozzi, D., L. Perkins, M. Marinak, D. Larson, J. Koning, and B. Logan, 2015, “Imposed magnetic field and hot electron propagation in inertial fusion hohlraums,” *J. Plasma Phys.* **81**, 475810603.
- Sulman, Mohamed M., J. F. Williams, and Robert D. Russell, 2011, “An efficient approach for the numerical solution of the Monge-Ampère equation,” *Appl. Numer. Math.* **61**, 298–307.
- Sutcliffe, Graeme, *et al.*, 2021, “A new tri-particle backlighter for high-energy-density plasmas (invited),” *Rev. Sci. Instrum.* **92**, 063524.
- Swisher, N. C., C. C. Kuranz, D. Arnett, O. Hurricane, B. A. Remington, H. F. Robey, and S. I. Abarzhi, 2015, “Rayleigh-Taylor mixing in supernova experiments,” *Phys. Plasmas* **22**, 102707.
- Takabe, H., and Y. Kuramitsu, 2021, “Recent progress of laboratory astrophysics with intense lasers,” *High Power Laser Sci. Eng.* **9**, e49.
- Tang, H., B. K. Russell, A. Maksimchuk, P. T. Campbell, M. J.-E. Manuel, and L. Willingale, 2020, “Scintillator detector characterization for laser-driven proton beam imaging,” *Rev. Sci. Instrum.* **91**, 123304.
- Taylor, Geoffrey, 1931, “Effect of variation in density on the stability of superposed streams of fluid,” *Proc. R. Soc. A* **132**, 499.
- Taylor, J. B., 1986, “Relaxation and magnetic reconnection in plasmas,” *Rev. Mod. Phys.* **58**, 741–763.
- Thoma, C., D. R. Welch, R. E. Clark, D. V. Rose, and I. E. Golovkin, 2017, “Hybrid-PIC modeling of laser-plasma interactions and hot electron generation in gold hohlraum walls,” *Phys. Plasmas* **24**, 062707.
- Thomson, William, 1880, “On a disturbing infinity in Lord Rayleigh’s solution for waves in a plane vortex stratum,” *Nature (London)* **23**, 45.
- Toncian, Toma, *et al.*, 2006, “Ultrafast laser-driven microlens to focus and energy-select mega-electron volt protons,” *Science* **312**, 410–413.
- Tubman, E. R., *et al.*, 2021, “Observations of pressure anisotropy effects within semi-collisional magnetized plasma bubbles,” *Nat. Commun.* **12**, 334.
- Tzeferacos, P., M. Fatenejad, N. Flocke, C. Graziani, G. Gregori, D. Q. Lamb, D. Lee, J. Meinecke, A. Scopatz, and K. Weide, 2015, “Flash mhd simulations of experiments that study shock-generated magnetic fields,” *High Energy Density Phys.* **17**, 24–31.
- Tzeferacos, P., *et al.*, 2017, “Numerical modeling of laser-driven experiments aiming to demonstrate magnetic field amplification via turbulent dynamo,” *Phys. Plasmas* **24**, 041404.
- Tzeferacos, P., *et al.*, 2018, “Laboratory evidence of dynamo amplification of magnetic fields in a turbulent plasma,” *Nat. Commun.* **9**, 591.
- Varentsov, D., *et al.*, 2016, “Commissioning of the prior proton microscope,” *Rev. Sci. Instrum.* **87**, 023303.
- Vay, J.-L., 2008, “Simulation of beams or plasmas crossing at relativistic velocity,” *Phys. Plasmas* **15**, 056701.
- Wagner, F., *et al.*, 2016, “Maximum Proton Energy above 85 MeV from the Relativistic Interaction of Laser Pulses with Micrometer Thick CH₂ Targets,” *Phys. Rev. Lett.* **116**, 205002.
- Walsh, C. A., A. J. Crilly, and J. P. Chittenden, 2020, “Magnetized directly-driven ICF capsules: Increased instability growth from non-uniform laser drive,” *Nucl. Fusion* **60**, 106006.
- Walsh, C. A., K. McGlinchey, J. K. Tong, B. D. Appelbe, A. Crilly, M. F. Zhang, and J. P. Chittenden, 2019, “Perturbation modifications by pre-magnetisation of inertial confinement fusion implosion,” *Phys. Plasmas* **26**, 022701.
- Wan, Yang, Omri Seemann, Sheroy Tata, Igor A. Andriyash, Slava Smartsev, Eyal Kroupp, and Victor Malka, 2022, “Direct observation of relativistic broken plasma waves,” *Nat. Phys.* **18**, 1186–1190.
- Wan, Yang, Sheroy Tata, Omri Seemann, Eitan Y. Levine, Slava Smartsev, Eyal Kroupp, and Victor Malka, 2023, “Femtosecond electron microscopy of relativistic electron bunches,” *Light Sci. Appl.* **12**, 116.
- Wang, P., J. Cammin, F. Bisello, T. D. Solberg, J. E. McDonough, T. C. Zhu, D. Menichelli, and B. K. Teo, 2016, “Proton computed tomography using a 1D silicon diode array,” *Med. Phys.* **43**, 5758.
- Wang, W. P., *et al.*, 2015, “Large-scale proton radiography with micrometer spatial resolution using femtosecond petawatt laser system,” *AIP Adv.* **5**, 107214.
- Weibel, Erich S., 1959, “Spontaneously Growing Transverse Waves in a Plasma due to an Anisotropic Velocity Distribution,” *Phys. Rev. Lett.* **2**, 83.
- Welch, D. R., D. V. Rose, R. E. Clark, T. C. Genoni, and T. P. Hughes, 2004, “Implementation of a non-iterative implicit electromagnetic field solver for dense plasma simulation,” *Comput. Phys. Commun.* **164**, 183–188.
- Wilks, S. C., W. L. Kruer, M. Tabak, and A. B. Langdon, 1992, “Absorption of Ultra-Intense Laser Pulses,” *Phys. Rev. Lett.* **69**, 1383–1386.
- Wilks, S. C., A. B. Langdon, T. E. Cowan, M. Roth, M. Singh, S. Hatchett, M. H. Key, D. Pennington, A. Mackinnon, and R. A. Snavely, 2001, “Energetic proton generation in ultra-intense laser-solid interactions,” *Phys. Plasmas* **8**, 542–549.
- Willingale, L., *et al.*, 2010a, “Proton deflectometry of a magnetic reconnection geometry,” *Phys. Plasmas* **17**, 043104.
- Willingale, L., *et al.*, 2010b, “Fast Advection of Magnetic Fields by Hot Electrons,” *Phys. Rev. Lett.* **105**, 095001.
- Willingale, L., *et al.*, 2011a, “High-Power, Kilojoule Class Laser Channeling in Millimeter-Scale Underdense Plasma,” *Phys. Rev. Lett.* **106**, 105002.
- Willingale, L., *et al.*, 2011b, “Proton probe measurement of fast advection of magnetic fields by hot electrons,” *Plasma Phys. Controlled Fusion* **53**, 124026.
- Willingale, L., *et al.*, 2013, “Surface waves and electron acceleration from high-power, kilojoule-class laser interactions with underdense plasma,” *New J. Phys.* **15**, 025023.
- Xu, X. H., *et al.*, 2019, “Detection and analysis of laser driven proton beams by calibrated GafChromic HD-V2 and MD-V3 radiochromic films,” *Rev. Sci. Instrum.* **90**, 033306.
- Yamada, Masaaki, Russell Kulsrud, and Hantao Ji, 2010, “Magnetic reconnection,” *Rev. Mod. Phys.* **82**, 603–664.
- Yamanaka, C., Y. Kato, Y. Izawa, K. Yoshida, T. Yamanaka, T. Sasaki, M. Nakatsuka, T. Mochizuki, J. Kuroda, and S. Nakai, 1981, “Nd-doped phosphate glass laser systems for laser-fusion research,” *IEEE J. Quantum Electron.* **17**, 1639–1649.
- Yao, W., *et al.*, 2022, “Detailed characterization of a laboratory magnetized supercritical collisionless shock and of the associated proton energization,” *Matter Radiat. Extremes* **7**, 014402.

- Yin, L., B. J. Albright, B. M. Hegelich, K. J. Bowers, K. A. Flippo, T. J. T. Kwan, and J. C. Fernández, 2007, “Monoenergetic and GeV ion acceleration from the laser breakout afterburner using ultrathin targets,” *Phys. Plasmas* **14**, 056706.
- Yogo, A., *et al.*, 2008, “Laser ion acceleration via control of the near-critical density target,” *Phys. Rev. E* **77**, 016401.
- Zeil, K., S. D. Kraft, S. Bock, M. Bussmann, T. E. Cowan, T. Kluge, J. Metzkes, T. Richter, R. Sauerbrey, and U. Schramm, 2010, “The scaling of proton energies in ultrashort pulse laser plasma acceleration,” *New J. Phys.* **12**, 045015.
- Zellner, M. B., M. S. Freeman, L. P. Neukirch, W. C. Uhlig, P. R. Berning, R. L. Doney, and D. Phillips, 2021, “Modeling proton interactions with magnetodynamic targets for electromagnetic field mapping,” *AIP Adv.* **11**, 055308.
- Zhai, S. H., *et al.*, 2019, “Proton array focused by a laser-irradiated mesh,” *Appl. Phys. Lett.* **114**, 013509.
- Zhang, C. J., *et al.*, 2016, “Capturing relativistic wakefield structures in plasmas using ultrashort high-energy electrons as a probe,” *Sci. Rep.* **6**, 29485.
- Zhang, Chaojie, *et al.*, 2020, “Measurements of the Growth and Saturation of Electron Weibel Instability in Optical-Field Ionized Plasmas,” *Phys. Rev. Lett.* **125**, 255001.
- Zhang, Mei, Liang Sheng, Huasi Hu, Yang Li, Yongtang Liu, Dongwei Hei, Bodong Peng, and Jizhen Zhao, 2018, “Theoretical and experimental investigation of gating performance of subnanosecond image intensifier with microstrip photocathode,” *IEEE Trans. Nucl. Sci.* **65**, 2310–2315.
- Zhong, Jiayong, *et al.*, 2010, “Modelling loop-top x-ray source and reconnection outflows in solar flares with intense lasers,” *Nat. Phys.* **6**, 984–987.
- Ziegler, J. F., M. D. Ziegler, and J. P. Biersack, 2010, “SRIM—The stopping and range of ions in matter (2010),” *Nucl. Instrum. Methods Phys. Res., Sect. B* **268**, 1818–1823.
- Ziegler, T., *et al.*, 2021, “Proton beam quality enhancement by spectral phase control of a PW-class laser system,” *Sci. Rep.* **11**, 7338.
- Zimmer, M., S. Scheuren, T. Ebert, G. Schaumann, B. Schmitz, J. Hornung, V. Bagnoud, C. Rödel, and M. Roth, 2021, “Analysis of laser-proton acceleration experiments for development of empirical scaling laws,” *Phys. Rev. E* **104**, 045210.
- Zimmerman, G., D. Kershaw, D. Bailey, and J. Harte, 1977, “LASNEX code for inertial confinement fusion,” Lawrence Livermore National Laboratory Technical Report No. UCRL-80169.
- Zylstra, A. B., H. G. Rinderknecht, N. Sinenian, M. J. Rosenberg, M. Manuel, F. H. Séguin, D. T. Casey, J. A. Frenje, C. K. Li, and R. D. Petrasso, 2011, “Increasing the energy dynamic range of solid-state nuclear track detectors using multiple surfaces,” *Rev. Sci. Instrum.* **82**, 083301.
- Zylstra, A. B., *et al.*, 2012, “Using high-intensity laser-generated energetic protons to radiograph directly driven implosions,” *Rev. Sci. Instrum.* **83**, 013511.
- Zylstra, A. B., *et al.*, 2020, “Saturn-ring proton backlighters for the National Ignition Facility,” *Rev. Sci. Instrum.* **91**, 093505.